INL/RPT-24-80533
ANL/NSE-24/63

Nuclear Energy Advanced Modeling and Simulation

High-Temperature Gas-Cooled Pebble-Bed Reactors Running In And Transient Modeling Capabilities Demonstration

M2MS-24IN0701181

SEPTEMBER 2024

Joshua T. Hanophy,
Ryan H. Stewart, and
Paolo Balestra

Idaho National Laboratory

Zhiee Jhia Ooi,
Jun Fang,
Thanh Hua, and
Ling Zou

Argonne National Laboratory

Battelle Energy Alliance manages INL for the U.S. Department of Energy's Office of Nuclear Energy

DISCLAIMER

This information was prepared as an account of work sponsored by an agency of the U.S. Government. Neither the U.S. Government nor any agency thereof, nor any of their employees, makes any warranty, expressed or implied, or assumes any legal liability or responsibility for the accuracy, completeness, or usefulness, of any information, apparatus, product, or process disclosed, or represents that its use would not infringe privately owned rights. References herein to any specific commercial product, process, or service by trade name, trademark, manufacturer, or otherwise, does not necessarily constitute or imply its endorsement, recommendation, or favoring by the U.S. Government or any agency thereof. The views and opinions of authors expressed herein do not necessarily state or reflect those of the U.S. Government or any agency thereof.

INL/RPT-24-80533
ANL/NSE-24/63

High-Temperature Gas-Cooled Pebble-Bed Reactors Running In And Transient Modeling Capabilities Demonstration

M2MS-24IN0701181

Joshua T. Hanophy,
Ryan H. Stewart, and
Paolo Balestra
Idaho National Laboratory
Zhiee Jhia Ooi,
Jun Fang,
Thanh Hua, and
Ling Zou
Argonne National Laboratory

September 2024

Idaho National Laboratory
Nuclear Energy Advanced Modeling and Simulation
Idaho Falls, Idaho 83415

http://www.inl.gov

Prepared for the
U.S. Department of Energy
Office of Nuclear Energy
Under DOE Idaho Operations Office
Contract DE-AC07-05ID14517

Page intentionally left blank

ABSTRACT

This study presents a comprehensive benchmarking and verification effort of several thermal-hydraulic and multiphysics capabilities for high-temperature gas-cooled reactor (HTGR) applications. The first part of this effort focuses on the running-in verification of Griffin's multiphysics capabilities, specifically for simulating the evolution of pebble-bed reactor cores from startup to equilibrium. In the absence of validation data, code-to-code comparisons are conducted with *kugelpy*, showing good agreement for key quantities like maximum power density and fresh core k-eff predictions. However, discrepancies in equilibrium core predictions suggest potential issues with cross sections, underscoring the need for further refinement and evaluation. The High Temperature Test Facility (HTTF) system analysis code benchmark uses RELAP5-3D, SAM, and GAMMA+ to assess their predictive capabilities for HTTF behavior under both normal operation and pressurized conduction cooldown transient conditions. While there is good agreement in predicting major parameters such as coolant temperature, solid temperature, and flow distribution, discrepancies in transient behavior highlight differences in modeling approaches, nodalizations, and heat transfer models. The HTTF lower plenum computational fluid dynamics benchmark employs nekRS to simulate flow mixing phenomena, successfully capturing relevant flow physics and demonstrating mesh independence in complex geometries. Preliminary results suggest a relatively uniform temperature field but significant unsteadiness in the flow, requiring time-averaging analyses. The GPBR200 system analysis code benchmark uses SAM's core channel and porous media models, incorporating a reactor cavity cooling system loop for decay heat removal. During steady-state and transient conditions, including protected depressurized and pressurized loss of forced cooling, both models show good agreement in predicting temperature profiles and key parameters. Notably, while the core channel model underpredicts convective heat transfer effects, both models maintain temperatures well below the tristructural isotropic fuel safety limit. These benchmarking efforts collectively enhance the predictive capabilities of the tools used in HTGR design and safety analysis, guiding developments to improve their accuracy and applicability.

Page intentionally left blank

CONTENTS

FIGURES

TABLES

Page intentionally left blank

ACRONYMS

ANL	Argonne National Laboratory
CFD	Computational Fluid Dynamics
DCC	Depressurized Conduction Cooldown
DEM	discrete element method
DLOFC	Depressurized Loss of Forced Cooling
GPBR200	200 MW General Pebble Bed Reactor
HTGR	high-temperature gas-cooled reactor
HTR-PM	High-Temperature Gas-Cooled Reactor pebble-bed module
HTTF	High Temperature Test Facility
INL	Idaho National Laboratory
KAERI	Korea Atomic Energy Research Institute
LES	large eddy simulation
MHTGR	Modular High Temperature Gas-cooled Reactor
MOOSE	Multiphysics Object-Oriented Simulation Environment
OTTO	once-through-then-out
PBMR400	400 MW Pebble Bed Modular Reactor
PBR	pebble-bed reactor
PCC	Pressurized Conduction Cooldown
PLOFC	Pressurized Loss of Forced Cooling
RANS	Reynolds-averaged Navier-Stokes

RCCS	Reactor Cavity-Cooling System
RPV	Reactor Pressure Vessel
SAM	System Analysis Module
sGPBR200	simplified 200 MW General Pebble Bed Reactor
VTB	Virtual Test Bed

Page intentionally left blank

High-Temperature Gas-Cooled Pebble-Bed Reactors Running In and Transient Modeling Capabilities Demonstration

M2MS-24IN0701181

1. RUNNING-IN VERIFICATION EFFORTS

Two modern reactor physics software tools have been developed that include various capabilities for modeling pebble-bed reactors (PBRs). Verification efforts are documented in this report for these two tools including code-to-code comparisons. The first tool is Griffin [1], which is a Multiphysics Object-Oriented Simulation Environment (MOOSE) [2] based application for reactor physics that has been specially designed for multiphysics modeling of advanced reactor designs. Griffin includes various deterministic methods for neutron transport. The second tool, *kugelpy* [3], is based on Serpent [4] and includes scripts that add functionality for equilibrium core calculations and running-in simulations. Both equilibrium core calculations and running-in simulations are discussed in Section 1.1. Serpent implements the Monte Carlo method for solving transport. Griffin and *kugelpy* implement significantly different methodology for PBR modeling. For this reason, code-to-code studies, where results from benchmark problems produced by the two codes are compared, are particularly valuable as part of verification efforts for the two codes. Differences and details about the modeling methodologies are reviewed in Section 1.2.

1.1. Introduction

This report focuses on high-temperature gas-cooled reactors (HTGRs), and for those reactors, pebbles flow slowly downward and are removed from the bottom of the reactor. PBRs are initially filled with inert graphite pebbles, where resh pebbles are fed into the top of the reactor. The inert graphite pebbles are removed from the bottom of the reactor, and a mix of graphite pebbles and fuel pebbles are added to the top of the reactor. As more fuel is added, the k-eff of the reactor increases, and eventually, criticality is reached. After this, the reactor power is increased while the graphite pebbles continue to be removed and fuel pebbles added. This startup phase of operation is referred to as the running-in phase of operation.

Generally, the fuel pebbles used initially during startup are lower enrichment relative to fuel pebbles that will be used later in plant operation. This is because the average burnup of the fuel is zero when the plant starts and will remain low for the first several hundred days of reactor operation. As the running-in phase continues, the power level is increased towards the nominal rated power for the reactor and the average burnup of the fuel increases. At some point during running-in, the pebble feed in the reactor is switched to entirely fuel pebbles; no more inert graphite pebbles are fed into the reactor. As such, eventually the reactor will be full entirely of fuel pebbles once all the graphite pebbles have flowed out of the reactor.

The average burnup of fuel will continue to increase during the running-in phase and the lower enriched starting fuel will not have enough fissile material to maintain reactivity and higher enriched fuel pebbles will be introduced. Eventually, the reactor will be full entirely of the higher enriched fuel pebbles. This higher enriched fuel is generally called the equilibrium fuel. This is because the running-in phase of operation ends when the equilibrium core configuration is reached, the average burnup of the fuel no longer increases and the reactor is operated at nominal rated conditions. There is a equilibrium between the amount of fuel burned in the reactor and amount of fresh fuel introduced in the feed of pebbles to the reactor. In this work, the lower enriched starting fuel is assumed to have a 5% enrichment and the equilibrium fuel is assumed to have an enrichment of 15.5%.

Developing accurate models to simulate the running-in phase of PBR operation is important for multiple reasons. For example, there are economic motivations for bringing reactor power to the nominal operating condition as quickly as allowable. As another example, some margins on important safety metrics such as the maximum pebble power density may be higher at times during running-in than for the equilibrium configuration.

1.2. Modeling Approach Comparisons Between Griffin And Kugelpy

There are many differences between Griffin and *kugelpy*, but the differences that are most important for this work can be put into two categories; differences in the transport solvers and differences in the modeling of pebble movement. Difference in the transport solvers will be discussed first.

Griffin uses deterministic methods for transport while *kugelpy* is based on the Serpent code, which uses a Monte Carlo method for transport. One important difference between these two methods is that the Monte Carlo method more easily allows fine detail to be modeled. As will be discussed further in Section 1.3, *kugelpy* models can include each individual pebble in the PBR core. While a similar modeling approach could be possible in Griffin, it is more challenging and not supported by the Griffin modeling approach discussed in this work. Instead, the core is meshed into volumes much larger than the size of a single pebble, and many pebbles are averaged together into a homogenized material that is used in the simulation. The *kugelpy* model is more detailed and should be more accurate, so this work can be seen as verifying the more approximate Griffin modeling approach against the higher fidelity *kugelpy* model. It is noted here that the Griffin simulations will use multigroup diffusion in this work. S_N transport can also be used for PBR analysis, and it may be valuable in the future to compare multigroup diffusion with S_N solutions. Since control rods are not used in this work, the multigroup diffusion solution should be sufficiently accurate to produce meaningful benchmark study results.

While the Griffin model lacks detail relative to the *kugelpy* model, the main reason it's useful is that it can be run quickly on modest computational resources and easily incorporates multiphysics. Multiphysics running-in simulations were first demonstrated with Griffin in [5], with a more realistic model being demonstrated in [6]. It is much more difficult to include multiphysics in the *kugelpy* model. A multiphysics running-in simulation with *kugelpy* was demonstrated in [7], but *kugelpy* was used to generate the isotopic composition in the core at various times, and these compositions were passed to Griffin, which was used to perform a multiphysics calculation. Especially for running-in simulations, the primary reason to use Griffin is its ability to perform multiphysics simulations quickly. This work does not include multiphysics verification as the basic methodologies used by Griffin need to be verified as a first step.

A second important difference between the deterministic transport method in Griffin and the Monte Carlo method used in *kugelpy* is that a multigroup cross section dataset needs to be created to use Griffin. Monte Carlo is able to use the physical cross section data while using a multigroup cross section involves some approximations. This difference and its effect on the verification work is discussed in more detail in Section 2.1.1.

The second significant different between Griffin and *kugelpy* is how pebble movement is modeled. Neither code models pebble movement at the level of detail of a discrete element method (DEM) code, but the approximations used are different. Griffin uses an Eulerian approach to solving the conservation equations as described in detail by Schunert et al. [8] while *kugelpy* uses a Lagrangian approach [9]. Both approaches have benefits and drawbacks. The Eulerian approach is more complicated mathematically and suffers from some numerical issues like numerical diffusivity while the mathematically simpler Lagrangian approach can naturally track a sharp interface. This is discussed further in Section 2.2. The Eulerian approach used in Griffin allows simpler time stepping, the Lagrangian approach in *kugelpy*, as explained in Reference [9], leads to a time step that is integral with the size of the mesh used; only discrete time steps can be taken.

1.3. Code-to-Code Benchmark Model Descriptions

As discussed in Section 1.2, there are considerable differences between the Griffin and *kugelpy* modeling approaches. This makes code-to-code comparisons valuable but also difficult, especially for running-in simulations, which are complicated by the many different ways they could progress. To make the code-to-code comparison more tractable, simplified models based on the 200 MW General Pebble Bed Reactor (GPBR200) design were developed in Griffin and *kugelpy*, respectively. These models will be referred to as the simplified 200 MW General Pebble Bed Reactor (sGPBR200). These simplified models cannot be identical because of the differences between the two codes, but they are made equivalent in important areas for comparison. It is noted that both codes in this comparison work have been used successfully for full running-in simulations with realistic HTGR models [6, 7, 9]. This section documents details of sGPBR200 models used to generate the comparison results in presented in Section 2.

The Griffin model used for the comparisons is shown shown in Figure 1b, and the model used for the Serpent-based code is shown in Figure 2. For reference, the Griffin model used in [6] is shown in Figure 1a, which is based on a model that can be found on the Virtual Test Bed (VTB) [10] (`https://mooseframework.inl.gov/virtual_test_bed/htgr/generic-pbr-tutorial/index.html`). Note the model on the VTB is a Pronghorn-only model. It does not include Griffin, and a simple function is used as the assumed heat source in the VTB model. A Griffin model was added to this VTB in [6]. The core and reflector dimensions are similar between the two models shown so the conclusions from code-to-code comparisons in this work should be physically meaningful.

For easy reference, some dimensions for the sGPBR200 benchmark model used in this work are shown in Table 1. This table also shows the constant temperatures used for all studies. The porosity shown is also constant throughout the core. An important component missing from the sGPBR200 model is control rods. Control rods will have to be investigated in the future after the basic validity of the running-in algorithms have been documented.

Table 1. Model parameters for the sGPBR200.

Parameters	Value (unit)
Core Height	8.75 (m)
Core Radius	1.2 (m)
Side Reflector Thickness	86 (cm)
Bottom Reflector Thickness	58 (cm)
Top Reflector Thickness	86 (cm)
Reflector Temperatures	650 (K)
Fuel and Moderator Temperatures	900 (K)
Porosity	0.3915

The streamlines used in the Griffin model are shown with yellow lines in Figure 1b. The axial discretization of each streamline exactly matches the mesh cells shown. There are five columns of cells shown in the mesh for the core region in Figure 1b and three streamlines. The first two columns of mesh cells are collected by the first streamline, the next two columns are collected by the second streamline, and the final column of cells goes with the outer streamline. The flow velocity for the pebbles is assumed constant for all streamlines. The *kugelpy* model also assumes constant pebble flow velocity across the core and uses three core channels and 35 axial volumes. These channels are similar to the streamlines in Griffin except that a different modeling approach is used to move the pebbles along the channels as described in Section 1.2.

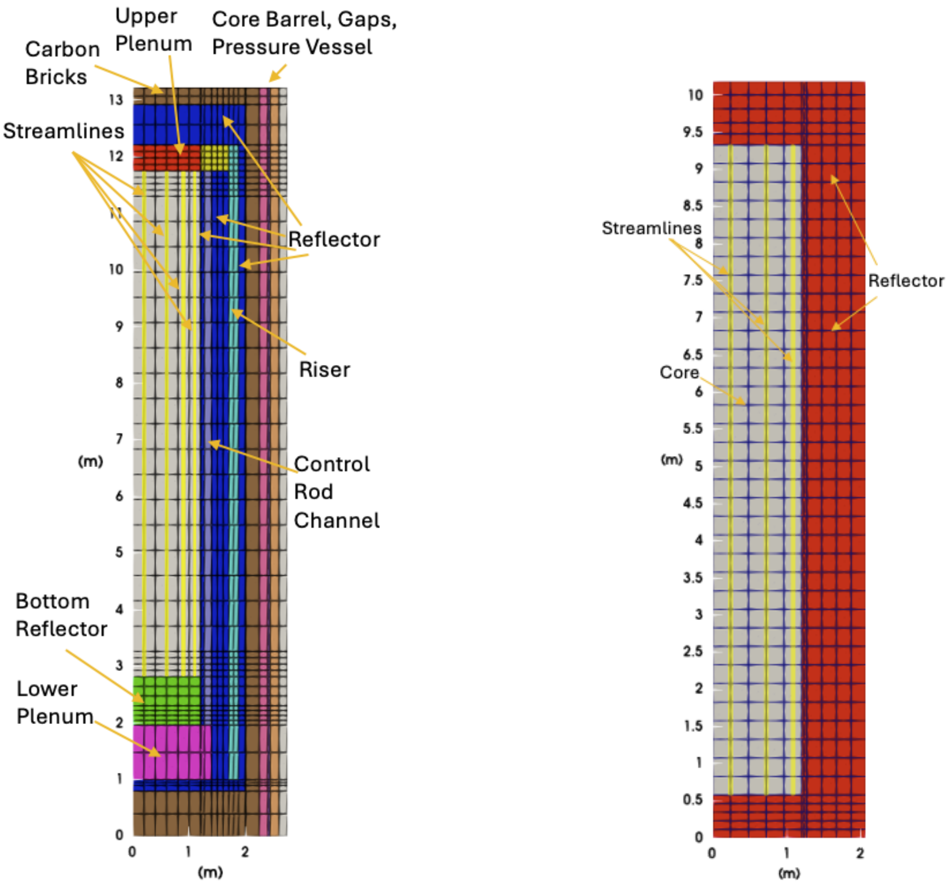

(a) (b)

Figure 1. (a) A schematic of an RZ-geometry Griffin model where the streamlines used for pebble depletion are marked with yellow lines and (b) the simplified version of the model used for the code-to-code comparison studies.

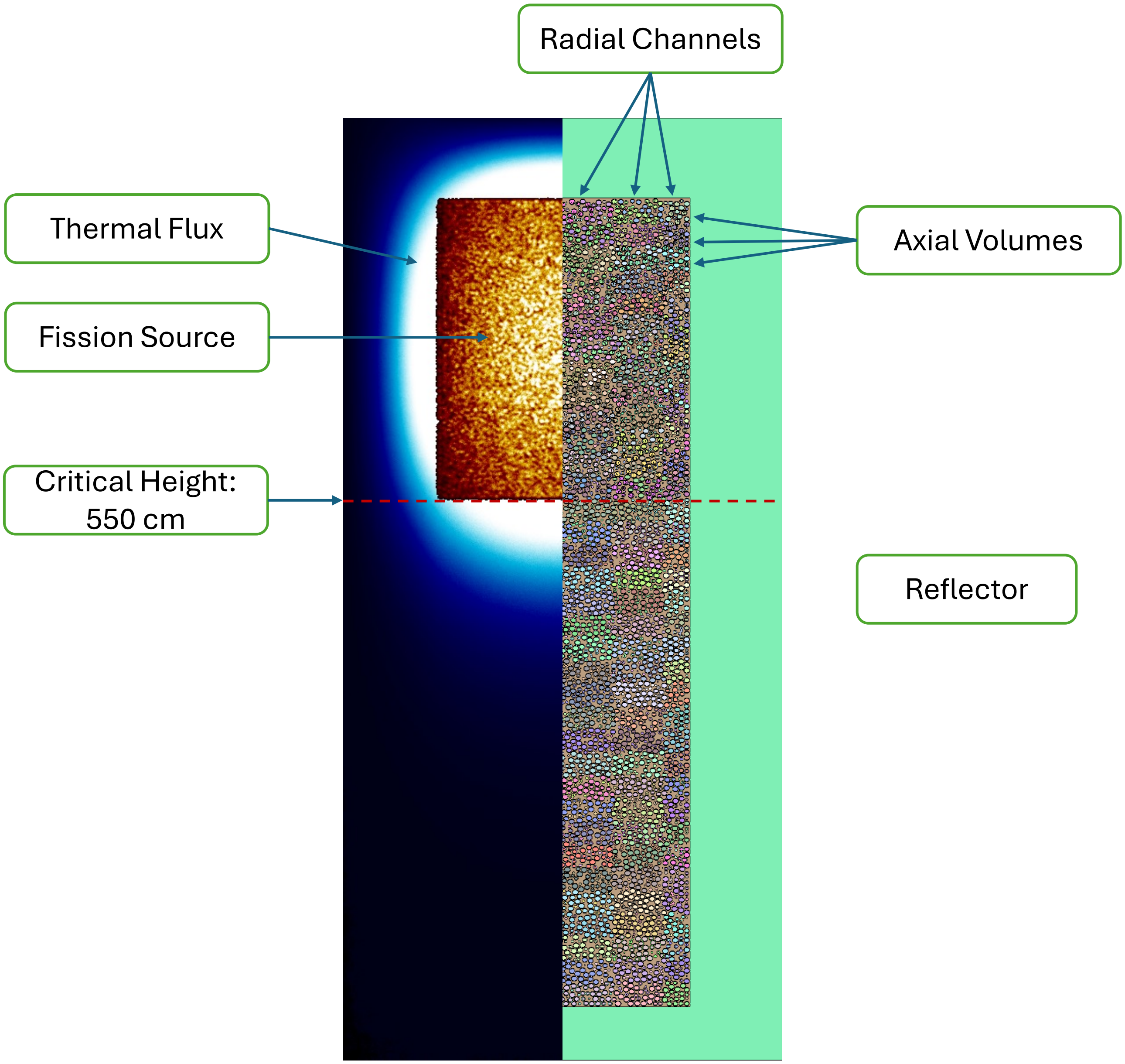

Figure 2. Simplified Serpent core geometry for a critical core. The critical core height is also shown, see Section 1.4.2 for more details.

.

1.4. Standalone Numerical Studies

This section documents verification-related studies for the running-in capability of *kugelpy* and Griffin, respectively. The studies documented in this section are "standalone" while the code-to-code comparison studies are documented in Section 2.

1.4.1. Kugelpy Convergence Studies

A convergence study on the axial mesh was performed with the Serpent model. This study examined the effect of the axial mesh (and corresponding time steps) on k-eff, the maximum pebble power, and discharge burnup for the running-in problem. Table 2 shows the running-in parameters used here. Of particular note is that the graphite fraction slowly reduces from 0.4 to 0.2 over the course of the convergence study. The removal of graphite allowed for a continually changing core over time, which is present in future simulations.

Figures 3–5 show the behavior of k-eff, the maximum pebble power, and the discharge burnup for the axial volume convergence. Overall, the use of axial regions has limited effects on k-eff, the maximum pebble power, and the discharge burnup for the simplified convergence study. It is assumed that more axial volumes reduces potential biases in operational parameters.

For k-eff, reducing the axial zones from 70 to 25 volumes introduces a bias of −100 pcm on average over the life of this problem. For the maximum pebble power, the mean values overlap for the entirety of the problem and are well within the given uncertainty. The discharge burnup exhibits the largest perceived difference, where pebbles in the 25 axial regions show slightly higher burnup. This is an artifact of the limited axial volumes, which results in pebbles being left in the core for slightly longer on average, resulting in a higher burnup. The difference in burnup is less than 0.01 MWd/kg for this lower power case; the difference would likely grow at higher power levels.

Given the limited difference found between 35 and 70 axial volumes, a total of 35 axial volumes was selected for future studies.

Table 2. Convergence study running-in parameters for sGPBR200.

Parameters	Value (unit)
Power	1 (MW)
Pebble Discharge Rate	0.666 (pebbles per minute)
Core Temperature	900 (K)
Reflector Temperature	900 (K)
Time Step	[10.9,6.23,4.36,3.15](days)
Axial Volume	[25,35,50,70]
Radial Channels	3
Reflector Density	8.824e-02 (b/cm)

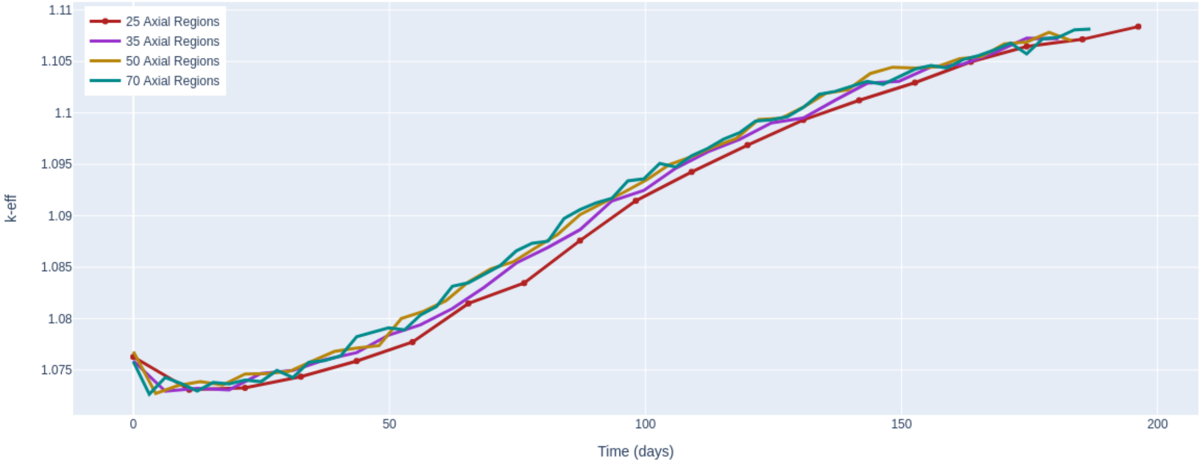

Figure 3. Critical eigenvalue for the axial convergence study.

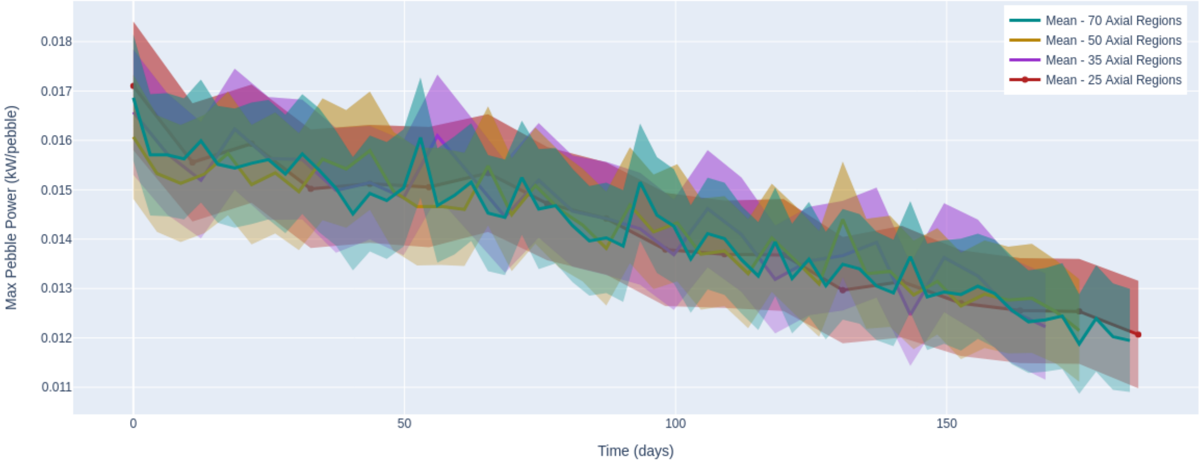

Figure 4. Maximum pebble power for the axial convergence study.

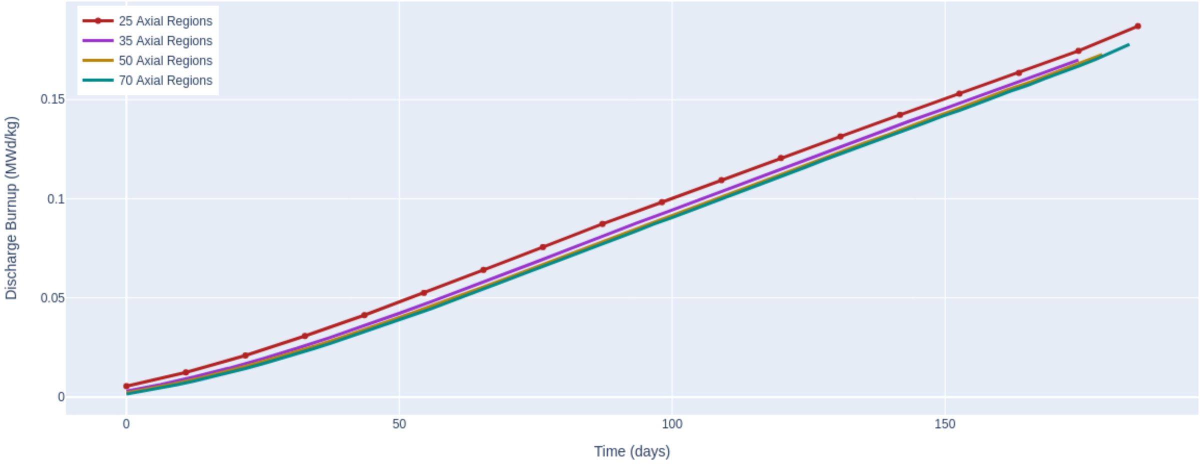

Figure 5. Discharge burnup for the axial convergence study.

1.4.2. Kugelpy Critical Height Study

The critical core was determined by adjusting the height of the interface between the pure graphite fuel pebbles and the 60% fuel pebble 40% graphite pebble region. This is performed using the *kugelpy* model, where multiple simulations with varying critical heights were examined and a linear interpolation technique was used until a critical height was found [3]. The critical core height for the sGPBR200 was 550 cm; meaning there is 325 cm of the fuel and graphite pebble mixture. Figure 2 shows the critical core height and corresponding fission source and thermal flux for the critical core.

1.4.3. Griffin Time Convergence Study

The equilibrium core calculation capability in Griffin provides a useful tool for verifying the running-in algorithms. Griffin uses a direct method to compute an equilibrium core instead of a “jumping-in” algorithm. This means that the time derivatives in the conservation equations are set to zero and the equations solved directly instead of solving the transient equations until some steady-state condition is reached. The only difference then between a running-in simulation result at equilibrium and a direct equilibrium calculation result is the discretization error from the time derivative. The difference between these two results can be used to perform a convergence study in time.

A running-in result at equilibrium was compared to a direct equilibrium result in Reference [11], but no convergence study was performed. The difference between the two calculations was relatively small for a single time step value in the running-in calculation. A time convergence study provides significantly more confidence in the verification and was performed for this work. Since forward Euler is currently implemented for the running-in equations, the difference between these two results should diminish in a first-order way with respect to the time step. Figure 6 shows the results for the time convergence study with three data points plotted along with a trend line for the first-order trend result. The data points nearly align exactly with the first-order trend line indicating the time integration algorithms for the running-in simulation are implemented correctly.

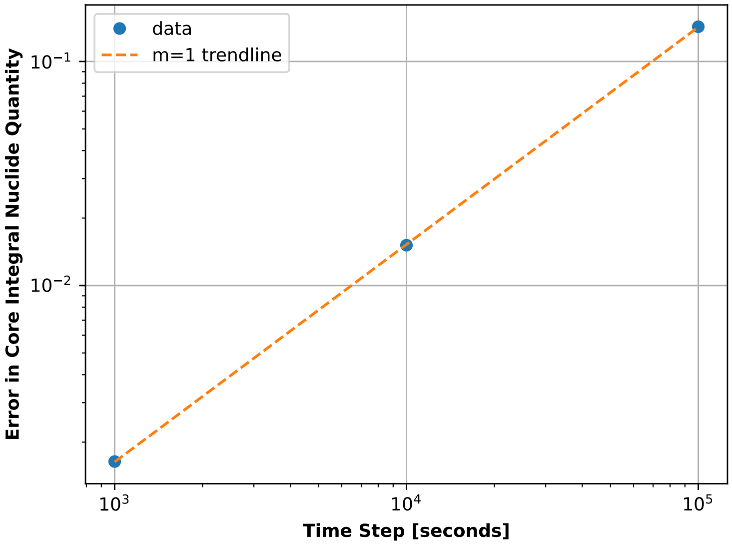

Figure 6. Error in a converged running-in simulation compared to the direct equilibrium result shown for three different time step values with a slope = 1 trend line.

2. KUGELPY-TO-GRIFFIN COMPARISON STUDIES

The running-in phase of PBR operation is reviewed in Section 1.1. Many of the complexities of running-in simulations, for example determining the appropriate control rod position and pebble feed rate over time, need to be simplified for these initial running-in verification studies. The purpose of these studies is to verify the basic modeling approach in Griffin compared with the more detailed modeling capabilities of *kugelpy*. This can provide a basis for confidence in more complex multiphysics running-in simulations later. Multiple simplified running-in simulations were constructed in Griffin and *kugelpy* and results were compared. The specific simulations are documented in the following subsections. All of the simulations use the model described in Section 1.3. Also common to all studies is the use of once-through-then-out (OTTO) cycles. Verifying the basic running-in algorithms is much simpler for the OTTO cycle, and cases with recycling can be investigated in future.

2.1. Homogeneous Core Pebble Inventory Studies

As discussed in Section 1.1, when the reactor goes critical and power starts increasing, the reactor will be filled with inert pebbles to some elevation and then above this elevation will be a mix of fuel and graphite pebbles. This interface between the two material regions (fueled and nonfuel) moves downward as the graphite pebbles are removed and is generally a sharp. An example of this is shown in Figure 2, where the region with a fission source has fuel and there is a sharp interface below which there are only inert graphite pebbles. Modeling this configuration introduces complexities relative to modeling the equilibrium core where there is only one pebble type, the equilibrium fuel. Previous work has already investigated verifying equilibrium core calculations [12]. As an initial test, configurations are tested where there is a homogeneous composition of pebbles in the core during a running-in-like simulation. The two tests, described in detail in the following two subsections, involve a fixed homogeneous pebble mixture of 40% inert graphite pebbles and the balance of starting 5% starting enriched fuel pebbles.

Table 3. Running-in parameters for sGPBR200.

Parameters	Value (unit)
Constant Power	25 (MW)
Pebble Discharge Rate	2 (pebbles per minute)
Time Step	2.11 (days)

2.1.1. Initial Homogeneous Core

The multigroup cross sections used in this work for the Griffin model were generated for an equilibrium core configuration and may not be ideal for running-in simulations. These cross sections were generated with a similar methodology to that described in Reference [13]. Griffin now includes an online cross-section capability [14], which will be implemented for running-in simulations in the future. However, this work is limited to use of the pregenerated multigroup library. To first investigate whether the pregenerated library was appropriate for mixtures of graphite and fueled pebbles, the k-eff of a homogeneous core of 40% inert graphite pebbles and the balance of fresh 5% enriched fuel pebbles was compared between Griffin and *kugelpy*.

kugelpy predicts a k-eff of 1.07590 ± 0.00036, and the Griffin prediction is 1.07283, which is lower by approximately 300 pcm. Given that the purpose of this test is to verify that the multigroup cross-section library developed for an equilibrium core can be reasonably used for the running-in code-to-code comparisons, this difference is acceptable.

2.1.2. Homogeneous Core Running-In

The previous section included only an eigenvalue calculation result. This section builds on the simple homogeneous core problem by adding a simple running-in simulation. Again, the core is made up of 60% fuel pebbles and 40% inert graphite pebbles. The fuel pebbles are 5% enriched. Then, the power is set to 25 MW and a running-in simulation is started with the parameters shown in Table 3. The composition of pebbles fed into the reactor is constant over time and consists of 60% fuel pebbles and 40% inert graphite pebbles. In this way, the fraction of graphite pebbles and fuel pebbles in the core is constant over time. When the pebbles leave the bottom of the reactor, they are all discarded; there is no pebble recycling in this benchmark.

Figure 7 shows the k-eff predicted by *kugelpy*. The core begins with a large amount of excess reactivity (approximately 3,000 pcm higher than equilibrium) due to all fuel pebbles being fresh fuel. Excess reactivity is rapidly reduced and reaches equilibrium around 60 days. The quick transition to equilibrium is attributed to the OTTO cycle being used; fuel can only pass through the core once. Uncertainty in k-eff is under 50 pcm.

The k-eff values predicted by Griffin are shown in Figure 8. The test in this section is meant to investigate whether the multigroup cross-section library used by Griffin is appropriate for burned fuel. The predictions for the k-eff after the core is at equilibrium are similar between Griffin and *kugelpy* and the drop in k-eff from the initial value to the equilibrium value are also similar. This provides some confidence that the multigroup library used in this work can reasonably be used for these simple running-in benchmark studies.

Figure 9 shows the behavior of the maximum pebble power predicted by *kugelpy*. The maximum pebble power hovers around 0.39 kW/pebble with little change to the mean. The uncertainty in the pebble power is due to the Monte Carlo nature of Serpent, and the fact that each pebbles power is calculated independently. The power of each pebble is measured where the maximum pebble power is presented. Given the large amount of pebbles in the core, additional particle histories would be necessary to reduce the uncertainty further; however, this was not deemed necessary for this level of study.

The maximum pebble power predicted by Griffin is shown in Figure 10. The predicted maximum power by Griffin is at the lower band of the predicted range from the *kugelpy* model. Since the maximum power is low and nearly constant, it seems sufficient to note only that the Griffin result is approximately within the

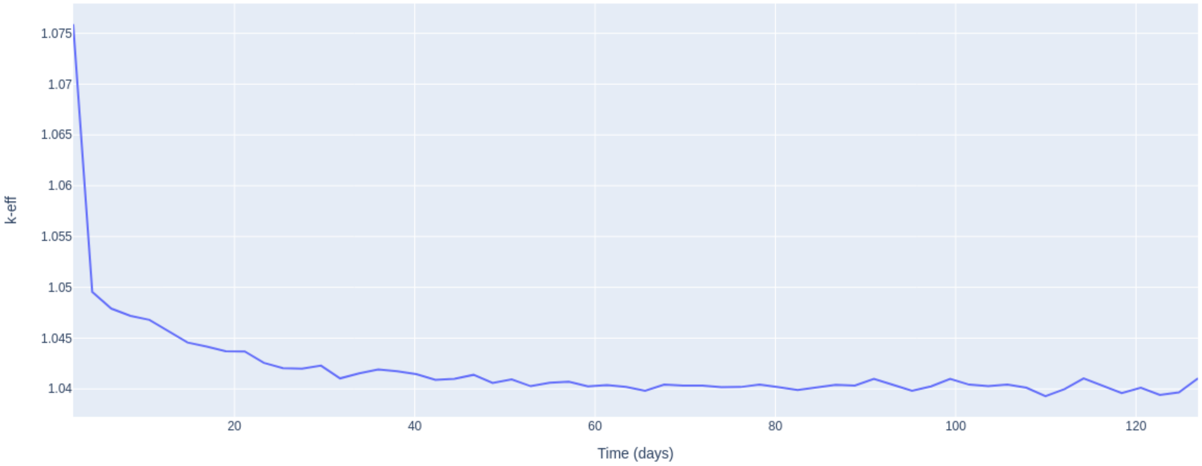

Figure 7. Critical eigenvalue for the homogeneous running-in process predicted by *kugelpy*.

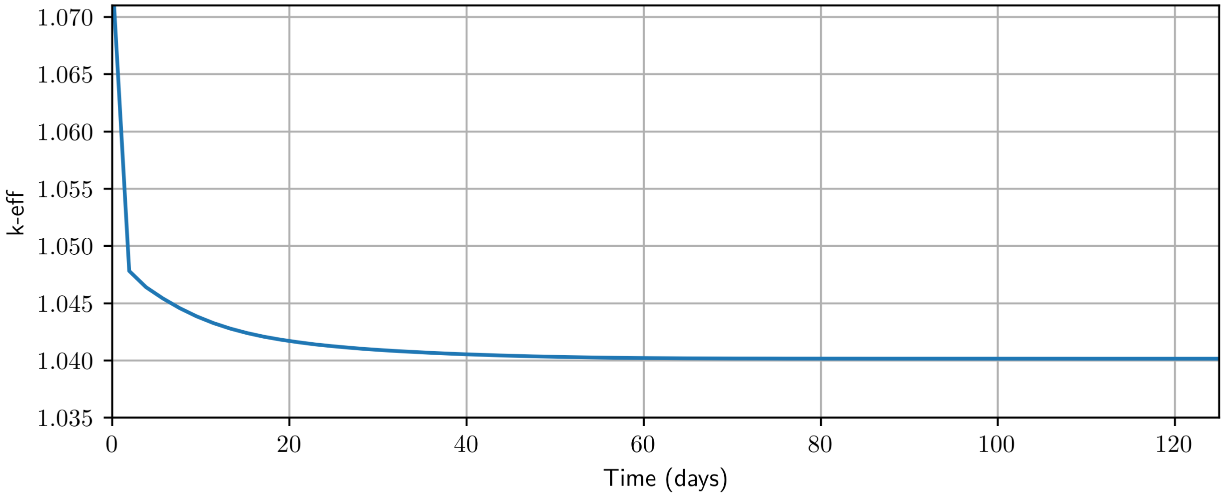

Figure 8. Critical eigenvalue for the homogeneous running-in process predicted by Griffin.

range predicted by *kugelpy*. The maximum pebble power is discussed further in Section 2.2.2, where the injection of higher enriched fuel pebbles later in the simulation leads to a significant spike in the maximum pebble power.

Figure 11a shows the flux profile in the core at equilibrium predicted by both Griffin and *kugelpy*. Unlike the traditional running-in process, flux peaking occurs near the center of the core both axially and radially. However, this initial benchmark case stops the running-in simulation while the core still contains 40% inert graphite pebbles. A normal OTTO cycle equilibrium core will have power peaking towards the top of the core. Figure 11a shows that similar flux profiles are predicted by the two codes.

The discharge burnup of the fuel predicted by *kugelpy* is shown in Figure 12. Over the running-in process, the burnup converges to about 2 MWd/kg at around 70 days. This follows the same time frame as k-eff for converging to an equilibrium value. A equivalent plot is not made for the Griffin results. The Griffin model only uses 11 burnup bins. The burnup value for each burnup bin is assumed to be the mid-point of the bin. Therefore, the first burnup bin already has a non-zero burnup. For a practical running-in simulation where the

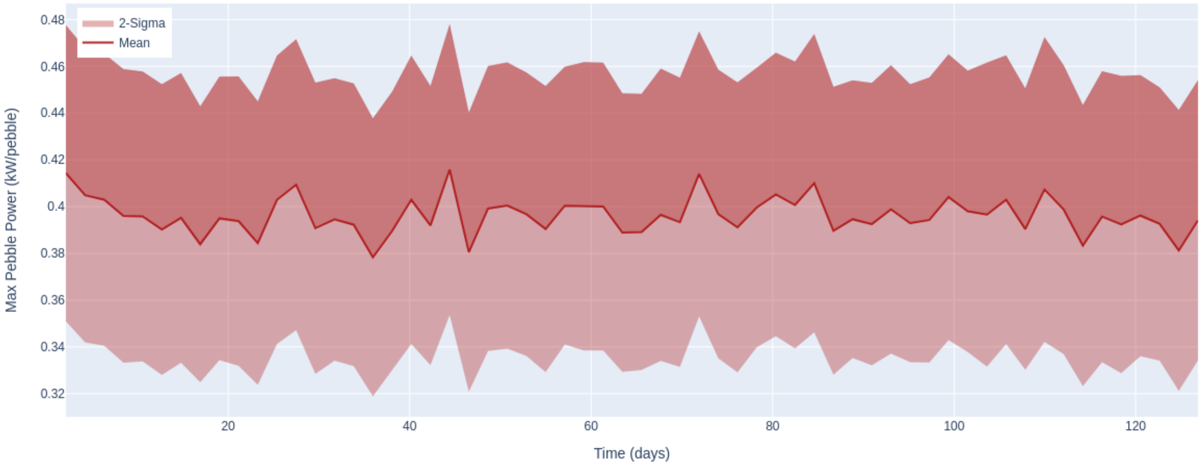

Figure 9. Maximum pebble power for the homogeneous running-in process predicted by *kugelpy*.

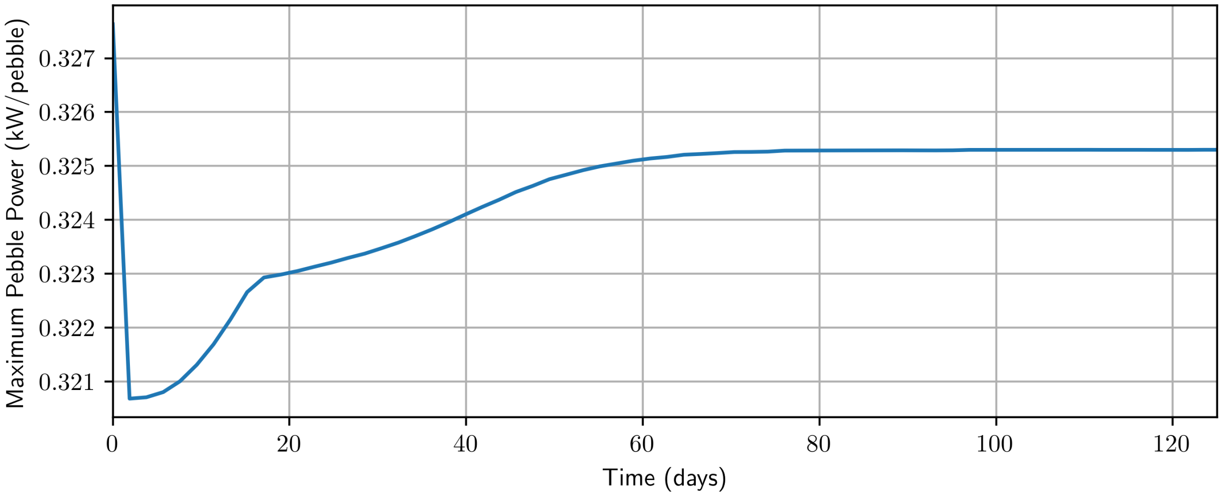

Figure 10. Maximum pebble power for the homogeneous running-in process predicted by Griffin.

burnup of the pebbles rapidly increases, the coarse 11 burnup bin grouping still leads to accurate calculations [6]. However, in this simple running-in test problem, the power is held at 25 MW and an OTTO cycle is used so the burnup remains very low throughout the simulation. The Griffin results for predicted discharge burnup are not as meaningful in this case. But the *kugelpy* is still shown for reference.

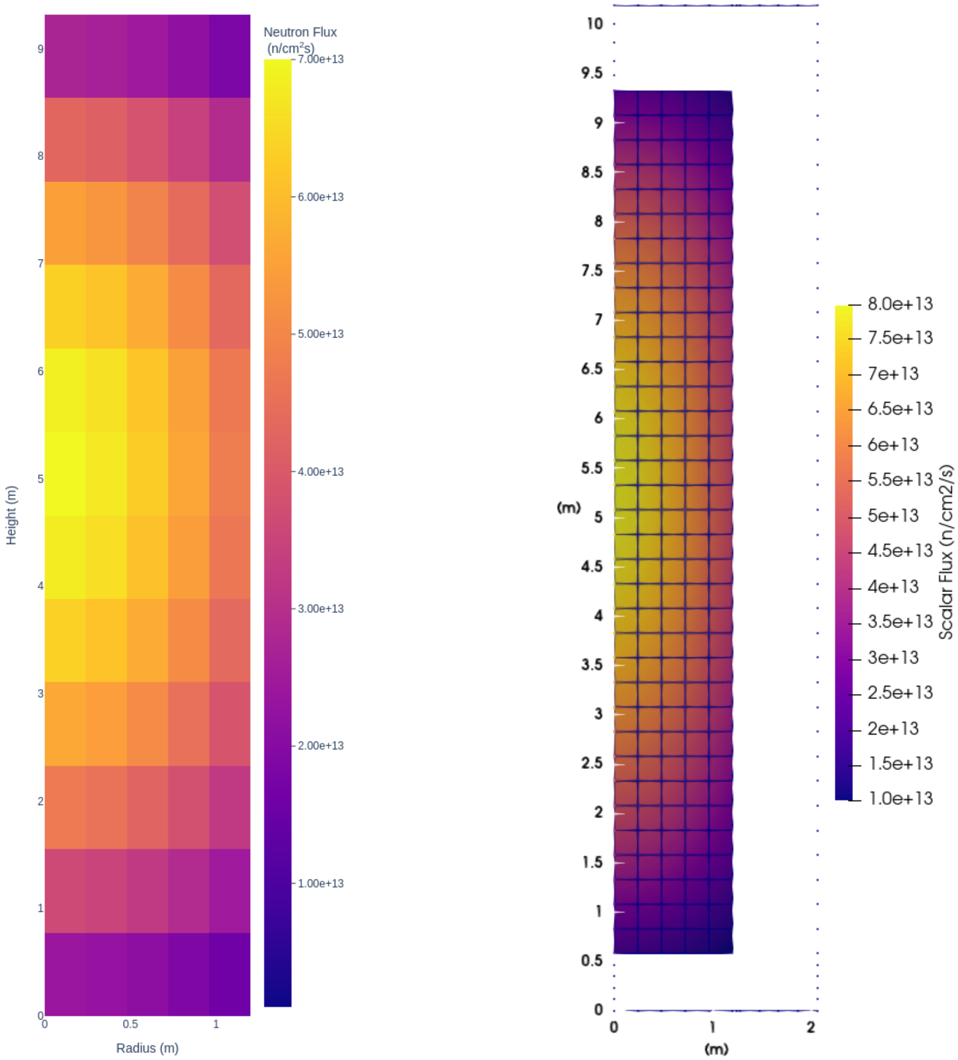

(a) *kugelpy*

(b) Griffin

Figure 11. Flux profile in the core region for the homogeneous running-in process (a) predicted by *kugelpy* and (b) predicted by Griffin.

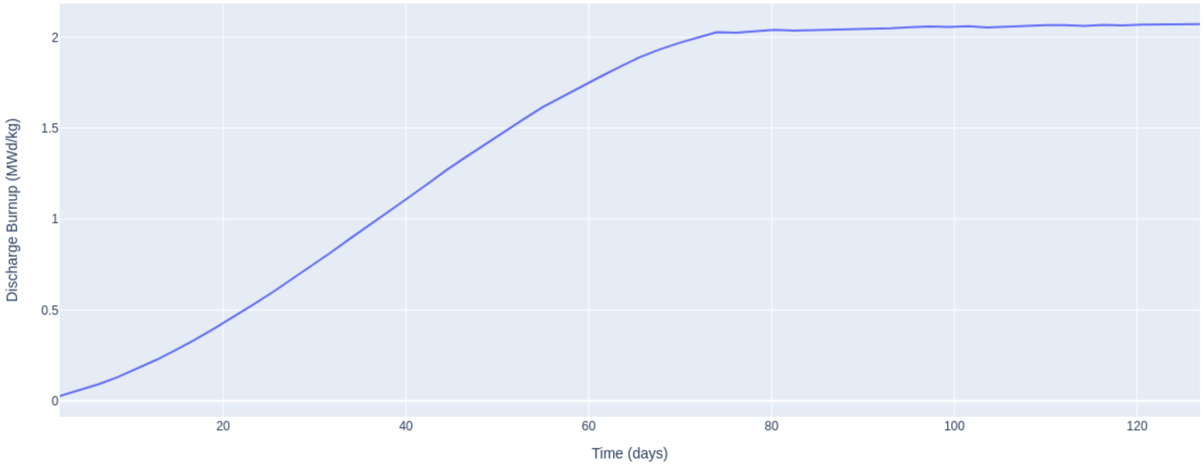

Figure 12. Discharge burnup for the homogeneous running-in process predicted by *kugelpy*.

2.2. Running-In From An Initial Sharp Interface Studies

As discussed in previous sections, actual running-in operations will start from a configuration where there is a bottom layer of inert graphite pebbles below a layer of mixed fuel and graphite pebbles. This configuration adds a complexity not present in the equilibrium core modeling, a sharp interface between materials in the core. As discussed in Section 1.2, *kugelpy* uses a Lagrangian approach to model conservation equations while Griffin uses an Eulerian approach. In particular, the spatial discretization currently used in Griffin, as discussed in detail in Reference [8], is numerically diffusive relative to more sophisticated spatial discretizations. This means that a sharp interface will diffuse and there is currently no way to model a sharp interface with Griffin. This can be seen in Figure 18, which is discussed further in the next section. *kugelpy*, on the other hand, can naturally model a sharp interface. To determine what significant impacts, if any, there are to modeling the sharp interface correctly, Griffin and *kugelpy* results are compared for several simplified running-in simulations starting from a sharp interface.

The first test presented in Section 2.2.1 starts from a sharp interface and includes only graphite pebbles and 5% enriched starting fuel. The second and third tests, in Sections 2.2.2 and 2.2.3, respectively, start the same as the test presented in the previous section, but at 80 days, equilibrium fuel is introduced. The equilibrium fuel is assumed to be 15.5% enriched and could generally be referred to as high-assay low-enriched uranium (HALEU). In this report, we will use the term equilibrium fuel. The test presented in Section 2.2.2 involves injecting a mixture of 60% equilibrium fuel and the balance inert graphite pebbles at 80 days, and in Section 2.2.3 the injection at 80 days is set to be 100% equilibrium fuel fuel.

2.2.1. Sharp Interface with Starting Fuel Only

The first study builds on that discussed in Section 2.1.2, except that this time, the problem starts from a sharp interface. The feed is still held at 40% graphite pebbles and the balance starting fuel throughout the running-in simulation. The simulation was started from 600 cm above the bottom of the core. Figure 13 shows the pebble composition in the core throughout the running-in simulation for both the Griffin and *kugelpy* models. The k-eff predicted by *kugelpy* is shown in Figure14, and the same result predicted by Griffin is shown in Figure15; the k-eff generally shows good agreement.

The maximum pebble power predicted by *kugelpy* is shown in Figure16, and the same result predicted by Griffin is shown in Figure17. The maximum pebble power begins at 0.85 kW/pebble as there is a constant

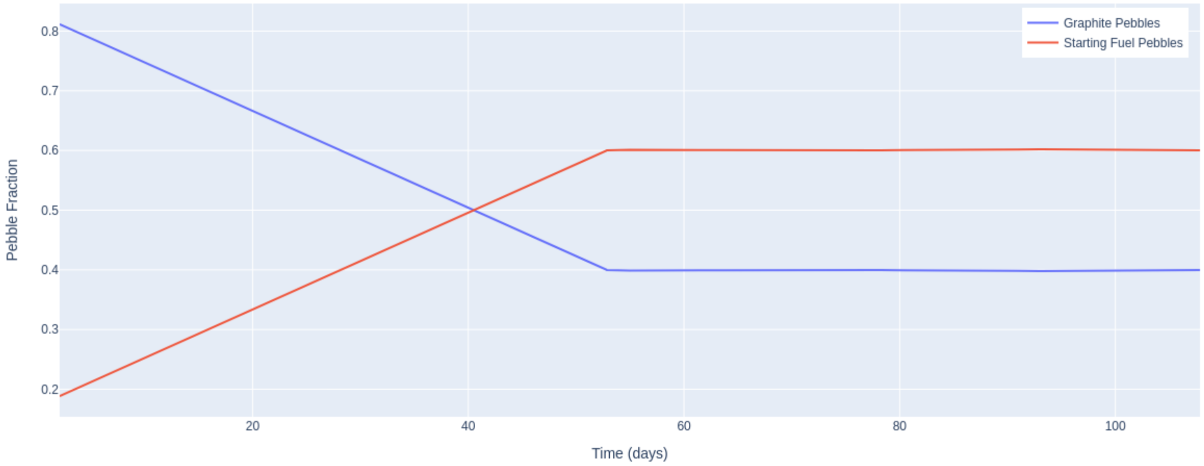

Figure 13. Fraction of starting fuel and graphite pebbles for the running-in process starting with a critical core. This result is the same for both the Griffin and *kugelpy* model.

power but fewer pebbles to spread the power across. Once additional fuel is added, the maximum pebble power converges to the homogeneous maximum pebble power of of 0.38 kW/pebble with little change to the mean. As with the result presented in Section 2.1.2, the predicted maximum power from Griffin is within the range predicted by *kugelpy* but on the lower bound of the predicted range.

A key modeling difference between *kugelpy* and Griffin is depicted in Figure 18, which shows the downward movement of pebbles as modeled by Griffin. There should be a sharp interface between the lower region of inert graphite pebbles and the upper region of mixed graphite and fuel pebbles. However, the interface diffuses in the Griffin model as shown in Figure 18. The same *kugelpy* results are not plotted, as there is no purpose for this; the sharp interface simply moves down and remains a sharp interface. The results in this section highlight an important aspect of the running-in simulation relative to this sharp interface, which is that the power being produced near the sharp interface is lower since it is like a boundary of the fueled region. This is likely why there is generally good agreement between the Griffin and *kugelpy* models, despite Griffin not tracking the sharp interface exactly as *kugelpy* is able to.

Figures 19 and 20 show the flux profile in the core and the discharge burnup of the fuel, respectively. The discharge burnup is only shown for *kugelpy* for the reasons described in Section 2.1.2. Figure 19 shows both the critical core (Figure 19a), where the flux is about twice as high due to fewer pebbles being present in the core. Figure 19b is nearly identical to Figure 11a as both problems have converged to the same core. The Griffin result equivalent to Figure 19b is not shown since it is the same as that from Section 2.1.2.

The burnup of the fuel exhibits a different behavior as the fuel that begins in the core accrues a higher burnup. This is again tied back to the higher flux seen in Figure 19a. Figure 20 shows the behavior of the sGPBR200 over the 120 days of the running-in process starting from critical as predicted by *kugelpy*. Once the initial fuel has been discharged, the burnup converges to the homogeneous running-in burnup of 2 MWd/kg.

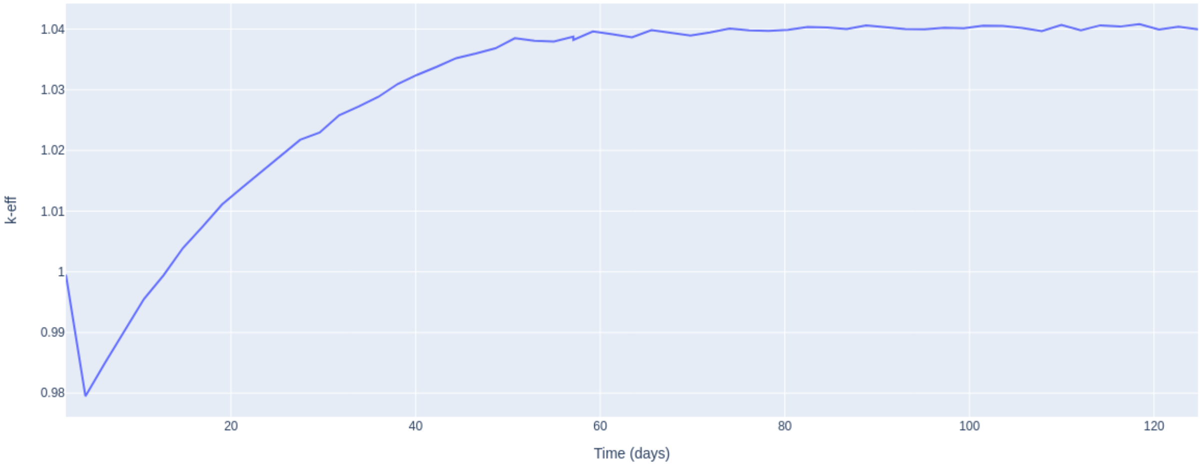

Figure 14. Critical eigenvalue for the the running-in process starting with a critical core height of 600 cm predicted by *kugelpy*.

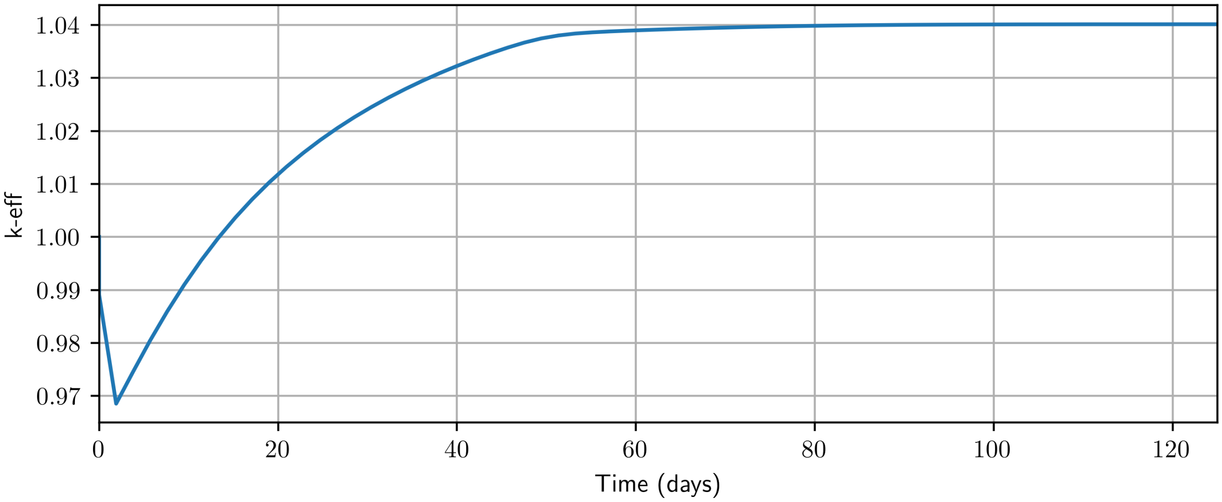

Figure 15. Critical eigenvalue for the the running-in process starting with a critical core height of 600 cm predicted by Griffin.

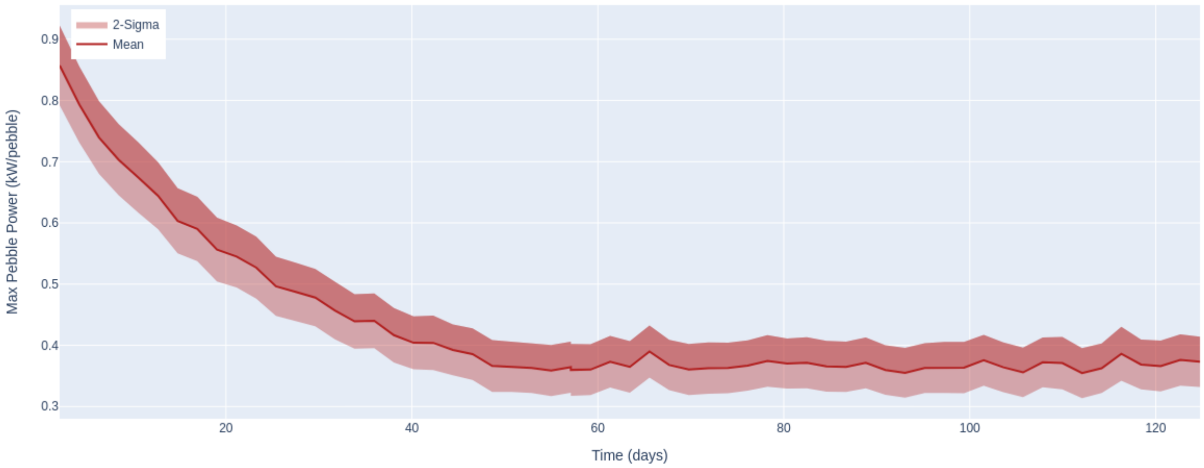

Figure 16. Maximum pebble power for the running-in process starting with a critical core height of 600 cm predicted by *kugelpy*.

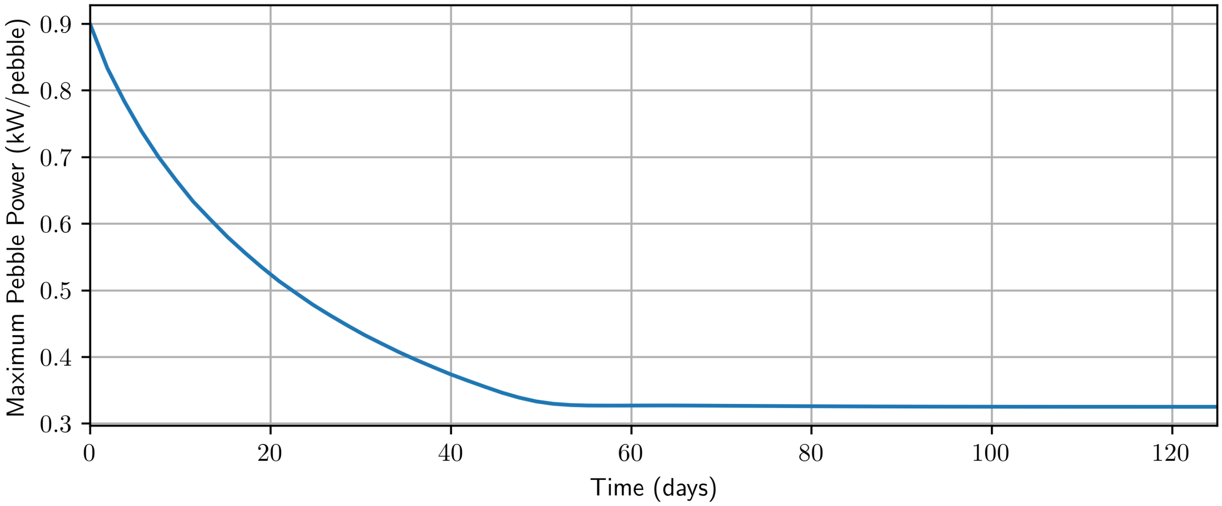

Figure 17. Maximum pebble power for the running-in process starting with a critical core height of 600 cm predicted by Griffin.

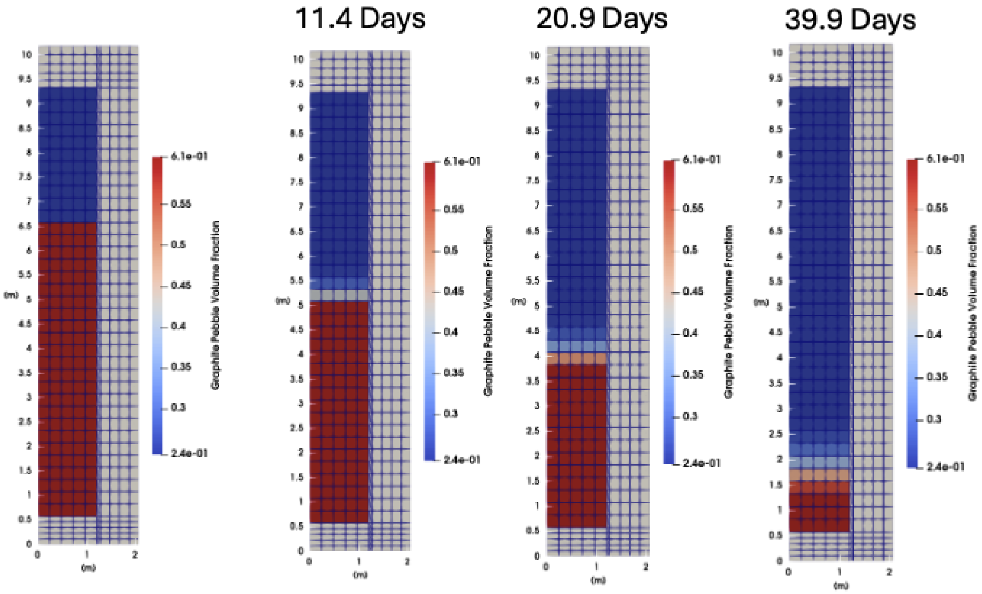

Figure 18. Volume fraction of graphite pebbles predicted by Griffin. The volume fraction is the volume of total space occupied by the pebble type. Since the porosity is 0.3915, the red region at the bottom of the core is entirely inert graphite pebbles.

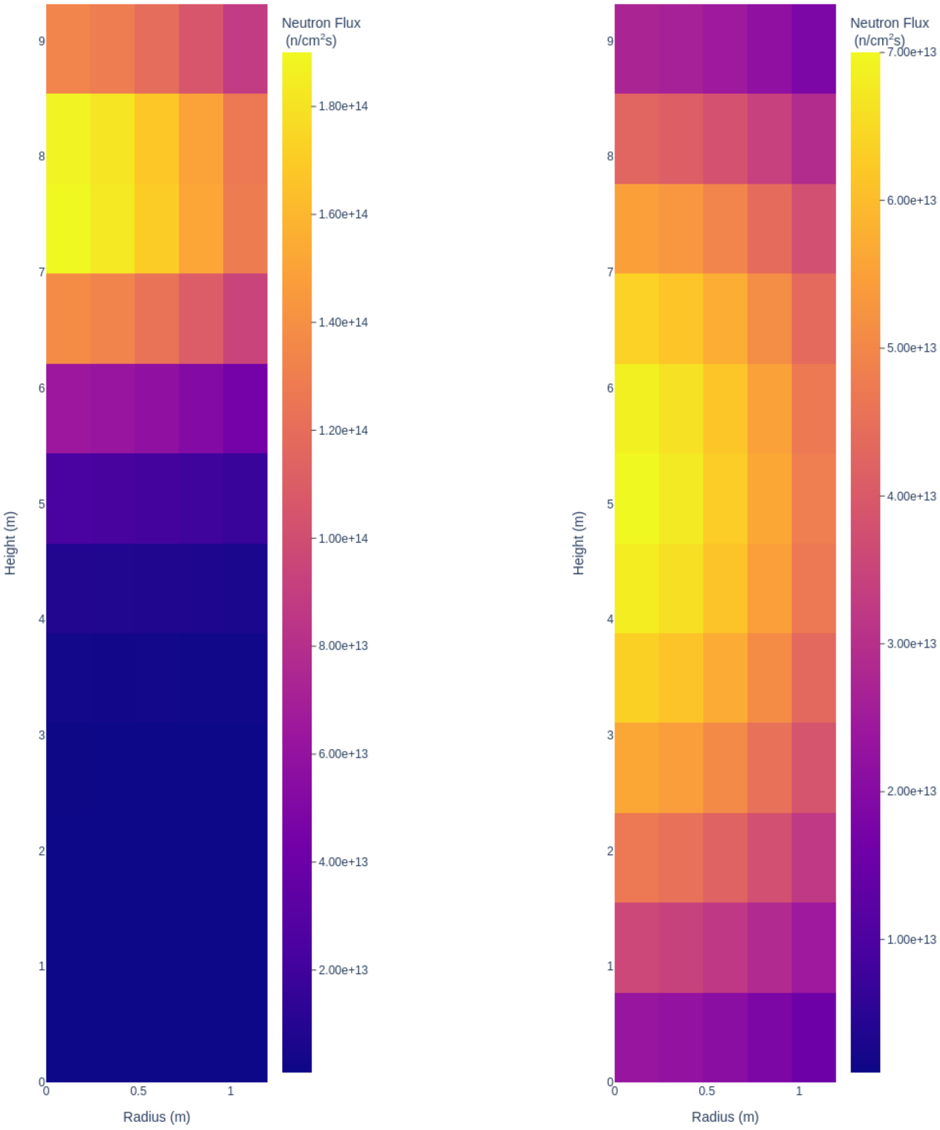

(a) Critical core height from *kugelpy*

(b) *kugelpy* equilibrium core

Figure 19. Comparison of the flux profile for the critical core and equilibrium during the running-in process.

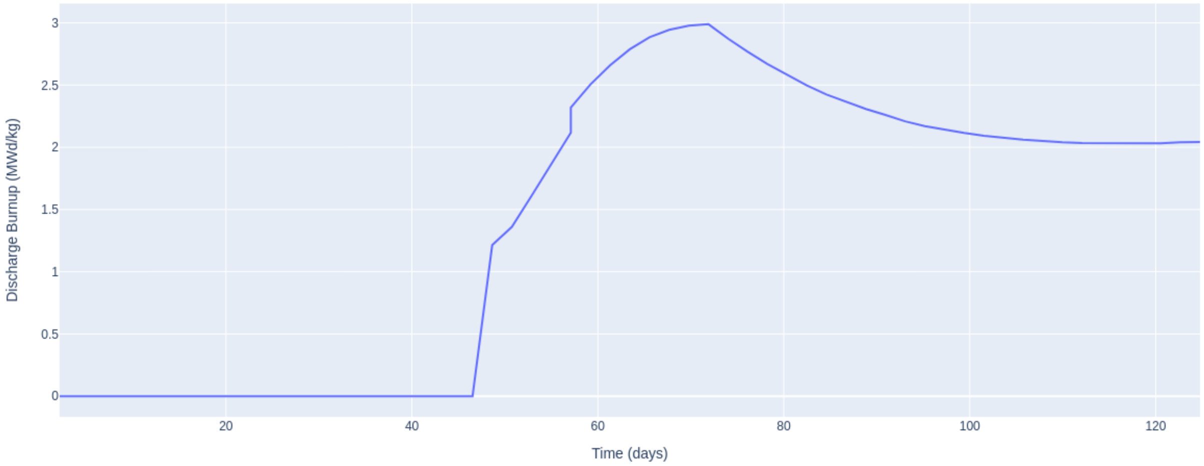

Figure 20. Discharge burnup for the running-in process starting with a critical core height of 600 cm predicted by *kugelpy*.

2.2.2. Injection of Equilibrium Fuel I

This study starts the same as the running-in scenario in Section 2.2.1. The major difference is that at approximately 82 days, the startup fuel and graphite pebbles are replaced with equilibrium fuel and graphite pebbles. Figure 21 shows the transition from a critical core with nearly 80% graphite pebbles to the equilibrium fraction of 40%.

Figure 22 shows the core beginning at a k-eff at roughly 1.00, where a sharp decrease is seen within the first 5 days due to the constant power of 25 MW and a relatively small amount of fuel pebbles. After this, there is an approach to an equilibrium k-eff from 5 to 60 days; equilibrium k-eff is approximately 1.04. Uncertainty in k-eff is under 50 pcm. At roughly 80 days, equilibrium fuel is inserted into the core, which results in k-eff steadily increasing over the remainder of the life time. An equilibrium k-eff (of approximately 1.35) may have been achieved at 120 days; however, additional runs would be necessary to verify. The Griffin result for k-eff is shown in Figure 23. It shows the same trends and similar values over time predicted by *kugelpy*.

Figure 24 show the behavior of the peak pebble power during the running-in phase predicted by *kugelpy*. The maximum pebble follows the same trend as the sharp interface, where an equilibrium peak power of 0.38 kW/pebble is reached between 60 and 80 days. Once equilibrium fuel is added, there is a sharp peak in the maximum pebble power. This peak is due to the higher enrichment of the fuel combined with the startup fuel, where the higher enriched fuel will produce proportionally more power compared with the startup fuel. The maximum pebble power does not fully reach equilibrium; however, an equilibrium maximum pebble power between 0.4 and 0.5 kW per pebble would be expected given the trend. The maximum power predicted by Griffin is shown in Figure 25. The peak power is well matched between the two codes. The maximum power appears to decrease more rapidly in the Griffin result after the power spike. Comparing Figures 25 and 24 at 100 and 120 days, it can be seen that Griffin is predicting a lower maximum power.

Figures 26 and 27 show the flux profile in the core and the discharge burnup of the fuel, respectively. Figures 26a and 26b show the flux distribution at 89 days (i.e., three time steps after equilibrium fuel is added). The flux profile at 89 days with equilibrium fuel injection predicted by Griffin is shown in Figure 26c. The flux shows peaking at the top of the core where the equilibrium fuel is being added. The peaking in flux causes the maximum pebble peaking as well. Figure 27 shows the divergent behavior caused by adding equilibrium fuel during the running in. Without the addition of equilibrium fuel, the fuel burnup converges to approximately 2 MWd/kg. The additional fuel loading of the equilibrium fuel and the constant power result in the same amount of uranium being burned, which results in an overall lower burnup level.

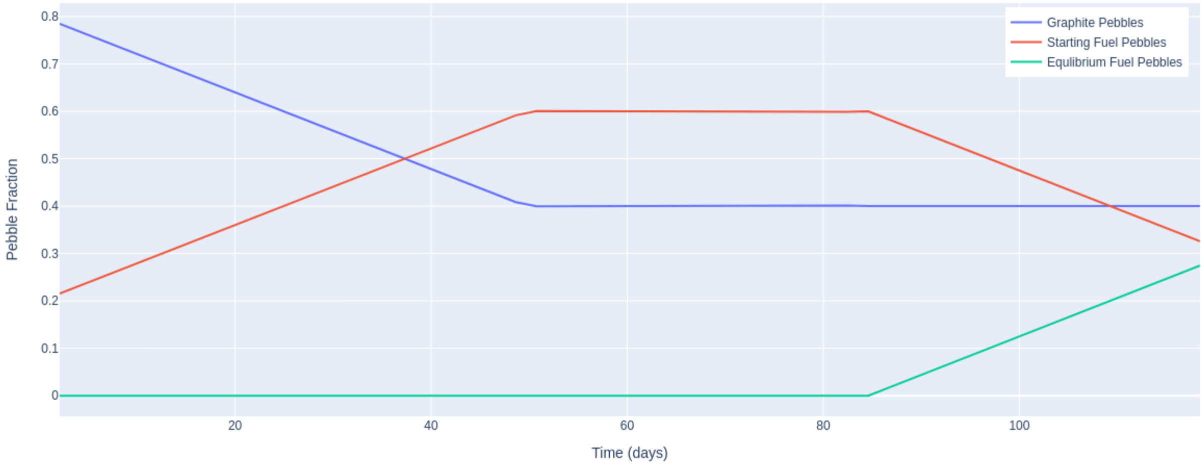

Figure 21. Fraction of starting fuel and graphite pebbles for the running-in process with the injection of equilibrium fuel at 82 days. This result is the same for both the Griffin and *kugelpy* model.

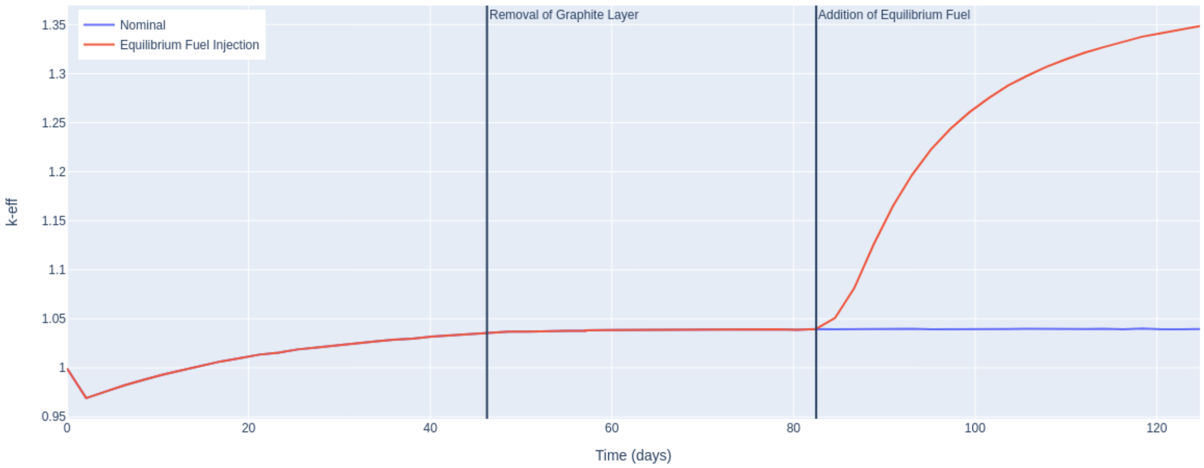

Figure 22. Critical eigenvalue for the the running-in process starting with the injection of equilibrium fuel at 82 days predicted by *kugelpy*.

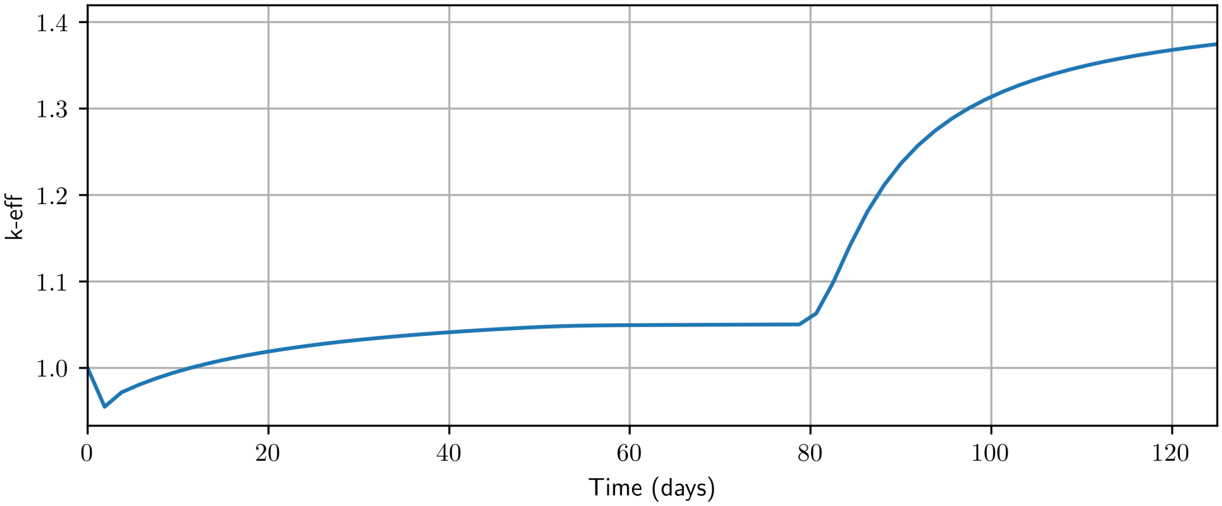

Figure 23. Fraction of starting fuel and graphite pebbles for the running-in process with the injection of equilibrium fuel at 82 days predicted by Griffin.

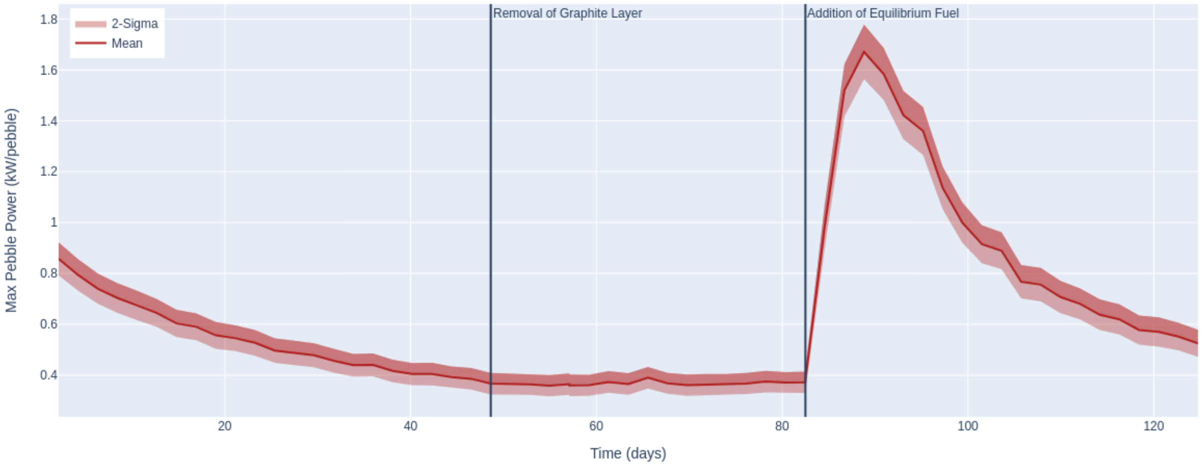

Figure 24. Maximum pebble power for the running-in process starting with the injection of equilibrium fuel at 82 days predicted by *kugelpy*.

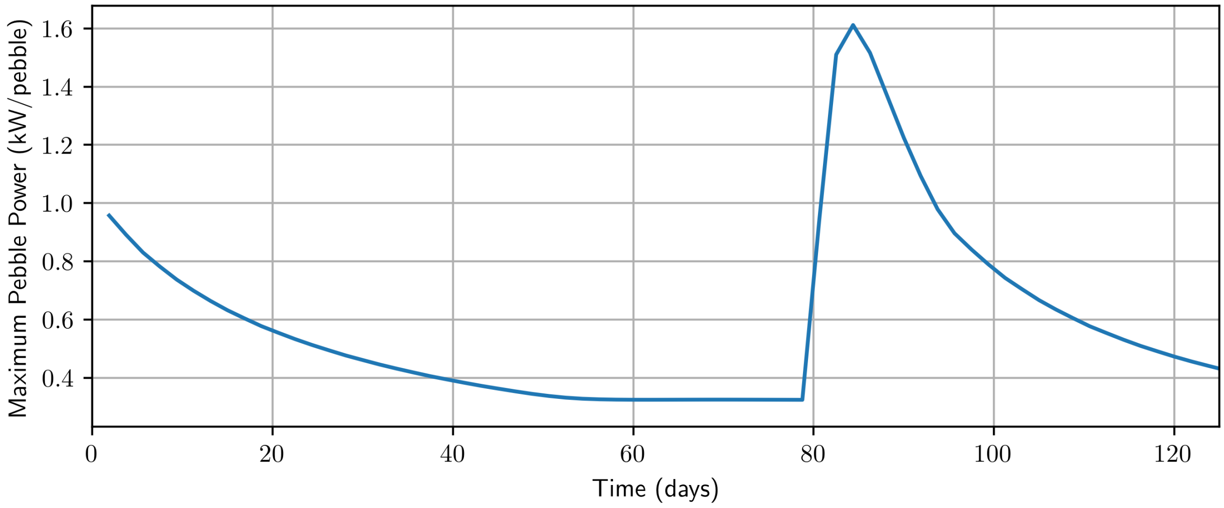

Figure 25. Fraction of starting fuel and graphite pebbles for the running-in process with the injection of equilibrium fuel at 82 days predicted by Griffin.

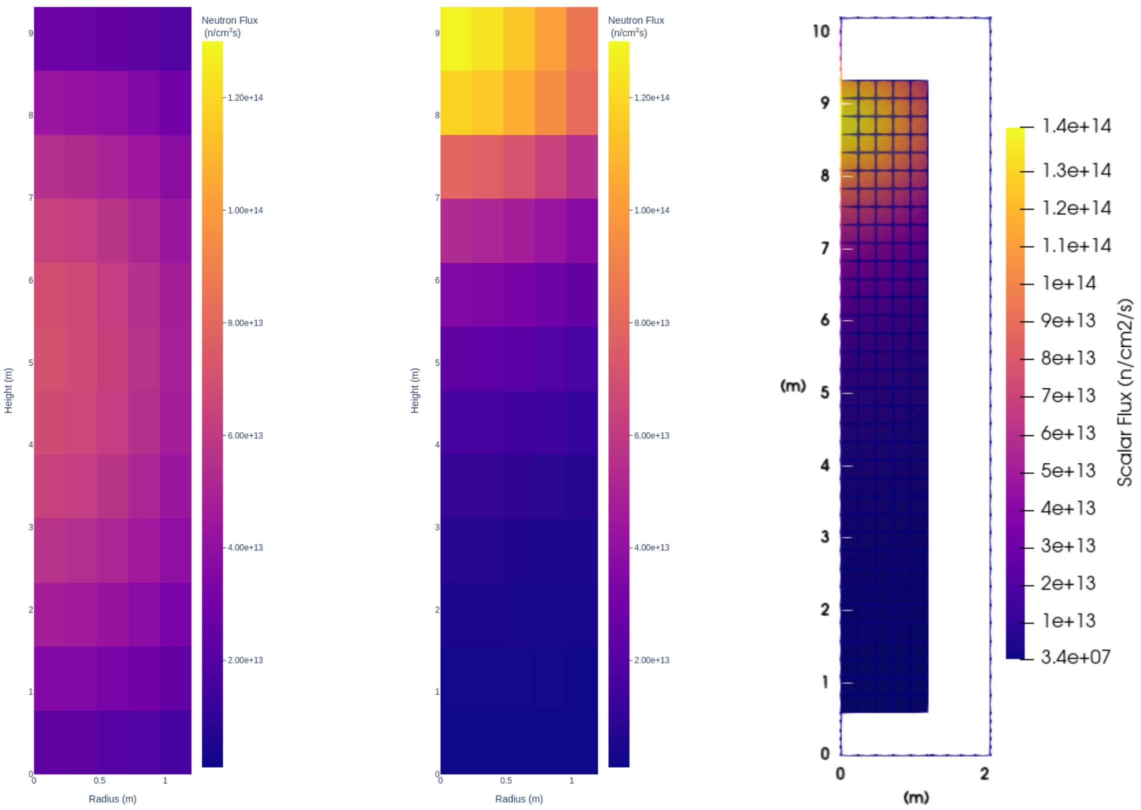

(a) Flux profile at 89 days without equilibrium fuel predicted by *kugelpy*

(b) Flux profile at 89 days with equilibrium fuel predicted by *kugelpy*

(c) Flux profile at 89 days with equilibrium fuel predicted by Griffin

Figure 26. Comparison of the flux profile for the addition of equilibrium fuel during the running-in process.

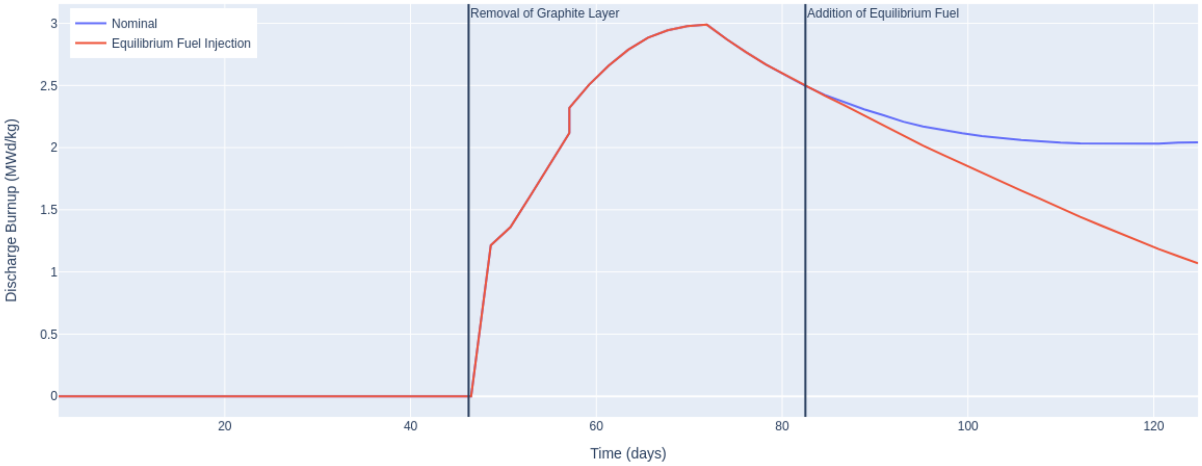

Figure 27. Discharge burnup for the running-in process with the injection of equilibrium fuel at 82 days predicted by *kugelpy*.

2.2.3. Injection of Equilibrium Fuel II

The second injection of equilibrium fuel running-in scenario was used to examine the inclusion of sharp interface between the fuel and graphite pebbles followed by another sharp interface with the equilibrium fuel. For this, the critical height of 550 cm was used for the initial critical height of the core. After this, the running-in scenario was performed using the parameters found in Table 3. The major difference is that at approximately 82 days, the startup fuel and graphite pebbles are replaced with equilibrium fuel. Figure 28 shows the transition from a critical core with nearly 80% graphite pebbles to the equilibrium fraction of 40%; at roughly 82 days both starting fuel and graphite pebbles are replaced with equilibrium fuel.

Figure 29 shows the k-eff predicted by *kugelpy* and Figure 30 shows the same result predicted by Griffin. Similar to Section 2.2.2, there is sharp increase in k-eff; however, this case sees a lower increase, which may be counter intuitive. There are more fuel pebbles, but the increased moderation from the mix of graphite pebbles in Section 2.2.2 actually leads to a higher eigenvalue.

Figure 31 show the behavior of the peak pebble power during the running-in phase predicted by *kugelpy* and the values predicted by Griffin in Figure 32. The maximum pebble follows the same trend as the Section 2.2.2 injection, where an equilibrium peak power of 0.38 kW/pebble is reached between 60 and 80 days. Once equilibrium fuel is added, there is a sharp peak in the maximum pebble power. Compared with the peak in Figure 24, the peak power is slightly lower due to a greater fraction of equilibrium fuel being added, which results in a more evenly distributed power. The maximum pebble power does not fully reach equilibrium; however, an equilibrium maximum pebbles power lower than Figure 24 as there is more equilibrium fuel in the core. The comparison between the Griffin and *kugelpy* results are similar to that from Section 2.2.2. Again, the maximum power during the power spike is predicted to be nearly the same between the two codes, but Griffin predicts that the maximum power decreases more rapidly after this point.

Figures 33 and 34 show the flux profile in the core and the discharge burnup of the fuel. Figures 33a and 33b show the flux distribution at 89 days (i.e., three time steps after equilibrium fuel is added). The flux shows peaking at the top of the core where the equilibrium fuel is being added. Similar to Section 2.2.2, the peaking in flux causes the maximum pebble peaking as well. Figure 34 shows the divergent behavior caused by adding equilibrium fuel during the running in. Without the addition of equilibrium fuel, the fuel burnup converges to approximately 2 MWd/kg. The additional fuel loading of the equilibrium fuel and the constant

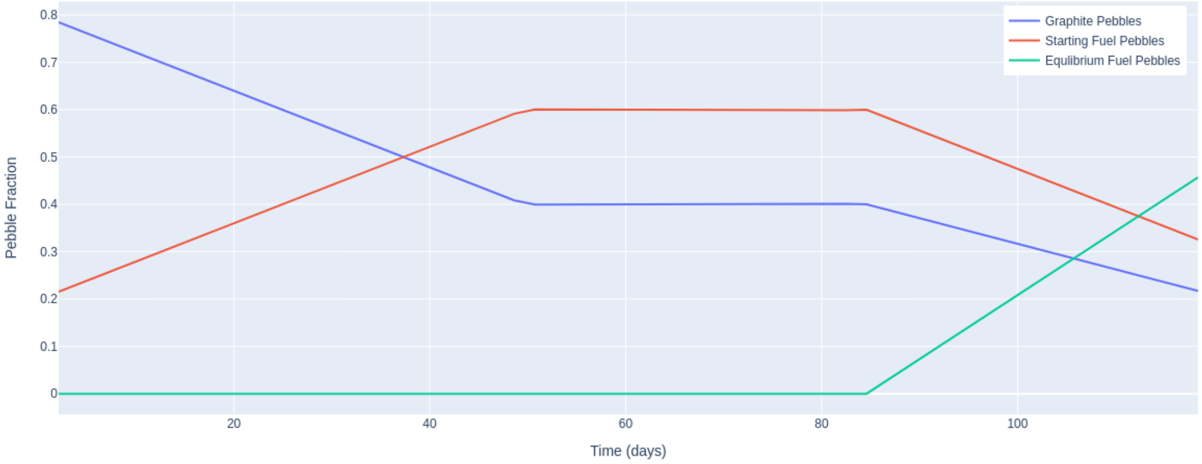

Figure 28. Fraction of starting fuel and graphite pebbles for the running-in process with the injection of equilibrium fuel at 82 days. This result is the same for both the Griffin and *kugelpy* model.

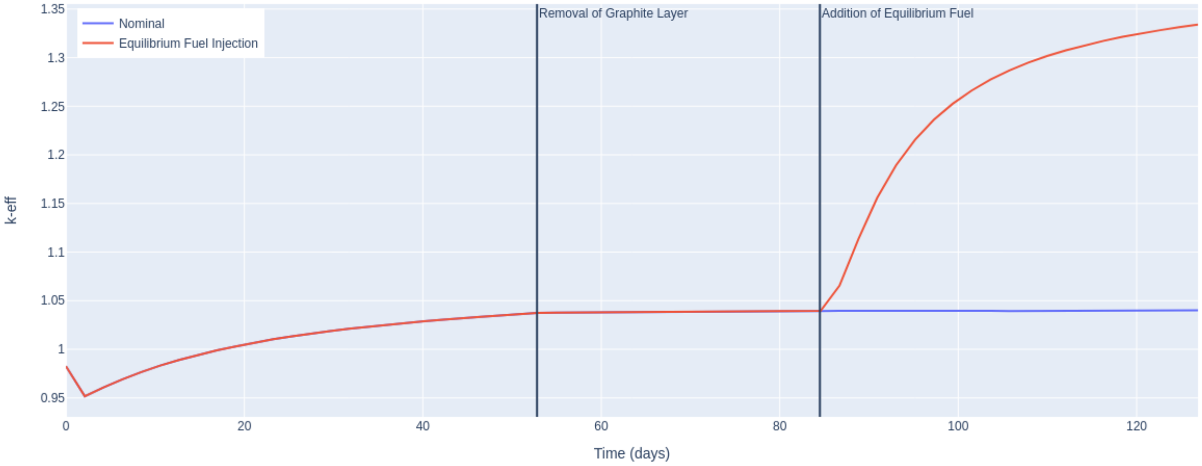

Figure 29. Critical eigenvalue for the running-in process starting with the injection of equilibrium fuel at 82 days predicted by *kugelpy*.

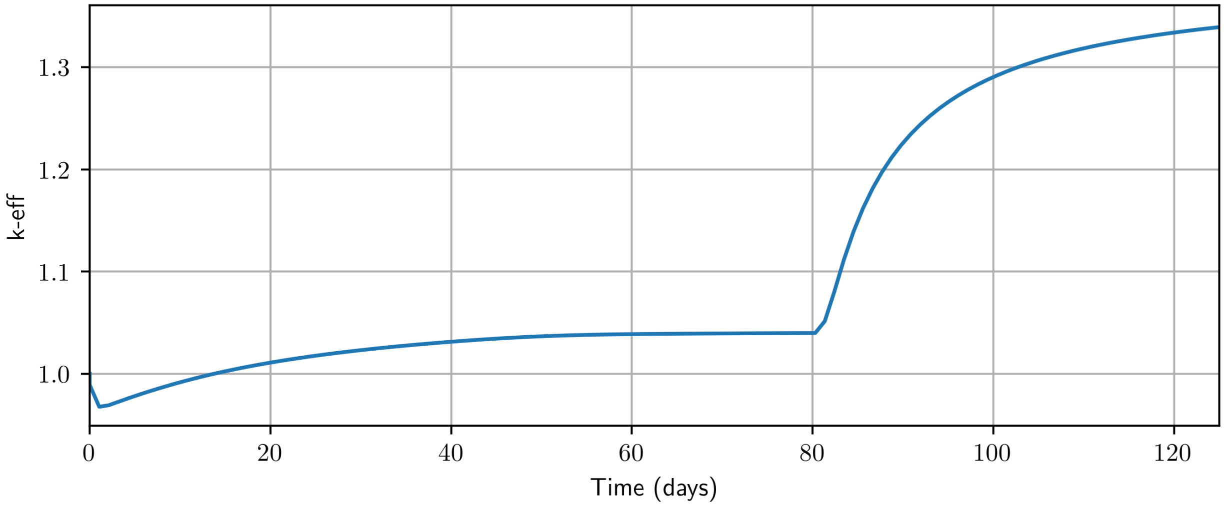

Figure 30. Fraction of starting fuel and graphite pebbles for the running-in process with the injection of equilibrium fuel at 82 days predicted by Griffin.

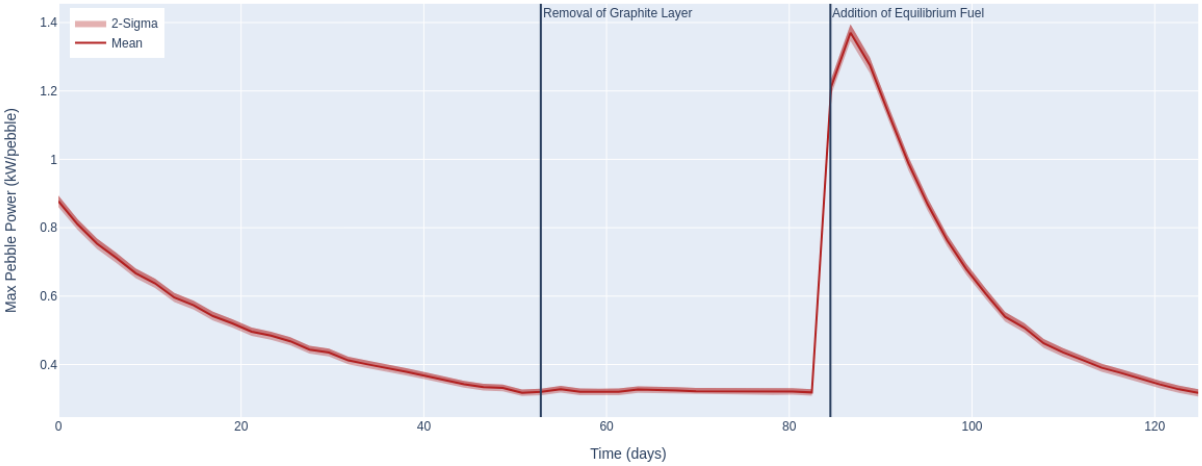

Figure 31. Maximum pebble power for the running-in process starting with the injection of equilibrium fuel at 82 days predicted by *kugelpy*.

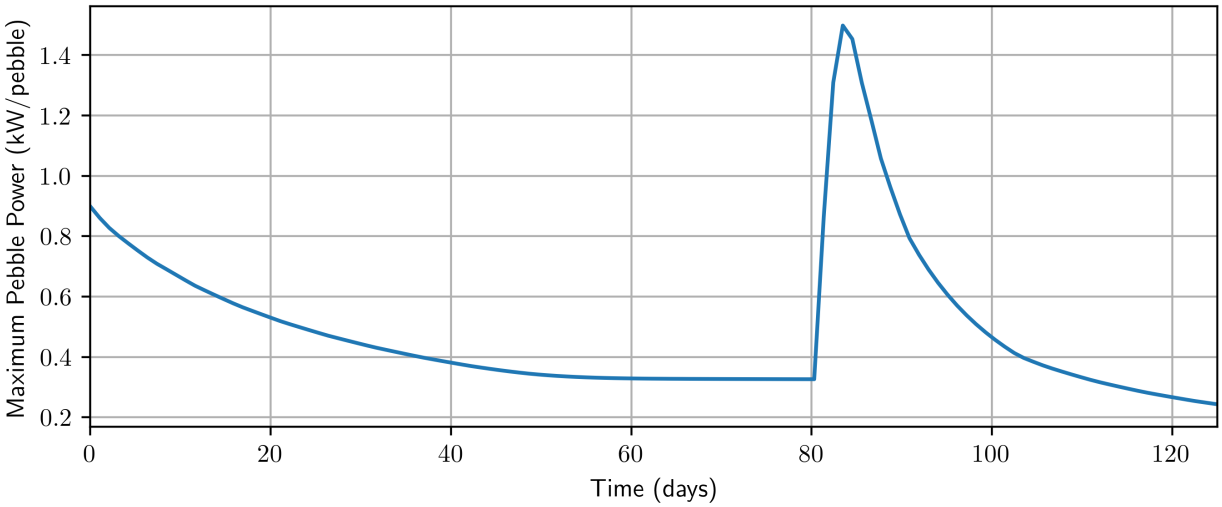

Figure 32. Fraction of starting fuel and graphite pebbles for the running-in process with the injection of equilibrium fuel at 82 days predicted by Griffin.

power results in the same amount of uranium being burned, which results in an overall lower burnup level.

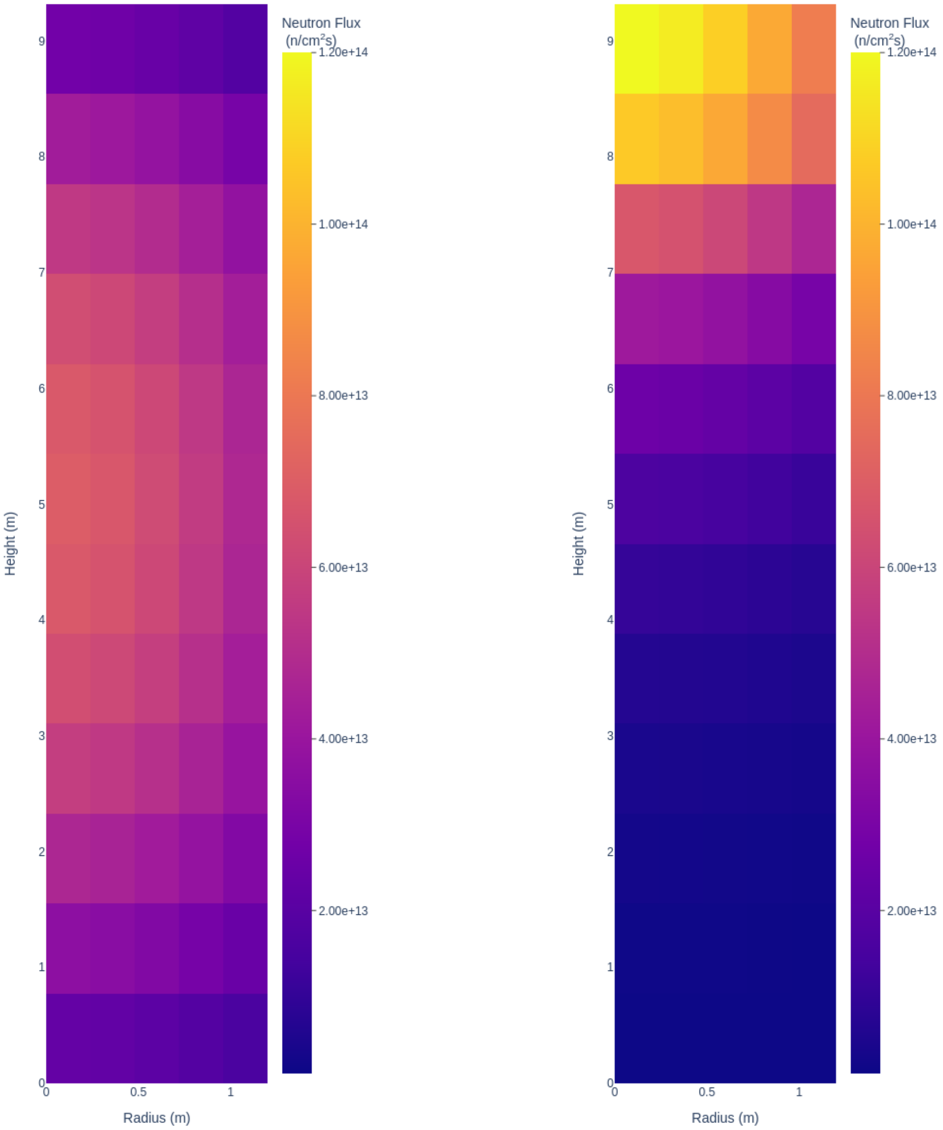

(a) (b)

Figure 33. Comparison of the flux profile for the addition of equilibrium fuel during the running-in process using Serpent.

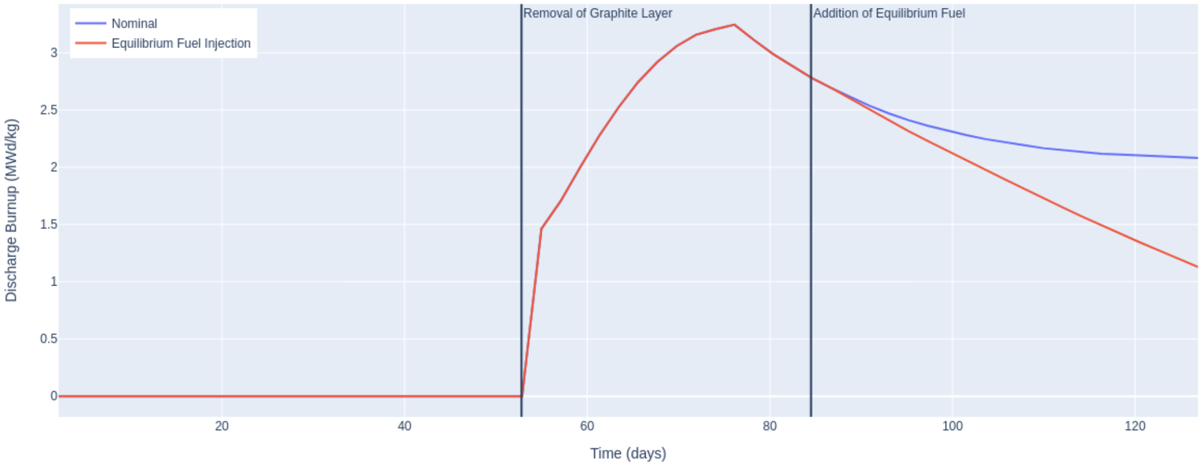

Figure 34. Discharge burnup for the running-in process with the injection of equilibrium fuel at 82 days using Serpent.

2.3. Code-to-Code Study Conclusions

This code-to-code comparison study started by showing good agreement for the predicted k-eff (within 300 pcm) for a fresh core of 40% graphite pebbles and 60% starting fuel pebbles. This was important because Griffin is using a multigroup library that was pregenerated targeting an equilibrium core configuration and it indicated that some meaningful validation could be carried out with these cross sections. Next, simple running-in simulations were conducted which showed good agreement for some important quantities such as the maximum values for maximum pebble powers over the running-in simulations. The predicted trends in k-eff were also similar. At times during the running in simulations, Griffin predicted lower maximum powers than *kugelpy*. The simple multigroup library used for Griffin in this work that was developed for an equilibrium core is expected to perform worse for burned fuel than fresh fuel. Some of the discrepancies between Griffin and *kugelpy* seen in this work are likely due to cross sections. The next step for validation work will be to use the new online cross section generation capability in Griffin. When online cross-section capabilities are implemented for running-in simulations, the models developed in this work will be valuable for re-evaluating the running-in capabilities in Griffin.

3. HTTF BENCHMARK

The High Temperature Test Facility (HTTF) [15] is an integral system test facility constructed and operated at Oregon State University using General Atomics' Modular High Temperature Gas-cooled Reactor (MHTGR) as its reference design. The main objective of this test facility is to experimentally investigate thermal fluid behaviors of interest to MHTGR transients. A variety of tests were performed in the HTTF, providing experimental data to reflect system-level responses, which are suitable for a code benchmark of system analysis codes, and experimental data suitable for higher resolution thermal fluid codes, such as Computational Fluid Dynamics (CFD) codes. As a result, the test data from HTTF is being used as the basis for the OECD-NEA Thermal Hydraulics Code Validation Benchmark for High-Temperature Gas-Cooled Reactors. This benchmark, described in Reference [16], provides problems representing hot gas mixing in the lower plenum (LP) and representing the Depressurized Conduction Cooldown (DCC) and Pressurized Conduction Cooldown (PCC) transients. Each problem in the benchmark includes exercises for code-to-code and code-to-data comparisons. The DCC and PCC problems also provide an exercise for error scaling between HTTF and MHTGR. An overview of the benchmark problems and their exercises are in Table 4.

Table 4. Summary of benchmark problems and exercises (“coupled” means system code coupled to CFD in the LP, ”PG” stands for Procedural Guide).

Problem No.	**Physics**	**HTTF Expt.**	**Code to Code (Exercise 1)**	**Code to Data (Exercise 2)**	**Error Scaling (Exercise 3)**	**Methods**
1	LP Mixing	PG – 28	Yes	Yes	No	CFD
2	DCC	PG – 29	Yes	Yes	Yes	System, coupled
3	PCC	PG – 27	Yes	Yes	Yes	System, coupled

3.1. System Analysis Code Benchmark

The code-to-code comparisons in Exercise 1 provide an opportunity for benchmark participants to compare their results to each other based on “fixed conditions” such as material properties and initial and boundary conditions. This comparison provides an opportunity to explore the impact of different model nodalizations and code capabilities in system modeling. This section presents results from Problem 3 based on analysis conducted at Argonne National Laboratory (ANL) using SAM, Idaho National Laboratory (INL) using RELAP5-3D, and Korean Atomic Energy Research Institute using GAMMA+.

3.1.1. The HTTF Facility Description

The HTTF is based on General Atomic’s MHTGR design, which uses prismatic graphite blocks in the core and reflectors. Compared to the MHTGR, the HTTF was scaled 1/4 in length and diameter and operated at prototypical temperature but at reduced pressure. Figure 35a shows the reactor pressure vessel (RPV) with flow path of helium coolant in normal operation. The RPV is surrounded by a reactor cavity cooling system (RCCS) constructed of water-cooled panels to establish boundary conditions for the tests and control radiation heat transfer from the RPV wall. The cavity between the RPV and RCCS panels is not air-tight, and it is expected that air flow through the cavity removes some amount of heat from the RPV.

The core is made up of 10 Greencast 94-F ceramic blocks, shown in Figure 35b, three lower reflector and two upper reflector blocks. In the radial direction, the core is divided into several regions: central (inner) reflector, inner, middle, and outer core, side (outer) reflector, and permanent reflector. In the axial direction, the blocks are stacked on one another (Figure 35c). There are 556 coolant channels cast in the ceramic blocks through which helium coolant flows to remove heat. The core is electrically heated by 210 graphite heater rods. The HTTF has 400 data acquisition channels for thermocouples, pressure transducers, and gas sensors.

3.1.2. Modeling the HTTF with System Codes

3.1.2.1 SAM The SAM model of the HTTF is based on the so-called two-dimensional (2D) ring model approach to approximate a 3D geometry (Figure 36). In this approach, the structures are homogenized and rearranged in concentric rings (annuli). In the core, a coolant or heater ring represents one hexagonal array of coolant channels or heater rods, and a ceramic ring represents the matrix material that provides the heat conduction path connecting coolant channels to heater rods. In converting to a ring, the cross-sectional area and the volume of the coolant channels are conserved by the ring thickness. The heat transfer surface

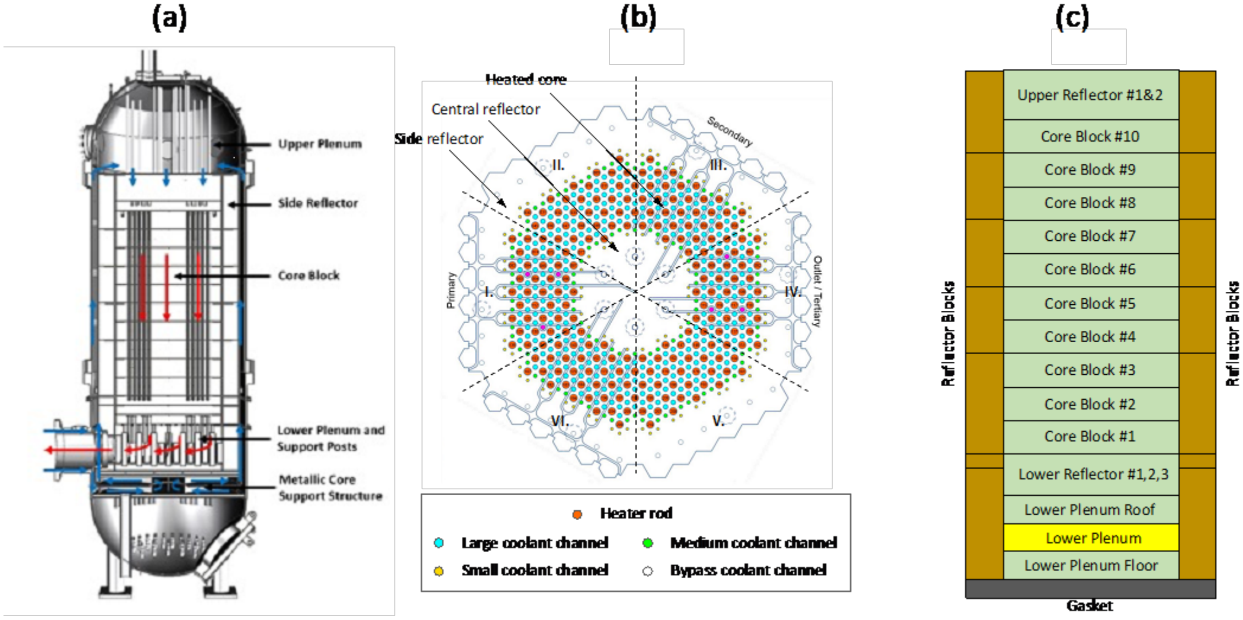

Figure 35. (a) Reactor pressure vessel with flow path, (b) core block, and (c) axial block stack.

area is properly accounted for applying an adjustment factor to the heat transfer surface area density for the ceramic rings. There are multiple rings in the core to capture the localized heat transfer, and ring-to-ring radial conduction captures core-wise heat conduction. In the 2D ring model, the heat transfer pathway follows the following sequence: heater ring → ceramic ring → coolant ring → ceramic ring → heater ring, etc. Outside of the core, the core barrel, upcomer, RPV, and RCCS are also modeled as concentric cylindrical rings. The HTTF core is modeled with 13 coolant rings, 11 heater rings, and 25 ceramic rings. One ring each is used to model the core barrel, upcomer, RPV, RCCS, and RCCS air cavity.

3.1.2.2 RELAP5-3D The RELAP5-3D model used in this work is based on the model published in Reference [17]. That model was reduced to a model of the vessel and RCCS only, and the thermophysical properties of the core blocks, permanent reflector, core vessel, and RCCS steel were modified to match the HTTF benchmark specifications. This model, shown in Figure 37, represents coolant flow through the six inner reflector coolant channels with Component 132. Components 140, 145, and 150 represent flow through the inner, middle, and outer portions of the core region respectively. Component 162 represents the coolant flow in the 36 outer reflector flow channels. Coolant gaps between the core block and permanent reflector and between the permanent reflector and core barrel are modeled with Components 164 and 166. In the inner and outer reflector regions that do not contain coolant channels, the block has been modeled using concentric cylinders representing the hex-block geometry of HTTF. In the regions of the reflectors that contain coolant channels and of the core, a unit cell approach was used as shown in Figure 37. Radial conduction within the core blocks is modeled using the conduction enclosure capability and heat transfer from the core to the permanent reflector, from the permanent reflector to the barrel, the barrel to the vessel, and the vessel to the RCCS are all accomplished through radiation enclosures.

3.1.2.3 GAMMA+ GAMMA+ has been upgraded for use as a system transient and safety analysis tool for non-light-water reactors in the Korea Atomic Energy Research Institute (KAERI). The GAMMA+ code has a lot of special features to simulate various thermofluid phenomena that occur during normal operating

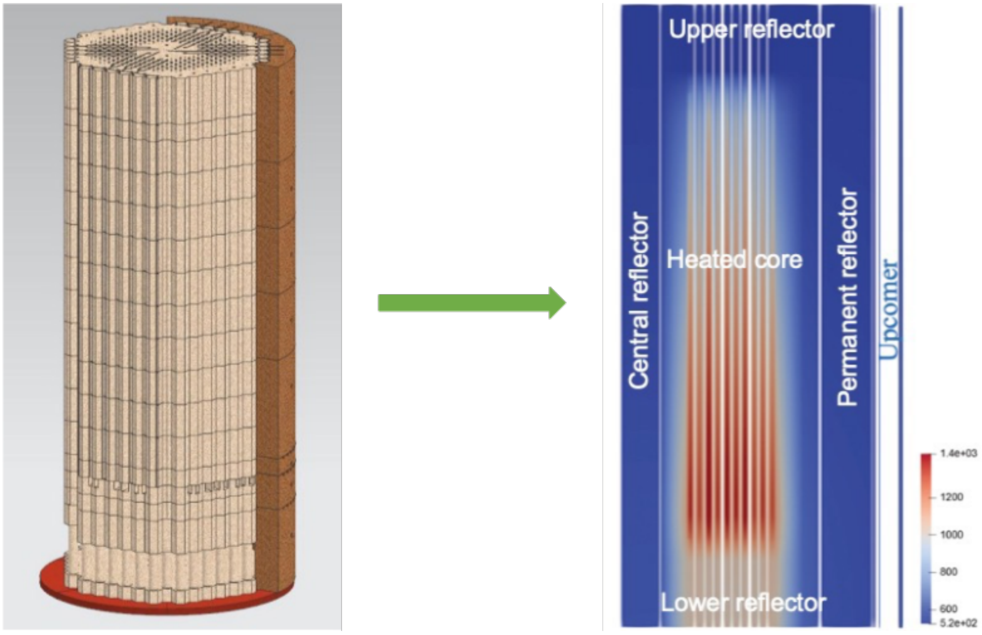

Figure 36. 2D ring model of the HTTF showing temperature distributions across the core and reflector regions.

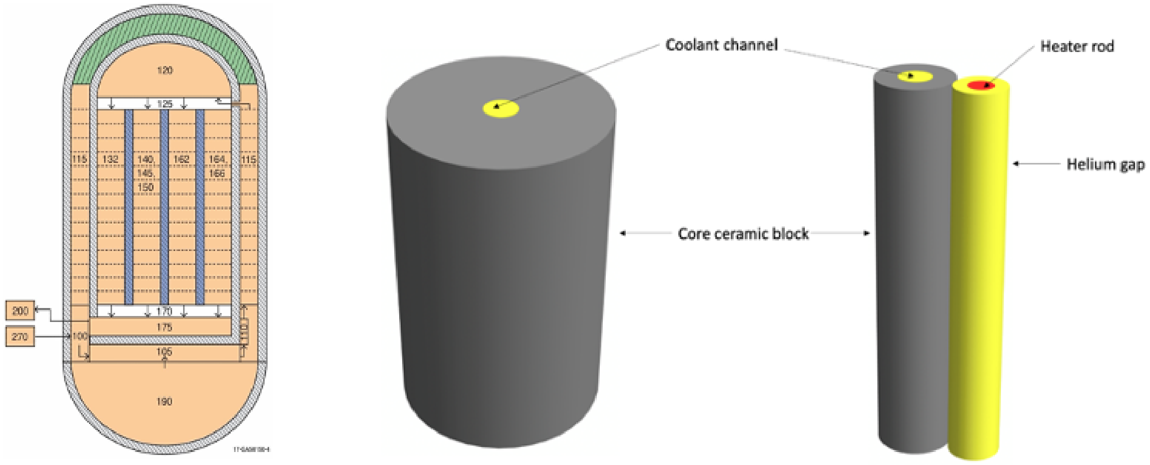

Figure 37. Nodalization diagram of the HTTF (left) and unit cells for the reflector (center) and core (right).

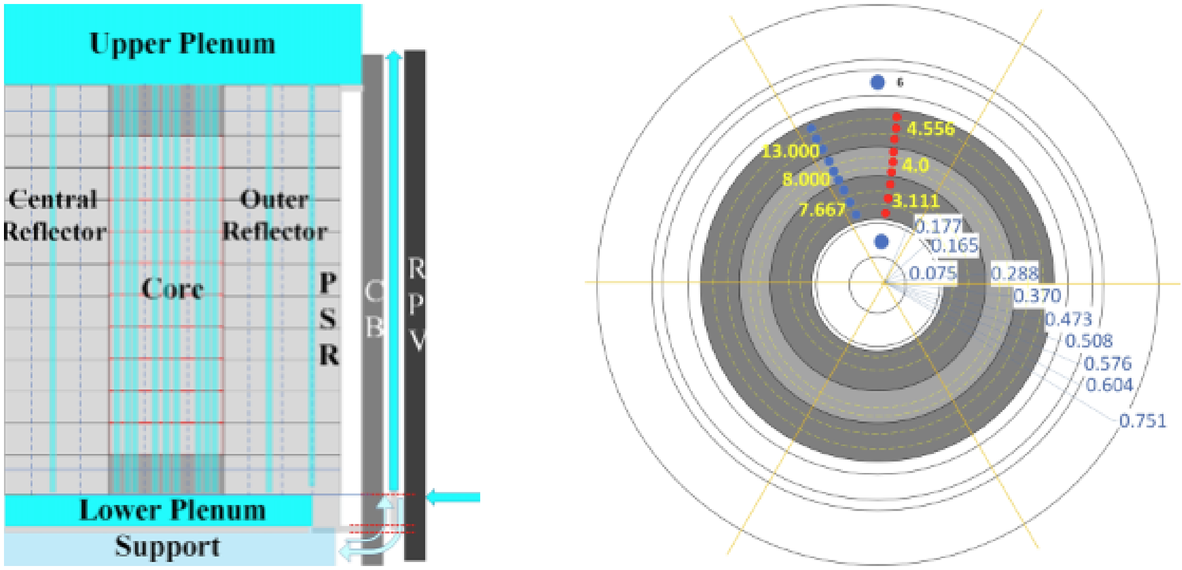

Figure 38. Schematic of the GAMMA+ model of the HTTF.

as well as postulated accident conditions in an HTGR. Figure 38 represents the GAMMA+ nodalization for HTTF system. The inner and outer reflectors have 14 nodes axially and three nodes radially. The fuel blocks that contain the heater rods consist of 10 axial blocks (nodes). The fuel block is divided into inner, middle, and outer rings radially. Each ring has three nodes. The arrangement of heater rods and coolant channels in the fuel block is simplified in GAMMA+ using the porous medium approach to approximate the HTTF core. Heater rods are modeled as 1D heat structures that transfer heat to the core blocks via thermal radiation and conduction. The core has nine radial cells and six circumferential cells. Users input the void fraction and equivalent flow and heat transfer areas of the coolant channels and heater rods in a 3D fuel block.

3.1.3. Code-to-Code Comparison Results

The simulations are performed according to the specifications proposed for the OECD/NEA International HTTF Benchmark. In the first part of the benchmark, the goal is for participants to compare results for exercises that have well-defined specifications. All simulations will use a common set of operating and boundary conditions, and thermophysical properties of materials. Although the HTTF has never been operated at full power, for this simulation it is assumed that all heater banks are operational producing maximum power output of 2.2 MW and that the axial heating profile is uniform. The operating conditions for steady state simulations are given in Table 5.

3.1.3.1 Steady State Table 6 tabulates the flow distribution in different core regions as calculated by SAM, RELAP5, and GAMMA+. The number of coolant channels in each region is also shown. The bypass flow in the inner and outer reflectors amounts to 12.3% of total flow, which is representative of bypass flow in the MHTGR. The agreement among the three system codes is excellent.

Figure 39 compares the helium and solid temperatures across the core and at different axial elevations. Overall, there is good agreement among the three codes; although, GAMMA+ predictions tend to be slightly higher than the SAM and RELAP5 predictions.The SAM model includes a large number of rings to represent the 516 coolant channels and 210 heater rods embedded within the core blocks. As a result, the radial

Table 5. Steady-state operating conditions.

Parameters	**Unit**	**Value**
Heating Power	MW	2.2
Helium Mass Flow Rate	kg/s	1.0
Helium Inlet Temperature	K	500
Helium Pressure	MPa	0.7
RCCS Water Mass Flow Rate	kg/s	1.0
RCCS Water Inlet Temperature	K	313.15
RCCS Water Pressure	MPa	0.1
RCCS Cavity Air Flow Rate	kg/s	0.025
RCCS Air Inlet Temperature	K	300

Table 6. Steady-state flow distribution (kg/s) in the HTTF.

Code	Inner Refl.	Inner Core	Middle Core	Outer Core	Outer Refl.
# Coolant Channels	6	138	144	234	36
SAM (ANL)	0.026	0.233	0.311	0.334	0.096
RELAP5 (INL)	0.026	0.231	0.306	0.335	0.101
GAMMA+ (KAERI)	0.025	0.233	0.314	0.333	0.096

temperature profile across the blocks is not smooth. The zigzag temperature pattern reflects the block geometry, with higher temperatures near the heater rods and lower temperatures adjacent to the coolant channels.

Table 7 compares the core barrel temperature at axial elevations corresponding to the elevations of the lower reflector, core blocks 1, 3, 5, 7, and 9, and upper reflector. There are notable small differences: GAMMA+ calculates a 27 K temperature increase from top (UR2) to bottom (LR3), compared to 18 K in SAM and 16 K in RELAP5, and the temperature at the top calculated by RELAP5 is $\tilde{1}$0 K higher than with SAM and GAMMA+.

Table 7. Temperature (K) along the height of the core barrel and reactor vessel.

Code	Structure	LR3	Bk1	Bk3	Bk5	Bk7	Bk9	UR2
SAM	Core barrel	518.4	517.4	514.4	511.0	507.6	504.0	499.9
RELAP5	Core barrel	535.7	532.0	530.0	524.2	520.0	515.4	509.9
GAMMA+	Core barrel	529.0	528.1	524.2	519.6	514.9	509.6	501.5
SAM	Reactor vessel	489.6	490.6	491.3	491.4	491.3	491.0	489.9
RELAP5	Reactor vessel	491.4	493.8	497.5	499.5	500.7	501.1	495.6
GAMMA+	Reactor vessel	489.1	489.4	489.8	489.9	489.8	489.7	485.6

There is better agreement in the vessel temperature also shown in Table 7. All three codes predict a practically uniform temperature on the reactor vessel and that the temperature peaks in the center (Bk5 in SAM and GAMMA+, Bk7 in RELAP5) and decreases very slightly toward the top or bottom where the structure is not facing the heated core.

3.1.3.2 Pressurized Conduction Cooldown Transient The PCC transient is initiated at time t = 0 in the simulations by tripping the gas circulator, which is assumed to coast down linearly in 1 second. The heating profile transitions to the ANS94 standard for decay heat [18]. The RCCS continues to operate

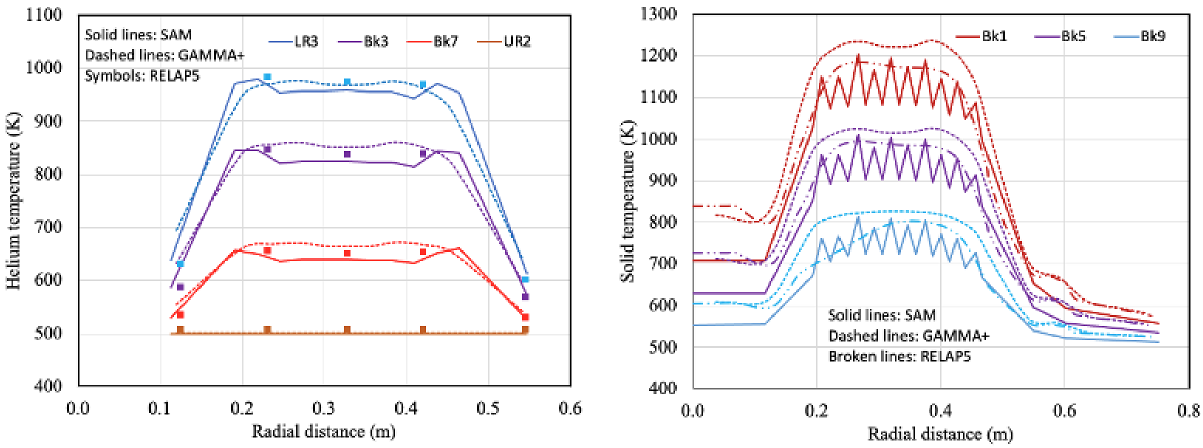

Figure 39. Steady-state core temperature for helium (left) and solid (right) at various axial elevations, including the lower reflector (LR), upper reflector (UR), and core blocks (BK).

normally. Decay heat is primarily transferred by the core-wise radial heat conduction and thermal radiation from the core region to the reactor vessel surface, and eventually to the RCCS via thermal radiation and convection.

After forced flow is terminated, natural circulation is established in the core due to the temperature difference between the core outer and inner regions. Figure 40 shows the flow rates calculated by different system codes in different core regions during the transient. Good agreement is observed among the codes, not only in the transient evolution but also in magnitude. Note that the flow rates immediately decline by three orders of magnitude from steady-state flow rate and this is captured by all three system codes. At the onset of the transient, the flow in the heated core reverses direction to flow upward while downward flow is maintained in the inner and outer reflectors where the temperatures are lower, effectively forming two natural circulation loops. Subsequently, the two loops converge to form a single loop with downward flow in the outer region (outer core and outer reflector) and upward flow in the inner region (inner reflector, inner core, and middle core). It is worth mentioning that the very small natural circulation flow rate in the HTTF core is not necessarily representative of the phenomenon in the MHTGR because the helium pressure in the HTTF is one-tenth the nominal operating pressure in MHTGR. Because the natural circulation flow is tiny in the HTTF, convective heat transfer is negligible. Consequently, the dominant mode of heat transfer in PCC in the HTTF is by thermal conduction and radiation.

The evolution from two flow loops to one can be explained by observing the radial temperature profile in the core block, shown in Figure 41. In normal operation and in the first few hours of the transient, the temperature is higher in the heated core than in the unheated reflectors, resulting in two circulation loops. During that time, the reflectors heat up while the core cools down because heat is conducted radially away from the core. The inner reflector then becomes the hottest part and temperature decreases radially outward. Consequently, the two circulation loops transition to a clockwise circulating loop. This phenomenon is well captured by SAM, RELAP5, and GAMMA+.

Figure 42 shows the temperature variation in the inner and outer core at three axial locations: Block 9 near the top, Block 5 in the middle, and Block 1 near the bottom. The complexity of the core geometry and differences in modeling approach result in different transient behavior predicted by the three codes. However, the common features observed are that the temperature in all blocks rises for the first few minutes because forced flow is cut off immediately while the decay heat drops to 5̃% of the nominal power level; following the initial increase, the temperature in the heated core starts to decline as heat is conducted to the colder regions

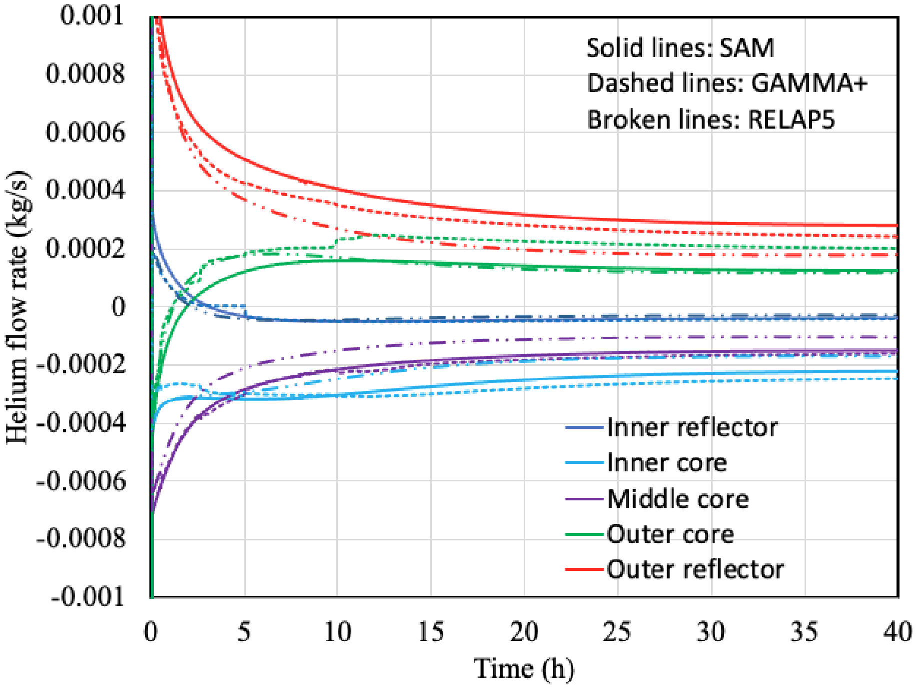

Figure 40. Natural circulation flow rates during PCC, positive flow is downward.

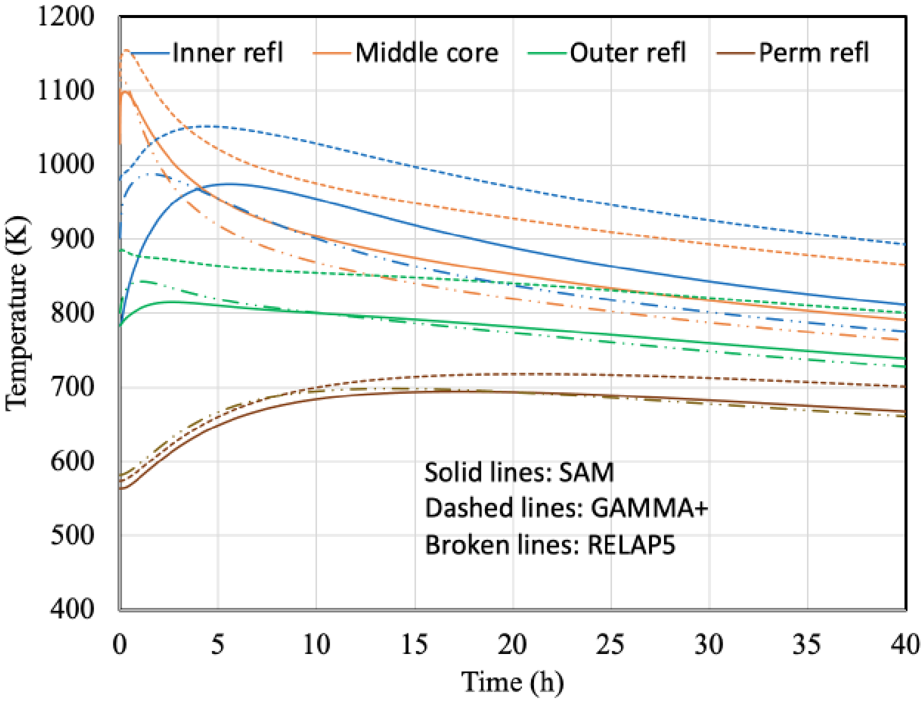

Figure 41. Temperature variation in the radial direction of the HTTF core block.

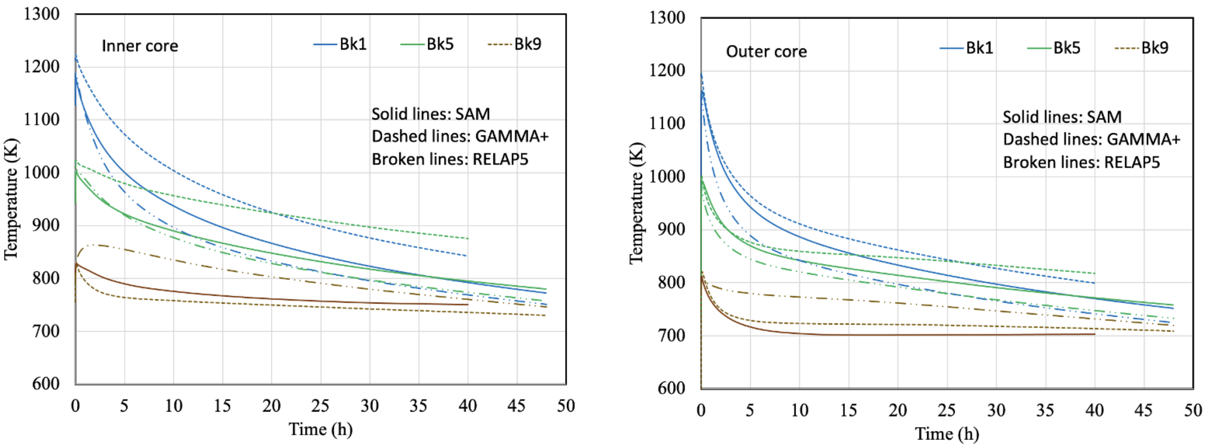

Figure 42. Temperature at three core blocks in the inner core (left) and outer core (right).

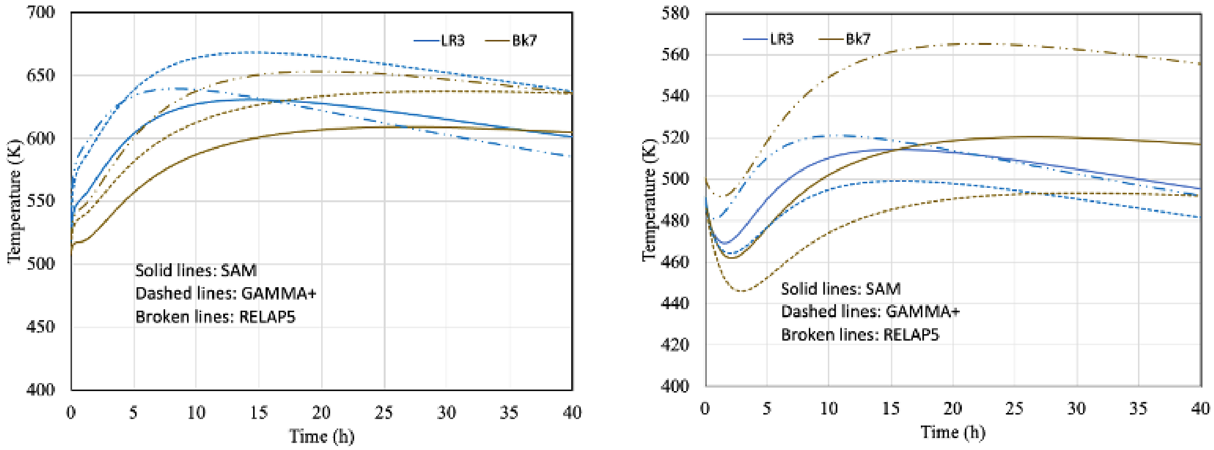

Figure 43. Core barrel (left) and vessel (right) temperatures at two axial elevations.

and transferred to the RCCS; and after many hours, the axial temperature profile transitions to one that peaks in the middle (Block 5) due to thermal conduction to the unheated upper reflector above the core and the lower reflector below the heated core.

Figure 43 compares the temperature variation in the core barrel and reactor vessel. Despite differences in the values, all three system codes predict that the temperature in the core barrel initially increases due to heat transferred from the heated core and subsequently decreases when the entire core is cooling down. During normal operation, the temperature of the vessel is approximately the same as the incoming helium temperature (500 K) flowing up the upcomer. In the first few hours of the transient, the vessel temperature drops because the helium flow has been terminated. Subsequently, the vessel temperature increases due to heat transfer from the core and eventually decreases again when the facility is cooling down.

Figure 44 shows the heat removal in the RCCS. The majority of heat loss is removed by the RCCS water panels, which receive energy from the reactor vessel primarily by thermal radiation. A smaller fraction of heat loss from the vessel wall is by the convection of air flow through the cavity (the space between the reactor vessel and RCCS panels). There is better agreement between SAM and GAMMA+ than with RELAP5. Noticeably, the relative amount of heat removed by the RCCS water panels is not consistent with the relative difference in the vessel temperature shown in Figure 43. For example, the vessel wall temperature predicted

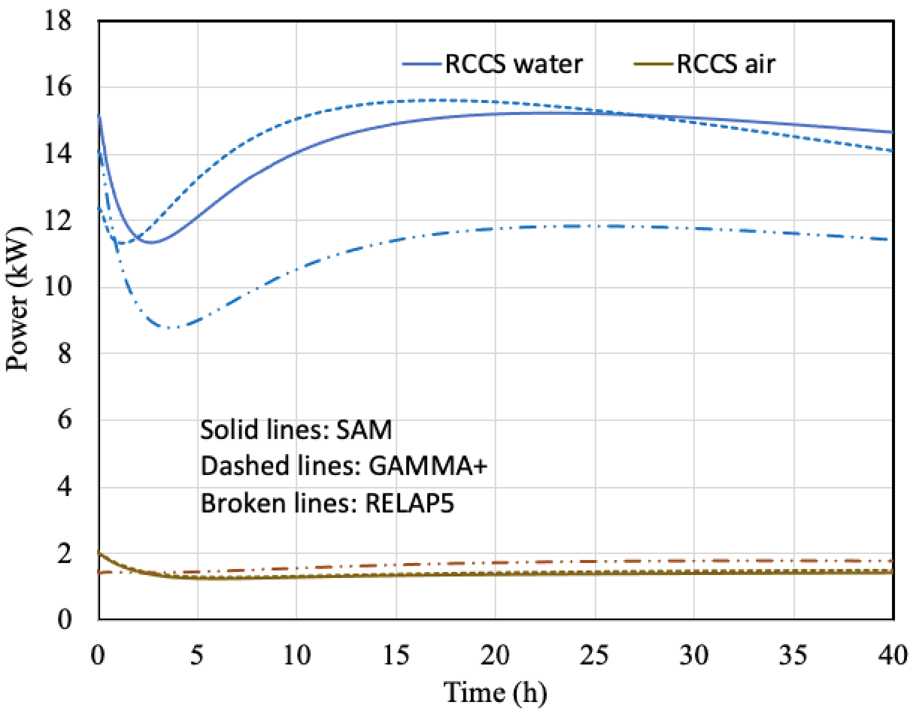

Figure 44. Heat removed in the RCCS water panels and through the air cavity.

by RELAP5 is highest among the three codes but the heat removal by the RCCS water panels is lowest. This discrepancy requires further investigation of the RCCS models in the three system codes, particularly with respect to the thermal radiation model.

3.1.4. Summary

Overall, the three codes can predict the HTTF under normal operation reasonably well. Good agreement was found for major parameters, such as coolant temperature, solid temperature, and flow distribution. In the PCC transient, the codes also agree with each other on the general transient characteristics, such as the natural circulation flow pattern and flow rate, which is three orders of magnitude smaller than steady-state forced flow, the rise and fall of the temperature in the solid structures in response to the loss of forced flow and subject to only decay heat, and the facility cooldown as a result of heat transfer to the RCCS. However, there are rather large discrepancies in the structure transient behavior that can be attributed to different modeling approaches, nodalizations, heat transfer closure models, and code capabilities. The discrepancies among the codes, and the limitations of each model, can be quantified in the next phase of the benchmark when code results are validated against the HTTF experimental data in Test PG-27. A desirable outcome of such validation is to improve the models to ensure the applicability of the system codes in HTGR prismatic design and transient conditions.

3.2. Lower Plenum CFD Benchmark

3.2.1. Problem Overview

Among the identified safety-relevant phenomena for the gas-cooled reactors, the outlet plenum flow distribution was ranked to be of high importance with a low knowledge level in the phenomenon identification and ranking table [19]. The heated coolant flows downward through the core region of the HTTF and enters the outlet and lower plenum through narrow channels, which causes the jetting of the gas flow. As the jets are restricted by different regions in the core, they have a nonuniform temperature and risk yielding high cycling thermal stresses in the lower plenum, negative pressure gradients opposing the flow ingress, and hot streaking. These phenomena cannot accurately be captured by 1D system codes; instead, the modeling requires using higher fidelity CFD codes that can offer an attractive avenue to predict the temperature fluctuations in the HTTF lower plenum [20]. As part of the efforts in an ongoing HTTF international benchmark campaign, the ANL team employs the CFD code, nekRS, to simulate the flow mixing problem in HTTF lower plenum with the two-equation $k-\tau$ turbulence model. The rest of this chapter is organized as follows: Section 3.2.2 will introduce the flow solver, nekRS, and the turbulence model employed; Section 3.2.3 details the simulation setups; and Section 3.2.4 focuses on the results and discussions.

3.2.2. Numerical Methods

NekRS is an open-source spectral element CFD code with capabilities for Reynolds-averaged Navier-Stokes (RANS) modeling, large eddy simulation (LES), and direct numerical simulation [21]. By using the Open Concurrent Compute Abstraction interface, NekRS supports both central processing unit (CPU) and graphics processing unit (GPU) backends. NekRS and its predecessor Nek5000 have been developed under U.S. Department of Energy Nuclear Energy Advanced Modeling and Simulation Program and have a long history of applications in reactor thermal hydraulics [22]. Spectral element method combines the accuracy of spectral methods with the domain flexibility of the finite element method. In nekRS calculations, the domain is discretized into E curvilinear hexahedral elements, in which the solution is represented as a tensor product of N^{th}-order Lagrange polynomials based on the Gauss-Lobatto-Legendre nodal points, leading to a total number of grid points $n = EN^3$. NekRS is highly parallel and has been previously applied to a wide range of problems to gain unprecedented insight into the physics of turbulence in complex flows. The time-stepping scheme of nekRS is semi-implicit; the diffusion terms of the Navier-Stocks equations are treated implicitly by using a k^{th}-order backward difference formula ($BDFk$), while nonlinear terms are approximated by a k^{th}-order extrapolation ($EXTk$) [23].

Most recently, an efficient two-equation $k-\tau$ RANS model has been implemented in nekRS to allow CFD simulations at engineering scale [24], particularly suitable for the HTTF lower plenum investigation considering the balance of computational cost and accuracy. The $k-\tau$ model, as a variant of the $k-\omega$ model [25], is selected here due to its robustness and flexibility in wall boundary condition specifications.

The incompressible formulation of nekRS is used in the current study, which assumes a Newtonian fluid with constant properties. The corresponding continuity, momentum, and energy equations are:

$$\nabla \cdot \mathbf{u} = \mathbf{0} \tag{1}$$

$$\rho(\frac{\partial \mathbf{u}}{\partial t} + \mathbf{u} \cdot \nabla \mathbf{u}) = -\nabla p + \nabla \cdot (\mu + \mu_\mathbf{t}) \nabla \mathbf{u} \tag{2}$$

$$\rho C_p(\frac{\partial T}{\partial t} + \mathbf{u} \cdot \nabla T) = \nabla \cdot (\lambda + \lambda_\mathbf{t}) \nabla T + q \tag{3}$$

where **u** is the velocity, p is the pressure, T is the temperature, ρ is the fluid density, μ and μ_t are the molecular and turbulent viscosities, C_p is the heat capacity, q is the heat generation rate, and λ and λ_t are the thermal conductivity and turbulent thermal conductivity. In the two-equation $k-\tau$ RANS model, the turbulent kinetic energy (k) and the inverse of turbulent dissipation rate ($\tau = 1/\omega$) are solved as two additional passive scalars. The corresponding transport equations are:

$$\frac{\partial(\rho k)}{\partial t} + \nabla \cdot (\rho k \mathbf{u}) = \nabla \cdot \left[(\mu + \frac{\mu_\mathbf{t}}{\sigma_\mathbf{k}}) \nabla k \right] + \mathrm{P} - \rho \beta^* \frac{k}{\tau} \tag{4}$$

$$\frac{\partial(\rho\tau)}{\partial t} + \nabla \cdot (\rho\tau\mathbf{u}) = \nabla \cdot \left[(\mu + \frac{\mu_{\mathbf{t}}}{\sigma_\tau})\nabla\tau\right] - \alpha\frac{\tau}{k}\mathrm{P} + \rho\beta - 2\frac{\mu}{\tau}(\nabla\tau \cdot \nabla\tau) \tag{5}$$

The term P represents the production of turbulent kinetic energy, while the closure coefficients used are consistent with the 2006 Wilcox $k - \omega$ model parameters [26], as follows:

$$\beta = 0.0708; \qquad \beta^* = 0.09; \qquad \alpha = 0.52; \qquad \sigma_k = \frac{5}{3}; \qquad \sigma_\tau = 2.0$$

The two turbulence scalars are then used to construct the eddy viscosity, which will be added to the molecular viscosity:

$$\mu_t = \rho k \tau \tag{6}$$

The turbulent Prandtl number Pr_t relates k_t and μ_t, which in the present work is selected as $Pr_t = 0.91$:

$$Pr_t \equiv \frac{\mu_t C_p}{k_t} \tag{7}$$

The $k - \tau$ RANS model has been demonstrated to produce results consistent with the established $k - \omega$ model [22, 24, 27].

3.2.3. CFD Simulation Setups

The HTTF lower plenum (i.e., core outlet plenum) geometry is illustrated in Figure 45, which contains 163 ceramic cylindrical posts on which the core structure stands. It is enclosed by lower side reflectors, lower plenum floor, and lower plenum roof. The height of the lower plenum is 22.2 cm. Helium gas enters the lower plenum through core coolant channels and exits through the horizontal hot duct. There are 234 inlet channels with the same diameter of 1 in (i.e., 2.54 cm). A cylindrical hot duct is connected to the lower plenum, which functions as the outlet channel. Rakes are installed in the hot duct to house measurement instruments in the experiments. Nek5000 requires a pure hexahedral mesh to perform the calculations. Due to the domain complexity, it is challenging to create an unstructured mesh with only hexahedral cells. A two-step approach is adopted in the meshing practice. We first used the commercial software, ANSYS Mesh, to generate an unstructured computational mesh consisting of tetrahedra cells (in the bulk) and wedge cells (in the boundary layer region, and then converted it into a pure hexahedra mesh using a native tet-to-hex Nek5000 utility [28]. To ensure the accuracy of wall-resolved RANS calculations, the first layer of grid points off the wall is kept at a distance of $y^+ < 1.0$. As shown in Figure 46, the resulting mesh has 2.60 million cells and the total degrees of freedom is approximately 72.86 million in Nek5000 simulations with a polynomial order of three. Note that the polynomial order is kept relatively low to limit the computational costs. It can be readily increased for higher fidelity simulations, such as a LES, given necessary computing hours.

The boundary conditions of the current CFD cases are taken from the corresponding system modeling of HTTF primary loop using RELAP5-3D. The reference lower plenum pressure is 211.9 kPa, and the helium gas has a density of 0.1950 kg/m3 with a reference temperature of 895.7 K. Table 8 summarizes the key thermophysical properties of helium flow used in the NekRS simulations. The 234 inlet channels are divided into 32 groups, as shown in Figure 47, based on the radial locations and polar angles, and each group with specific mass flow rate and temperature. Inlet channels within a certain group are assumed to have the same inflow velocity corresponding to the specific mass flow rate. Details of the inlet boundary conditions are listed in Table 9, where CG-XY denotes the channel group at Ring X and Angular Division Y. The configuration includes five rings (1–5) and six angular divisions (A–F), as depicted in Figure 47. Figure 48

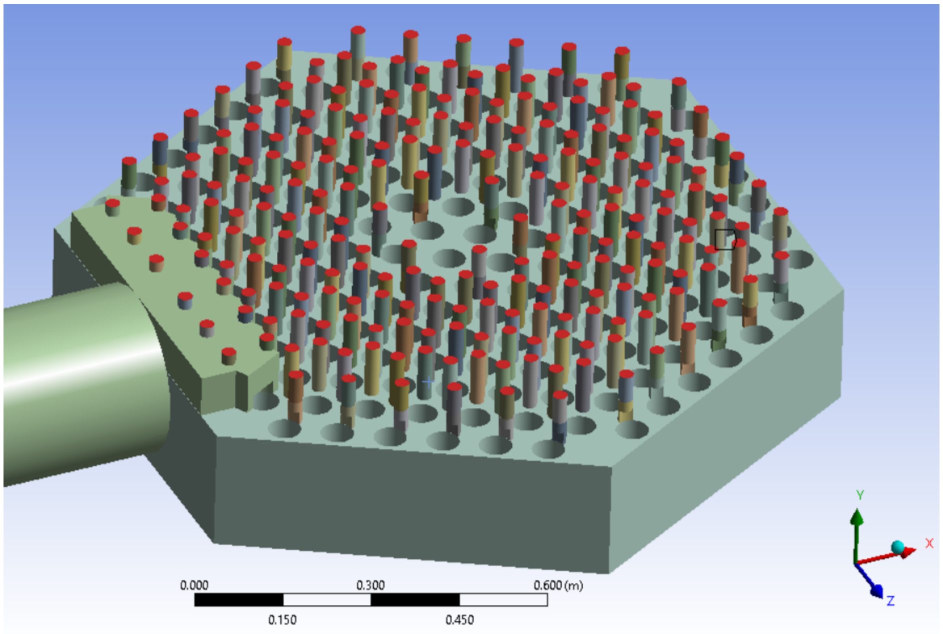

Figure 45. Overview of the HTTF lower plenum geometry (inlets highlighted in red).

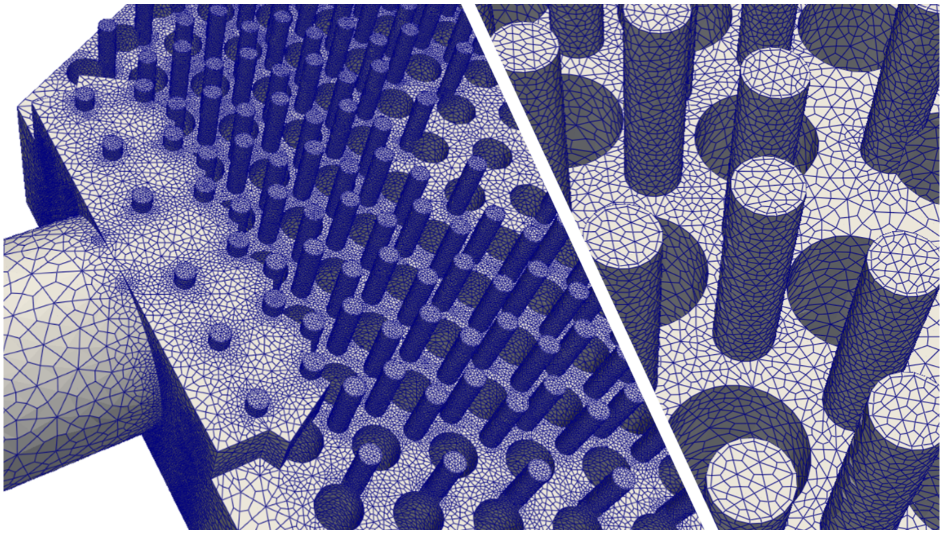

Figure 46. The hexahedral mesh of HTTF lower plenum from the tet-to-hex conversion.

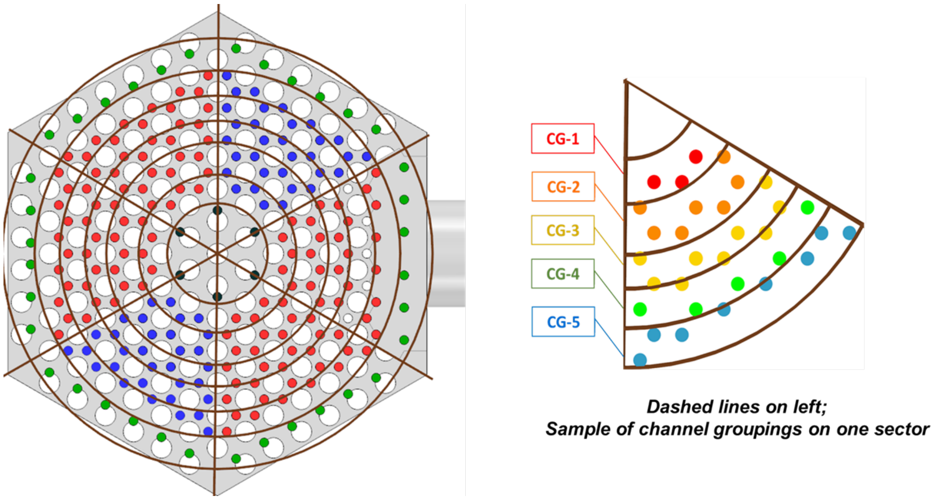

Dashed lines on left;
Sample of channel groupings on one sector

Figure 47. The grouping of lower plenum inlet channels.

visually illustrates the boundary conditions enumerated in Table 9. All wall surfaces are assumed to have no-slip velocity and adiabatic thermal boundary conditions, and a natural pressure condition is given to the outlet face of hot duct.

The CFD simulations were carried out in a dimensionless manner. The reference velocity is the mean flow velocity at hot duct, which is 35.73 m/s. Normalization of temperature is accomplished by referencing it to the maximum inlet temperature of 984.34 K at the CG0 group and the minimum inlet temperature of 810.05 K at the outer bypass group. Subsequently, during the postprocessing stage, it is straightforward to convert the CFD results back into dimensional values, enabling additional analyses to be conducted.

Table 8. Helium thermophysical properties and flow conditions.

Property	Value	Unit
Reference Pressure	0.8	bar
Reference Temperature	900	K
Helium Density	0.4	kg/m^3
Helium Heat Capacity	5.193×10^3	$J/(kg \cdot K)$
Helium Viscosity	4.307×10^{-5}	$Pa \cdot s$
Helium Thermal Conductivity	0.3027	$W/(m \cdot K)$
Helium Prandtl Number	0.74	–
Hot Duct Diameter	0.2984	m
Mean Flow Velocity at Hot Duct	35.73	m/s
Reynolds Number at Hot Duct	9.9039×10^4	–

The simulations were conducted using the GPU-optimized CFD solver NekRS, chosen for its significant computational efficiency, especially on GPU-based leadership-class supercomputers, like Polaris at ANL. A typical simulation job would use 50 compute nodes with four Nvidia A100 GPUs per node. A characteristics-based time-stepping has been used in the simulations to avoid the limitations imposed by the Courant-Friedrichs-Lewy number due to the explicit treatment of the nonlinear convection term. This treatment is necessary due to the existence of small local mesh cells created during the unstructured meshing and tet-to-hex conversion. A maximum Courant-Friedrichs-Lewy number of 3.0 has been reached, which corresponds to an average time step size of 2.5×10^{-5}.

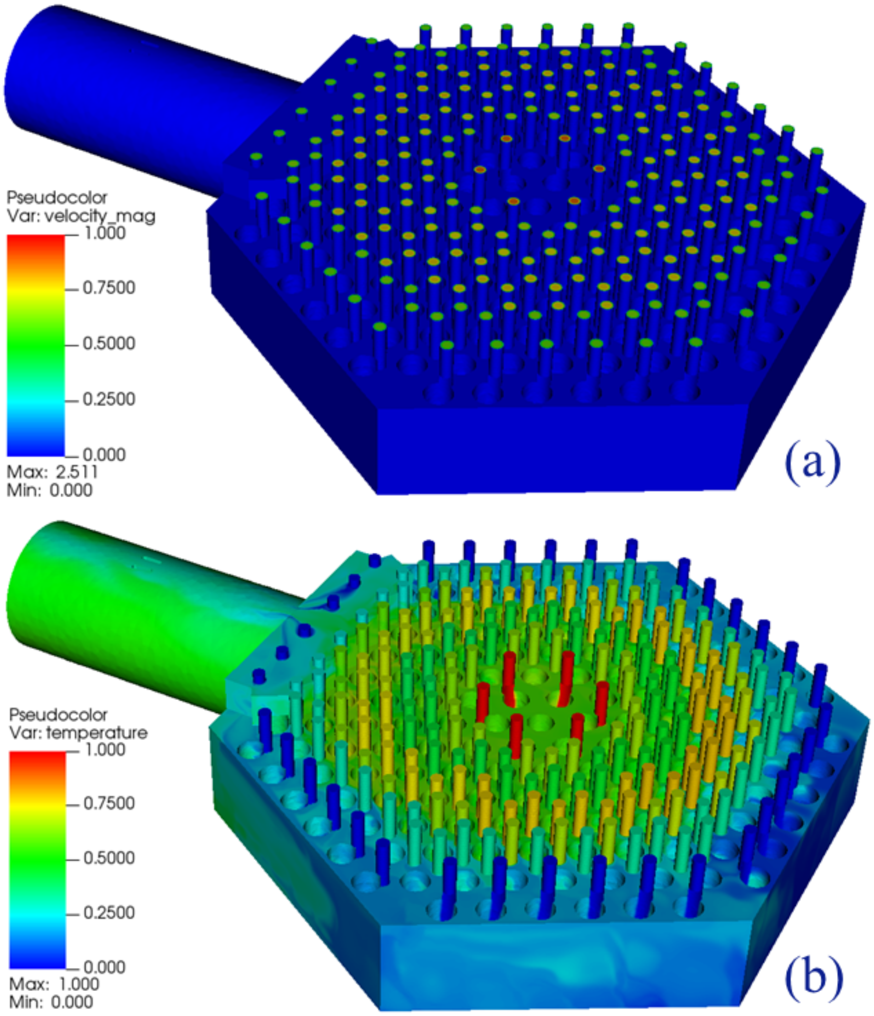

Figure 48. Boundary conditions: (a) prescribed inlet velocity and no-slip wall condition and (b) prescribed inlet temperature and adiabatic walls.

Table 9. Inlet boundary conditions for the HTTF lower plenum simulations.

Zone ID	Velocity (m/s)	Temperature (K)
CG-1A	30.389	984.34
CG-2A	23.513	924.658
CG-3A	25.709	889.08
CG-4A	26.618	944.901
CG-5A	26.405	926.654
CG-6A	21.83	866.424
CG-1B	23.513	925.415
CG-2B	25.69	890.425
CG-3B	26.61	947.609
CG-4B	26.446	932.229
CG-5B	21.828	867.567
CG-6B	23.511	924.788
CG-1C	25.702	889.276
CG-2C	26.608	945.155
CG-3C	26.394	926.902
CG-4C	21.825	866.606
CG-5C	23.52	922.995
CG-6C	25.794	886.395
CG-1D	26.772	941.098
CG-2D	26.586	922.794
CG-3D	21.91	863.558
CG-4D	23.517	920.054
CG-5D	25.9	881.331
CG-6D	27.101	932.826
CG-1E	27.129	913.384
CG-2E	22.303	856.71
CG-3E	23.521	922.956
CG-4E	25.796	886.341
CG-5E	26.775	941.027
CG-6E	26.589	922.725
CG-1F	21.911	863.508
CG-2F	23.521	922.956
CG-3F	25.796	886.341
CG-4F	26.775	941.027
CG-5F	26.589	922.725
CG-6F	21.911	863.508
Outer Bypass	20.669	810.051

3.2.4. Results and Discussion

A simulation time of 20 convective time units (CTUs) is first achieved to allow the turbulent flow to develop fully. One convective time unit is defined as the time it takes for the mean flow to travel one hydraulic diameter in the hot duct. Due to the nature of the unsteady RANS turbulence model, only a quasisteady state can be reached. Velocity fluctuations are observed as helium flow enters the lower plenum and passes through the LP posts. Snapshots of the instantaneous velocity and temperature fields at the lower plenum mid-plane (y

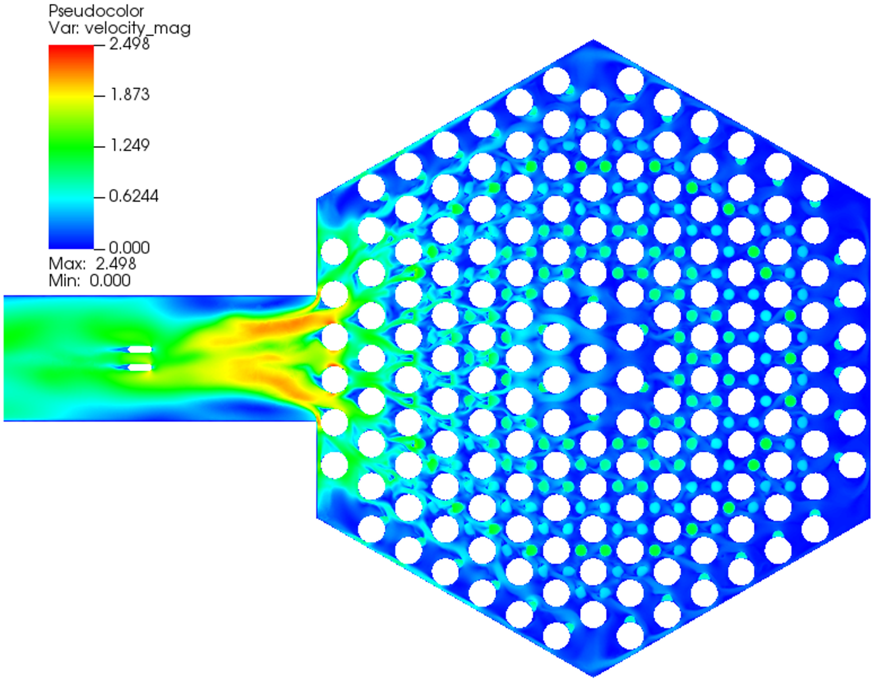

Figure 49. Snapshot of instantaneous nondimensional velocity distribution on the lower plenum mid-plane (y = -0.1, top view).

= -0.1) from the quasisteady state are shown in Figure 49 and Figure 50, respectively. Noticeable variations are detected in both velocity and temperature fields. The velocity magnitude gradually increases as the helium flow approaches the hot duct. Flow separation becomes evident around the lower plenum posts, particularly in areas near the hot duct, contributing to the observed instability in the fluid solutions.

The temperature distribution depicted in Figure 50 clearly shows the high-temperature jets interact with the lower plenum posts and floor, imposing thermal stress on the lower plenum structures. As evidenced by Figures 49 and 50, the presence of helium jets is quite conspicuous within the lower plenum, characterized by notably higher velocity and temperature values. Moreover, the inflow jets exhibit greater prominence in regions farther from the hot duct, owing to the diminished local horizontal flow. Conversely, areas nearer to the hot duct showcase more pronounced disturbances in the inflow jets due to the stronger local horizontal flow. Consequently, in Figure 50, the jets positioned away from the hot duct achieve deeper penetration, while those in close proximity to the hot duct experience quicker diffusion. The presence of hot streaking is further confirmed within the lower plenum, particularly in areas distant from the hot duct. The streams of elevated temperature directly impact the lower plenum posts and floor in this specific region, resulting in uneven thermal stresses. In general, the lower section of the lower plenum encounters higher temperatures, notably at the juncture between the lower plenum and the hot duct, as visually depicted in Figure 50.

Apart from the instantaneous solutions, an analysis involving time-averaging was conducted on the simulation results over an additional 10 CTUs. As an example, the time-averaged velocity field is displayed in Figure 51. By eliminating unsteady effects in the flow field, the time-averaged results reveal notably symmetric patterns in the velocity field along the centerline of the hot duct.

To better quantitatively assess the velocity and temperature distributions in the lower plenum, time-averaged velocity and temperature values along the lower plenum and hot duct centerlines were extracted, as shown in Figure 52. To ensure that the CFD results are mesh-independent, two additional cases with lower and higher mesh resolutions were set up. The coarse and fine mesh cases have 22 million and 171 million

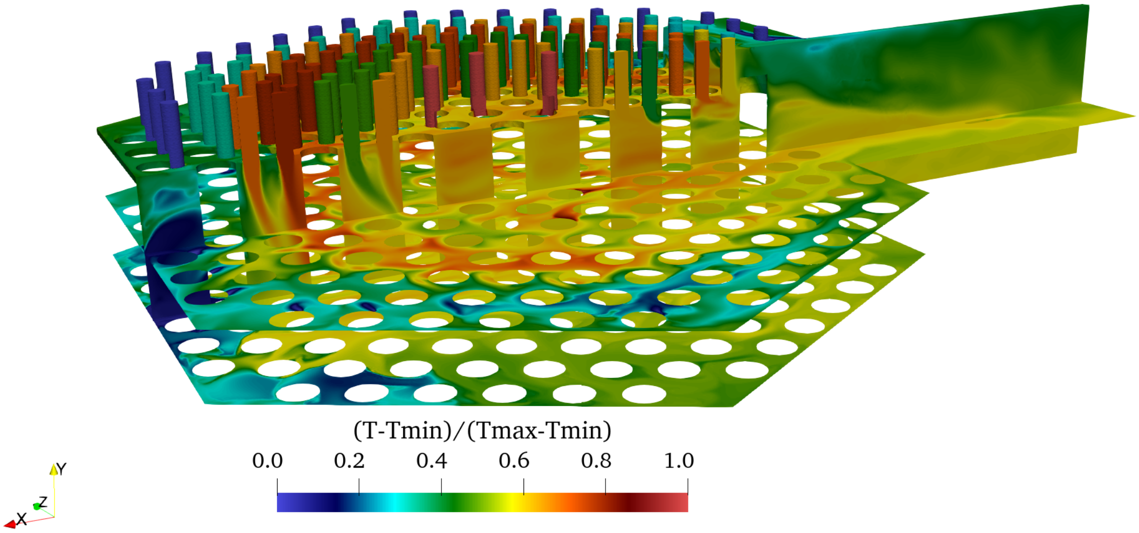

Figure 50. Snapshot of instantaneous nondimensional temperature distribution on the lower plenum mid-plane (y = -0.1, top view).

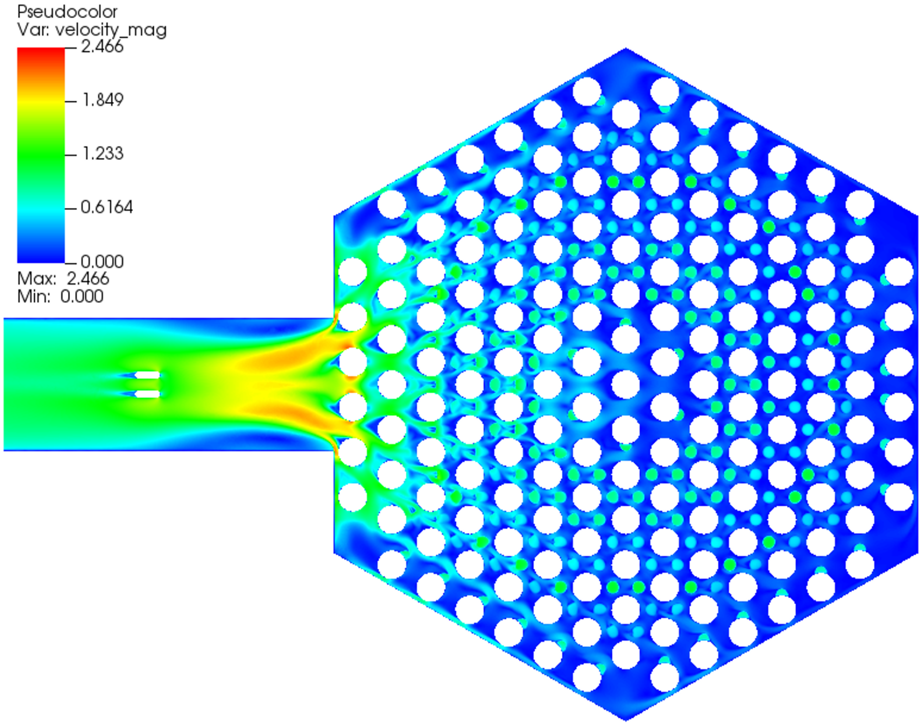

Figure 51. Time-averaged nondimensional velocity distribution on the lower plenum mid-plane (y = -0.1, top view).

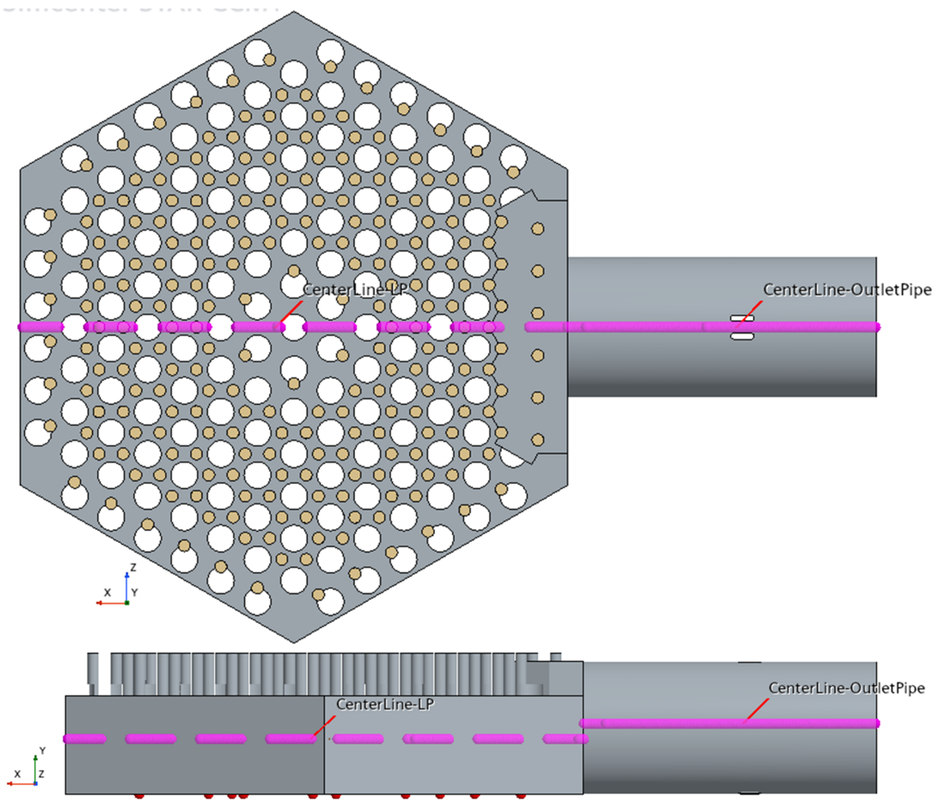

Figure 52. Centerlines through lower plenum and hot duct for data collection.

degrees of freedom, respectively, with polynomial orders of two and four. As a reference, our base case contains a total of 72 million degrees of freedom, as mentioned in the previous section. The same simulation workflow was adopted for the mesh study cases, including 20 CTUs for flow development and an additional 10 CTUs for time-averaging data collection and analysis. The corresponding profiles of time-averaged velocity and temperature along the lower plenum and hot duct centerlines are depicted in Figures 53 and 54, respectively. Overall, a very good mesh convergence trend is observed, particularly between the base case and the fine mesh case, confirming that the mesh used in our base case is adequate for capturing the primary flow features. In Figure 53, we observe a gradual increase in velocity magnitude as the flow approaches the hot duct, followed by a rapid acceleration at the junction between the lower plenum and the hot duct. The velocity magnitude tends to decrease as the flow nears the hot duct exit, but a peak is observed when the flow encounters the rakes installed in the hot duct. Additionally, the velocity profiles exhibit significant fluctuations downstream of $\frac{x}{D_h} \approx -2$, indicating flow separation and the presence of recirculation zones. As for the temperature profiles, the temperature remains relatively uniform in the bulk region of the lower plenum, with noticeable fluctuations in the peripheral region on the opposite side of the hot duct. The temperature evolution downstream of $\frac{x}{D_h} \approx -2$ may indicate a thermal stratification within the hot duct.

3.2.5. Summary

As part of the HTTF benchmarking efforts, we applied the spectral element CFD code, nekRS, to simulate the flow mixing phenomenon in the HTTF lower plenum. It has been successfully demonstrated that nekRS is capable of capturing the relevant flow physics within a complex geometry, such as the lower plenum. A mesh-independent study further confirmed the adequacy of our computational grid in capturing the primary

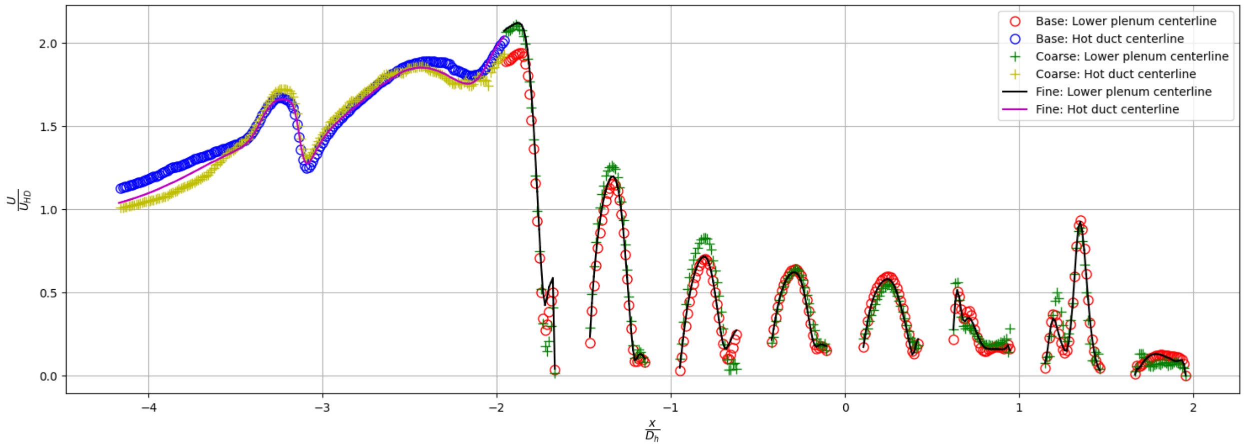

Figure 53. Time-average velocity magnitude along lower plenum and hot duct centerlines.

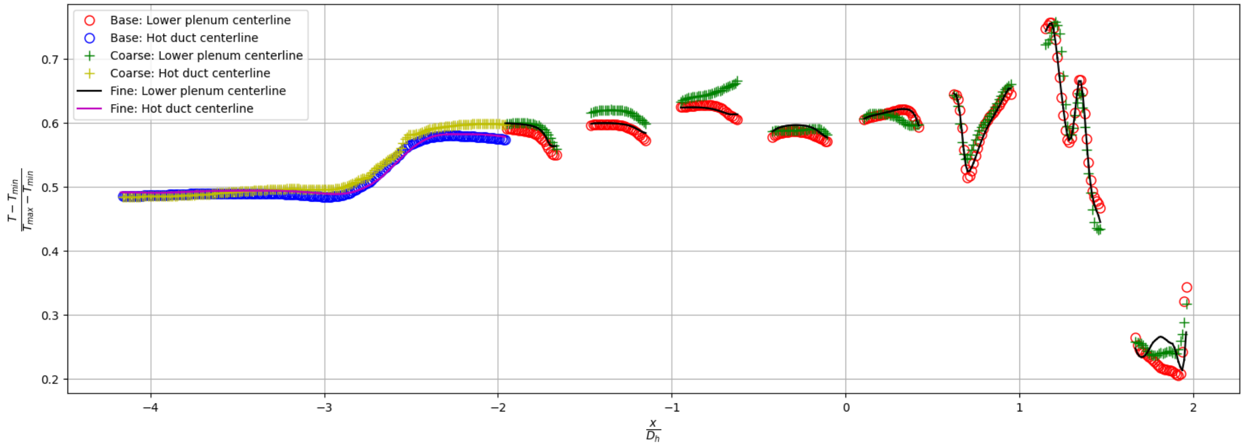

Figure 54. Time-average temperature along lower plenum and hot duct centerlines.

flow features. The current study examined the velocity and temperature distributions in the lower plenum and hot duct. It was observed that the temperature field remains relatively uniform throughout the bulk region of the lower plenum. However, due to the complex geometry, the flow solutions exhibit significant unsteadiness. Consequently, a time-averaging analysis was also conducted on the unsteady RANS results. As a work in progress, we are continuing with the postprocessing and analysis of the CFD results in preparation for the planned code-to-code and code-to-data comparisons within the HTTF benchmark teams.

4. GPBR200 SYSTEM ANALYSIS CODE BENCHMARK

4.1. Motivation

Compared with the conventional light-water reactors, the PBRs have complex core geometries that result in more complex thermal-fluid behaviors in the reactor core during both steady-state normal operating condition and transient scenarios. Furthermore, the reactor reliance on Reactor Cavity-Cooling System (RCCS) for decay heat removal during certain transients introduces further challenges that need to be resolved in the modeling of these reactors. In the conventional light-water reactors, heat is removed primarily through convective heat transfer between the fuel rods and the coolant during both steady-state operating condition and transient scenarios. The only differences are the source of the coolant (e.g., driven by coolant pumps compared with injection by emergency core cooling systems) and the switch from single-phase convective heat transfer to two-phase boiling heat transfer. On the other hand, for PBRs and other HTGR designs in general, the heat removal mechanisms during steady-state operating condition and transient scenarios could be substantially different.

Under steady-state operating conditions, similar to light-water reactors, heat is removed mainly by forced convection between fuel pebbles and the coolant, with the coolant being some type of gas rather than water. However, during loss-of-forced-flow transient scenarios, unlike light-water reactors, decay heat is primarily removed from the core via radial heat conduction from the pebble fuels to the side reflectors and finally to the RCCS. In the former, heat transfer is a localized phenomenon with a relatively small length scale on the order of several centimeters. Conversely, during loss-of-forced-flow transient scenarios, the core-wise radial conduction from the pebble bed to the RCCS adds another heat transfer length scale that corresponds to the reactor core diameter on the order of several meters. Furthermore, natural convection can establish in the core during the loss-of-forced-flow transients, which can further impact the temperature redistribution inside the reactor core and thus the removal of decay heat. The combination of different heat removal mechanisms poses a unique set of challenges to the modeling of the PBRs.

Various modeling approaches for PBRs have been demonstrated by researchers, ranging from the unit-cell approach by van Antwerpen et al. to study local heat transfer phenomena to full-scale LES by Merzari et al. using Cardinal, which is a lower-length-scale simulator that comprises three physics: neutronics, thermal fluids, and fuel performance [29, 30]. Additionally, the simulations of PBRs with Pronghorn using the porous medium approach have been demonstrated by other researchers [31–33].

In previous fiscal years (FYs), a model of the GPBR200 was developed with System Analysis Module (SAM) using the so-called core channel approach [34, 35]. In this approach, the core channel component in SAM is used to model the pebble bed of the GPBR200. The core channel is a SAM built-in component that consists of a 1D fluid component coupled to a 2D heat structure. Compared to the higher fidelity methods mentioned above, the core channel approach is faster and requires significantly fewer computational resources due to its lower resolutions and the use of correlations to solve for quantities such as pressure drop and heat transfer coefficients. As a result, despite the lower fidelity, the core channel approach is ideal for simulating long transients such as the loss-of-forced-flow accidents.

The work in FY24 is a continuation from the previous FYs with further improvements added to the core channel model. Additionally, for validation and verification, a 2D porous media model with higher resolutions and fidelity is developed with SAM and compared with the core channel model. A simplified water-cooled RCCS loop is also included in both the core channel and the porous media models. Steady-state simulations are first performed with both models. Next, transient simulations of the depressurized and pressurized loss-of-forced cooling (Depressurized Loss of Forced Cooling (DLOFC) and Pressurized Loss of Forced Cooling (PLOFC)) accidents are performed. In the coming sections, descriptions of both models are first provided, followed by the presentation of the simulation results, and lastly the conclusions.

4.2. Model Descriptions

4.2.1. Core Geometry

The GPBR200 reactor is chosen as the reference design in this work, focusing only on the core. Auxiliary components that make up the coolant system of the reactor are not included here to reduce the complexity of the model so that the thermal hydraulics behavior of the core could be properly studied. The design information of the reactor used here is obtained from the work by Stewart et al. based on publicly available figures and models [33]. The reactor has an installed thermal capacity of 200 MW, cooled by pressurized helium gas with the primary coolant pressure of 6 MPa, inlet and outlet core temperatures of 533 K and 1023 K, respectively, and a nominal helium mass flow rate of 78.6 kg/s during steady-state normal operating condition. The pebble-bed core has a packing factor of 0.61 and roughly 223,000 pebbles are loaded. The schematic of the GPBR200 core is shown in Figure 55 and the dimensions of the core are tabulated in Table 10.

Table 10. Dimensions of the GPBR200 core [33].

Features	Dimensions [m]
Core Radius	1.20
Reflector Width Between Core and Riser	0.52
Riser Width	0.18
Outer Reflector Width	0.21
Gap Between Reflector and Barrel	0.04
Barrel Thickness	0.04
Gap Between Barrel and RPV	0.08
RPV Thickness	0.09
Bottom Reflector Height	0.54
Core Height	8.91
Core Inlet Height	0.36
Riser Height	8.57
Top Gap Height	0.55
Top Reflector Height	0.85

4.2.2. SAM Core Channel Model

Based on the schematic shown in Figure 55 and the dimensions tabulated in Table 10, a SAM model for the GPBR200 core is built. The schematic of the SAM model is shown in Figure 56 with the assumption that the core is axially symmetric. In the SAM model, solid structures such as the reflectors, core barrel, Reactor Pressure Vessel (RPV), and RCCS panels are modeled with the *PBCoupledHeatStructure* components. Meanwhile, coolant channels, such as the upcomer and flow channels, in the bottom reflector are modeled as 1D flow with the *PBOneDFluidComponent*.

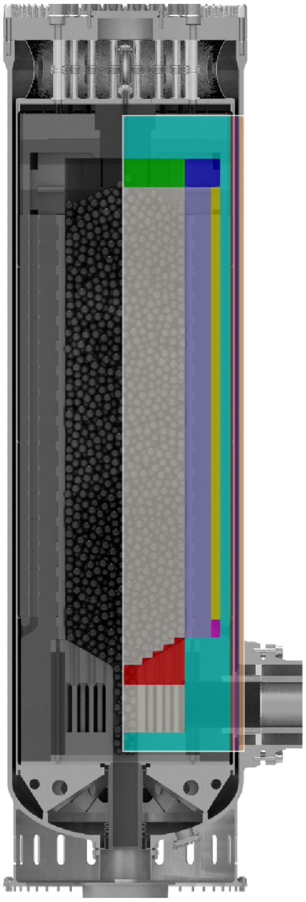

Figure 55. Schematic of the core of the GPBR200 [33].

The pebble bed is modeled with multiple *PBCoreChannel* components, each of which effectively represents a column of cylindrical or annulus of a pebble bed. Note that the *PBCoreChannel* is essentially a 1D fluid component with built-in heat structures that can simulate solid-to-fluid thermal fluid behaviors. This allows the specification of hydraulic parameters, such as flow area, hydraulic diameter, and surface roughness, as well as solid parameters, such as the geometry and material properties of the heat structure. Additionally, heat transfer parameters, such as the heat transfer area density, can be provided to the component. Solid, fluid, and heat transfer behaviors are then calculated internally by the *PBCoreChannel* component according to the provided information. The *PBCoreChannel* component is set to have spherical heat structures where the heat-transfer geometry is set as a pebble bed. The use of multiple *PBCoreChannels* in the radial direction allows the model to capture the radial heat conduction within the pebble bed and from the pebble-bed core to the reflectors, which is particularly important for loss-of-forced-flow transient scenarios where radial conduction plays a significant role in decay heat removal.

One major update implemented to the core channel model is the modeling of the lower reflector region located below the pebble bed. Previously, the lower reflectors and the pebble beds are modeled as separate components with the former being *PBCoupledHeatStructures* coupled to *OneDFluidComponent*. However, this approach severely underestimates the solid-to-solid heat transfers between the pebbles in the *PBCoreChannels* and the heat structures in the lower reflectors. Furthermore, during natural circulation and low flow conditions under certain transient scenarios, the lower reflector region has been observed internally by the authors to cause convergence issues to the model. As a result, a different approach to model the

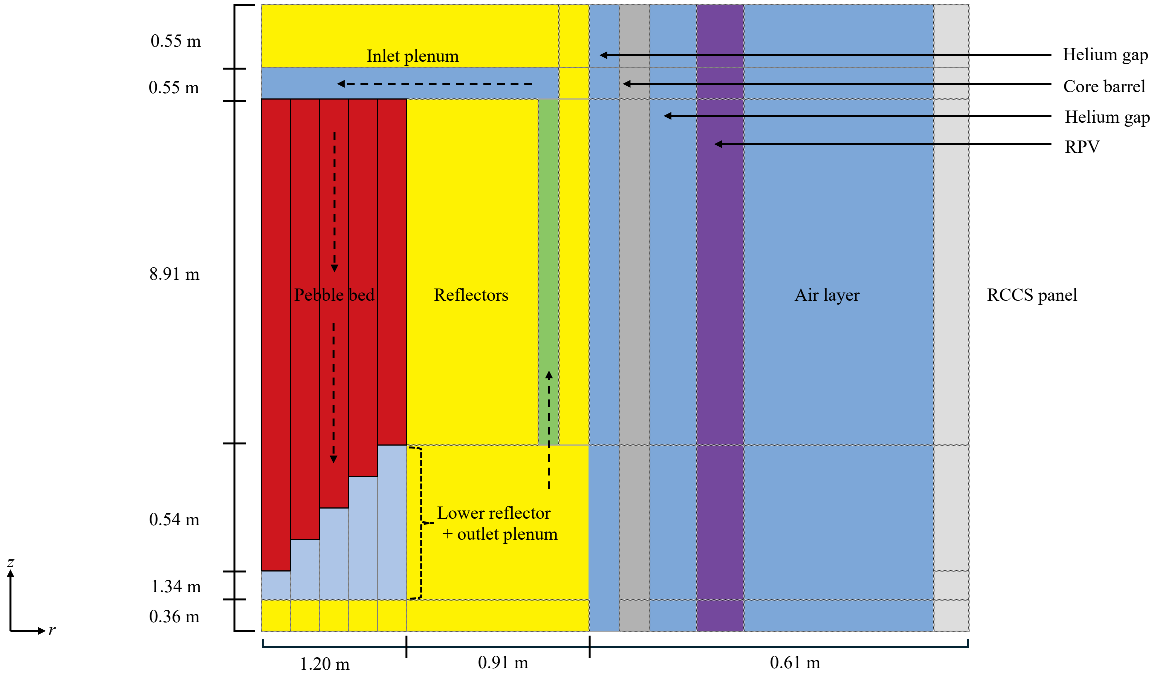

Figure 56. Schematic of the GPBR200 core for the SAM models (not to scale).

lower reflector is adopted. In the new approach, the pebble bed and lower reflectors are modeled using one *PBCoreChannel* with the heated region confined only to the pebble bed. A power density distribution obtained from the work of Stewart et al. is applied to the core channels [33]. This approach eliminates the need for additional heat structures and fluid components in the lower reflector. On top of that, the model convergence is improved substantially. However, this approach assumes the same porosity for the pebble bed and reflector regions as variable porosity is not currently available in *PBCoreChannel*.

The core channels used to model the pebble-bed core are essentially independent of each other. To allow for heat conduction between the core channels, the heat structures of the core channels need to first be thermally coupled to each other. In SAM, the thermal coupling of heat structures can be accomplished through the *SurfaceCoupling* component where the heat transfer rate is determined by a user-defined heat transfer coefficient, which is termed as h_{gap} in SAM. Based on the units of heat transfer coefficient, h_{gap} is determined as function of the core-wide effective thermal conductivity, k_{eff}, and a length-scale, L.

The k_{eff} is determined using the ZBS correlation, which calculates the effective thermal conductivity of the pebble-bed core with the consideration of pebble-pebble conduction, pebble-coolant convection and conduction, and pebble-pebble radiation [36, 37]:

$$\frac{k_{eff}}{k_f} = \left(1-\sqrt{1-\varepsilon}\right)\varepsilon\left[\left(\varepsilon-1+\frac{1}{\kappa_G}\right)^{-1}+\kappa_r\right]+\sqrt{1-\varepsilon}\left[\varphi\kappa+\left(1-\varphi\right)\kappa_c\right], \tag{8}$$

where φ is the surface fraction parameter for heat transfer through contact areas and ε is the porosity of the pebble bed core. The nondimensional effective thermal conductivity related to fluid phase conduction, κ_G, is simplified to be 1. For the nondimensional effective thermal conductivity related to thermal radiation, κ_r, and the contribution from the heat transfer due to solid conduction, fluid conduction, and thermal radiation, κ_c, more detailed descriptions are available from other researchers [36, 37].

Given h_{gap} dictates the heat transfer rate between adjacent core channels and hence the rate of radial heat

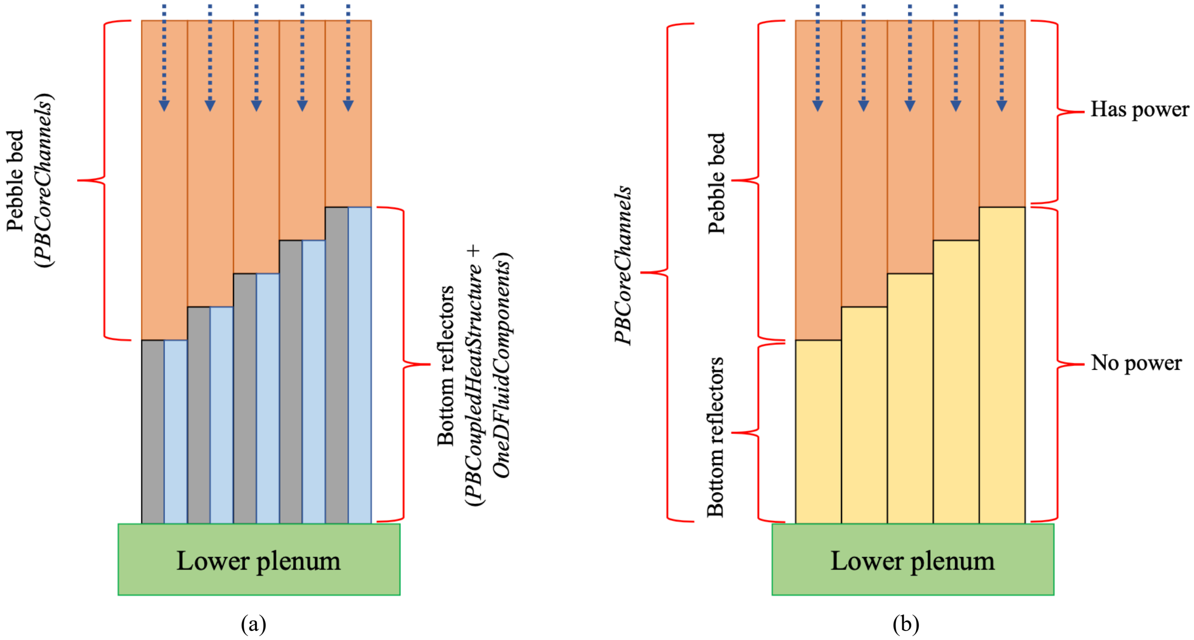

Figure 57. Changes in the modeling approach of the lower reflector region in the SAM core channel model where (a) is the previous approach and (b) is the updated approach.

conduction between adjacent core channels, the modeling of h_{gap} is further examined. In this work, h_{gap} is calculated as:

$$h_{gap} = \frac{k_{eff}}{\Delta L} \cdot \frac{A_{channel}}{A_{pebbles}}, \tag{9}$$

where ΔL is defined as the distance between the centers of adjacent core channels or heat structures, $A_{channel}$ is the surface area of core channels, and $A_{pebbles}$ is the total surface area of pebbles in each core channels. The area ratio is used to account for the difference of surface area of a core channel and the total surface area of pebbles in that channel. This approach to couple adjacent core channels has been validated using experimental data from the High Temperature Test Unit in FY23 [35].

A simplified natural-circulation-driven and water-cooled RCCS loop is added to the model. It is loosely based on the RCCS design used in the High-Temperature Gas-Cooled Reactor pebble-bed module (HTR-PM) reactors [38]. A schematic of the closed-loop RCCS is shown in Figure 58. The loop consists of an RCCS panel of equal height as the core and is thermally coupled to a riser channel. Downstream of the riser is the unheated chimney section and the inventory tank. A heat exchanger is added to the tank as the ultimate heat sink. The secondary side of the heat exchanger is not modeled. Instead, the inlet and outlet boundary conditions on the secondary side are modeled using a time-dependent junction and a time-dependent volume, respectively. The cooled water flows from the inventory tank back to the riser through the downcomer. Heat transfer from the external wall of the RPV to the internal wall of the RCCS panel occurs through thermal radiation. Natural convection happening in the enclosure between the RPV and the RCCS panel is not currently modeled. The loop is assumed to be at atmospheric pressure.

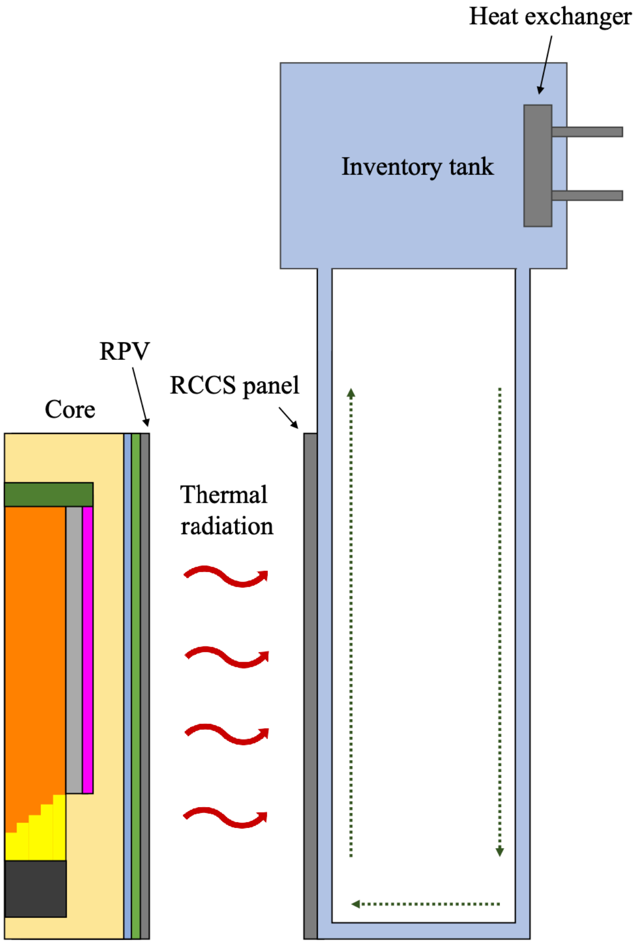

Figure 58. Schematic of the water-cooled closed-loop RCCS.

4.2.3. SAM Porous Media Model

The SAM porous media model consists of three individual models, namely the core, the primary loop, and the RCCS loop. The core is modeled using SAM's multidimensional flow model in 2D RZ geometry while the primary loop and RCCS are modeled with SAM's 0D and 1D components. The individual models are coupled to each other through the MOOSE MultiApp system [39].

The mesh of the 2D RZ core of the porous media model is shown in Figure 59. The pebble bed and the bottom reflectors are modeled as porous media while the side reflectors, core barrel, helium gaps, and RPV are modeled as solid. Note that the inlet and outlet plena are not modeled in the 2D porous media model but are instead modeled as 0D volume branches using the SAM component system in the primary loop model.

On the other hand, the riser is modeled using an approach that utilizes both the 2D meshes and the 1D component system. In the 2D model, even though the riser is meshed, it is treated as a solid component (rather than porous media) whose thermal physical properties are reduced by a factor of $1 - porosity$. This means that, in the 2D mesh, there is no fluid flow in the riser. Instead, the fluid flow in these two channels are modeled as 1D flow using *PBOneDFluidComponent* in the primary loop model. Conjugate heat transfer between these channels with the surrounding 2D solid structures is also modeled. This combined approach avoids the need to mesh the two channels in the 2D model while still capturing the radial heat conduction from the core to the surrounding reflectors.

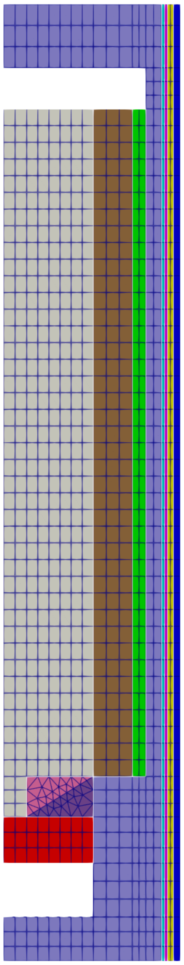

Figure 59. Mesh of the 2D RZ core of the SAM porous media model.

The primary loop model essentially consists of three individual models. These are the cold leg consisting of the riser, cold plenum, and inlet and outlet boundary conditions, the hot leg consisting of the hot plenum, outlet channel, and inlet and outlet boundary conditions, and the surrogate channel with inlet and outlet boundary conditions. The surrogate channel is needed for the domain overlapping approach, which will be explained later in this section. Given that the focus of the current work is on the modeling of the core, a simplified primary loop with inlet and outlet boundary conditions is adopted to reduce the complexity of the model. It should be pointed out that this simplification neglects loop-wide natural circulation that may occur during certain transients. Once the core model is comprehensively verified and benchmarked, the model will be expanded to include components such as the steam generator and helium blower to close the primary loop. Finally, the RCCS loop is the same as that used in the core channel model, as described in Section 4.2.2.

In the domain overlapping approach, the primary loop model contains the entire domain, including a component that overlaps with the multidimensional model domain. It is different than the conventional domain decomposition approach where the primary loop and core are split into separate models with data exchange happening at the boundaries. The domain overlapping approach is adopted in this work because it has been shown to improve the accuracy and numerical stability of simulations compared to the conventional domain decomposition approach [40]. As shown in Figure 61, the inlet velocity of the porous media core and the surrogate channel are set to those from the cold plenum in the cold leg. The multidimensional core is

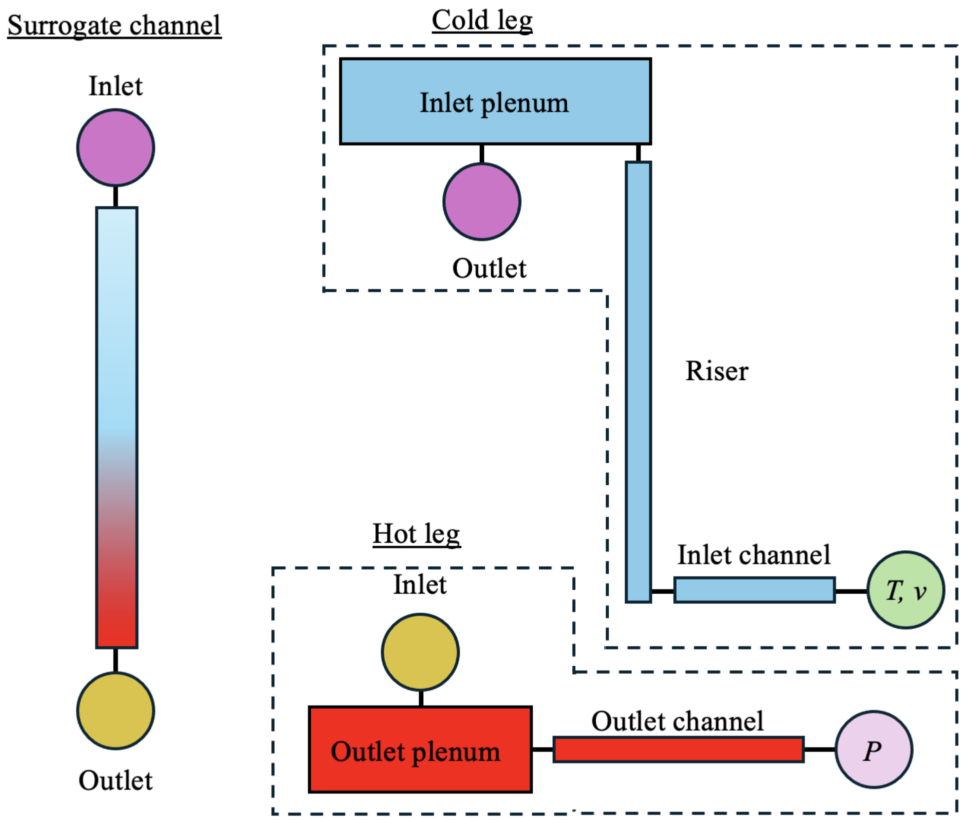

Figure 60. 0D/1D primary loop of the SAM porous media model.

given a flow-direction-dependent temperature boundary condition at the inlet where the temperature is set to the outlet temperature of the 1D primary loop only during downward flow. During flow reversal where helium flows upward, the inlet temperature of the multidimensional core is not set. Next, the inlet temperature of the surrogate channel is set to that from the inlet of the multidimensional core. Frictional pressure drop across the multidimensional core is computed and transferred to the primary loop model where it is imposed to the surrogate channel. Given that the surrogate channel has the same inlet condition and pressure drop as the multidimensional core, the resultant flow rate in the surrogate channel is also the same as that in the multidimensional core. Finally, to ensure energy balance between the models, the temperatures at the outlet of the surrogate channel and the hot plenum are set to the outlet temperature of the multidimensional core.

The coupling between the core, primary loop, and RCCS models is accomplished through the MOOSE MultiApp system [39]. The porous media model is the *MainApp* while the other two models are the *SubApps*. The *MainApp* controls the coupling between the different *Apps* and facilitates the transfer of information between each other. Figure 62 summarizes the coupling and transfer of information in the model. The core model transfers the outlet temperature and velocity, as well as the pressure drop across the porous region to the primary loop model (*SubApp*-1). In return, the core model receives inlet temperature and velocity and outlet pressure from the primary loop model. At the same time, riser fluid temperature, heat transfer coefficient, and wall temperature are also exchanged between the two *Apps* to model the conjugate heat transfer between the multidimensional wall and the fluid in the 1D riser. On the other hand, the core model also transfers layered averaged radiation heat flux at the RPV external wall to the RCCS model. In return, the core model receives the layered averaged inner wall temperature of the RCCS panel and uses that as the T_∞ for its radiative boundary condition. Picard iteration is performed at every exchange of information to ensure

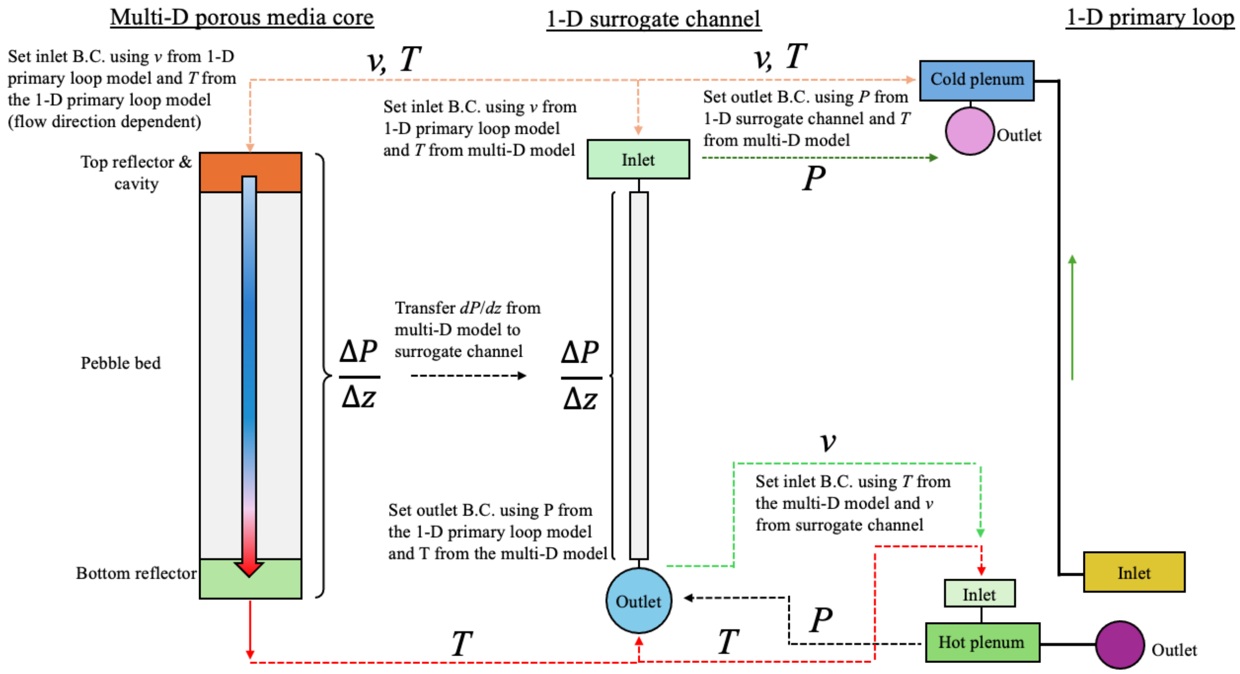

Figure 61. Depiction of the domain overlapping approach used for coupling the porous media core and primary loop models.

convergence.

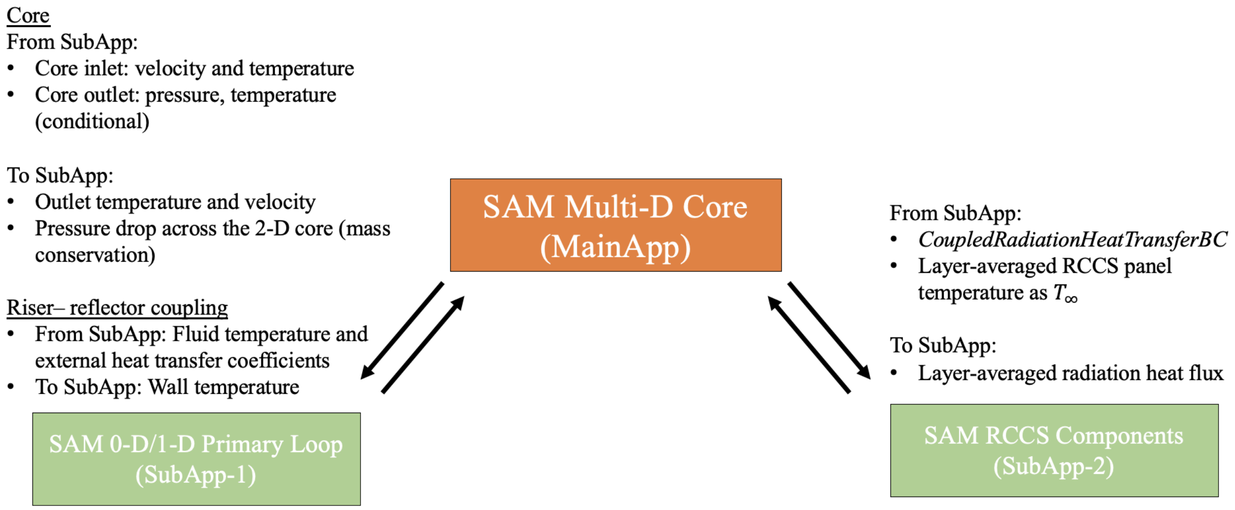

Core
From SubApp:
- Core inlet: velocity and temperature
- Core outlet: pressure, temperature (conditional)

To SubApp:
- Outlet temperature and velocity
- Pressure drop across the 2-D core (mass conservation)

Riser– reflector coupling
- From SubApp: Fluid temperature and external heat transfer coefficients
- To SubApp: Wall temperature

SAM Multi-D Core (MainApp)

From SubApp:
- *CoupledRadiationHeatTransferBC*
- Layer-averaged RCCS panel temperature as T_∞

To SubApp:
- Layer-averaged radiation heat flux

SAM 0-D/1-D Primary Loop (SubApp-1)

SAM RCCS Components (SubApp-2)

Figure 62. *MultiApp* coupling of the SAM core, primary loop, and RCCS models.

4.3. Results And Discussions

4.3.1. Steady-State Normal Operating Condition

The steady-state normal operating condition is simulated with the core channel and the porous media models. The normal operating condition the reactor operates at 200 MWth at a system pressure of 6 MPa.

Helium enters the core at 523.15 K with a mass flow rate of 78.6 kg/s. The power density distribution obtained by Stewart et al. using a Pronghorn-Griffin coupled simulation is imposed on both models [33]. The results from both models are summarized in Table 11. Overall, both models agree very well with the relative differences being smaller than 0.5%. The core channel model predicts an outlet helium temperature of 1022.4 K while the porous media model predicts a lower value of 1017.7 K where the theoretical outlet temperature is 1023 K. The core channel model also predicts a slightly higher mean and maximum pebble surface temperature than the porous media model.

Table 11. Comparison of the SAM core channel and porous media models for the steady-state normal operating condition.

	Core Channel	Porous Media	Relative Differences [%]
Inlet Temperature (inlet B.C.) [K]	533.0	533.3	NA
Outlet Temperature [K]	1022.4	1017.7	0.46
Mean Pebble Surface Temperature [K]	801.1	800.3	0.10
Maximum Pebble Surface Temperature [K]	1104.5	1096.6	0.72

Figures 63 and 64 compare the axial fluid temperature, pebble surface temperature, and velocity profiles between core channel and porous media models at radial locations of *r* = [0, 0.36, 0.57, 0.78, 0.99] m. The solid lines are from the porous media model while the dashed lines are from the core channel model. Overall, an excellent agreement is observed between the models for fluid and pebble surface temperatures, especially near the inner region of the pebble bed. Some small disagreements are observed towards the outer region of the pebble bed. Near the bottom of the pebble bed, the pebble surface temperature experiences a small drop due to heat transfer from the pebble bed to the unheated bottom reflectors. The dip in temperature is well captured by both models. The axial velocity profiles from both models also show good agreement. As helium flows downward from the top to the bottom of the pebble bed, it is heated by the fuels, causing the helium density to decrease and accelerating the velocity.

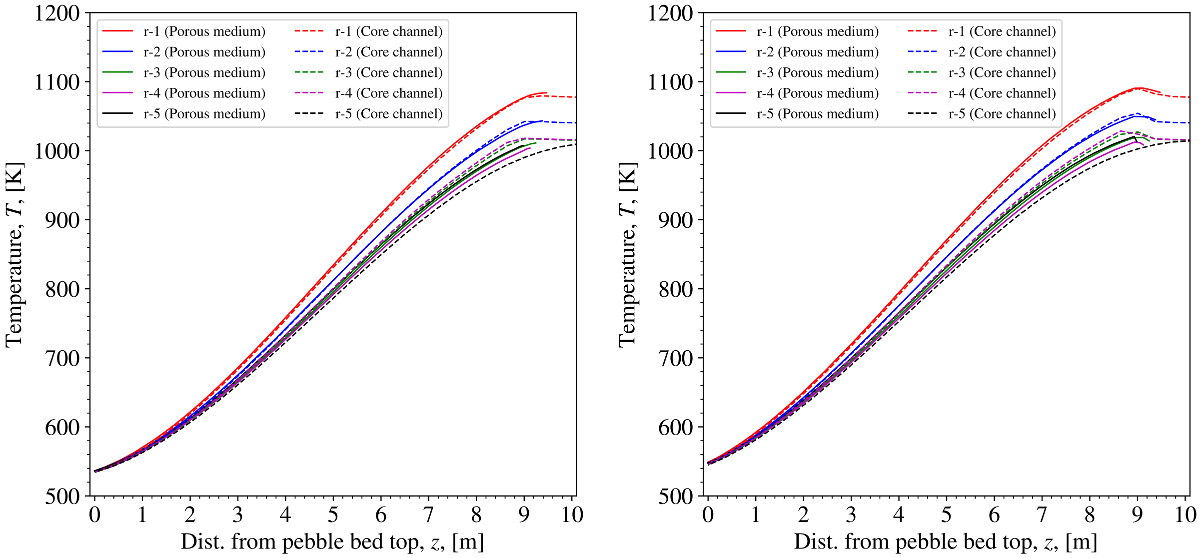

(a) (b)

Figure 63. Comparison of the axial temperature profiles of (a) fluid and (b) pebble surfaces between the SAM core channel and porous media models.

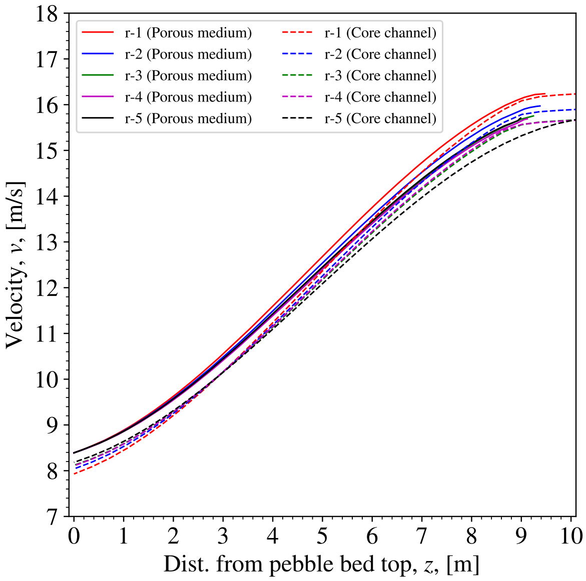

Figure 64. Comparison of the axial velocity profiles between the SAM core channel and porous media models.

The solid and fluid temperature distributions predicted by the core channel and porous media models are presented in Figures 65 and 66, respectively. Note that the power density distribution imposed to the porous media model is also included in Figure 66. The power density shows a bimodal distribution with a peak near the inner region of the pebble bed and another peak at the outer region close to the side reflector. The outer peak forms because a considerable amount of neutrons escape the bed and are thermalized and scattered back into the pebble bed [33]. Qualitatively, the temperature distributions of both models are in good agreement. Both models show a maximum temperature of around 1100 K. In both models, the pebble bed shows a significantly higher temperature than the surrounding regions, such as the reflectors. This indicates that, during steady-state normal operating conditions, the heat produced by the pebbles is primarily removed by the coolant where only a small amount of heat is lost to the surrounding solid regions. Furthermore, the flow of helium in the bypass and the riser acts as another layer of barrier that restricts the flow of heat from the pebble bed to the reflectors.

Overall, the core channel and the porous media models show good agreement during steady-state normal operating conditions. The mean and maximum pebble surface temperatures predicted by both models are shown to be within 0.5% of each other. The axial temperature and velocity profiles also show good agreement with each other. In the coming section, a transient loss-of-flow accident is simulated and discussed.

4.3.2. Protected DLOFC Accident

The SAM core channel and multidimensional porous media models are shown to agree well during steady-state normal operating conditions. In this section, the protected DLOFC accident is simulated with the two models and the results are compared. During DLOFC, the helium blower is tripped, causing a loss of forced cooling. At the same time, the pressure boundary is lost, leading to the depressurization of the core. In the protected DLOFC, the reactor is scram and the reactor power is reduced to decay heat level.

DLOFC is one of the most severe accidents that can happen to the GPBR200. Due to the depressurization, helium inventory in the core is lost, which means that in-core natural circulation cannot be established. Decay heat can only be transferred through radial conduction and thermal radiation from the pebble bed to the

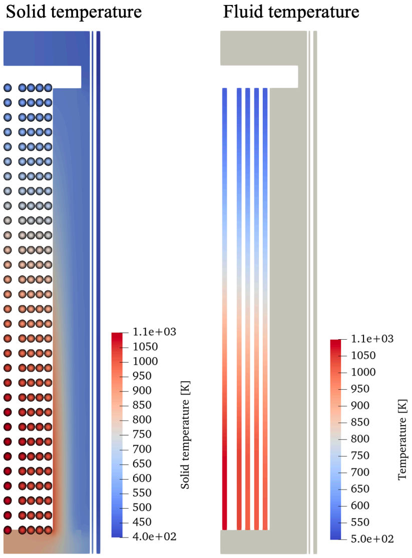

Figure 65. Distributions of solid temperature and fluid temperature predicted by the core channel model.

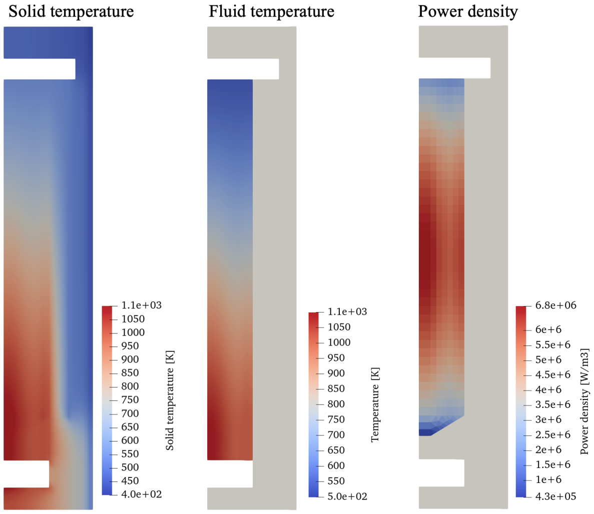

Figure 66. Distributions of solid temperature, fluid temperature, and power density predicted by the porous media model.

RPV through layers of structures such as the side reflectors, core barrel, and helium gaps. In the actual system, decay heat is transferred from the RPV through thermal radiation and natural convection to the RCCS. Currently, natural convection in the RCCS cavity is not included as its contribution is substantially smaller than thermal radiation. The effects of natural convection in the RCCS cavity will be considered in future work. In the current model, convective heat transfer is not modeled in the pebble bed during the transient because its effect is negligible due to the fact that helium density is significantly lower at the transient pressure of 1 atm than the normal operating pressure of 7 MPa. This means that the results shown here represent the upper limit of the DLOFC transient. However, it should be mentioned that, in some transients depending on the location of the break, flow reversal may occur and cause hot coolant to re-enter the core, which in turn may redistribute the heat in the pebble bed. Such a phenomenon is not captured by the current model as convection is not considered.

Steady state is first established before the start of the transient. At $t = 0$ seconds, the DLOFC transient is initiated by reducing the flow rate from the nominal value to zero linearly over 13 seconds following the recommendation by the OECD-NEA 400 MW Pebble Bed Modular Reactor (PBMR400) transient report [41]. Simultaneously, the reactor is scram and the power level is reduced according to a decay heat curve [41].

Figures 67 and 68 show the distributions of solid temperature during the DLOFC transient predicted by the core channel and porous media models, respectively. Overall, both models predict similar temperature distributions during the transient. At the beginning of the transient, the lower half of the pebble bed is hotter due to helium flowing from the top to the bottom of the pebble bed. As the transient progresses, the hot spot in the pebble bed starts to shift upward following the power density distribution shown in Figure 66. At the same time, the overall temperature of the pebble bed also increases until the peak temperature is reached at about 50,000 seconds. After that, as heat is transferred to the side reflectors, the pebble-bed temperature starts to come down. The decay heat is transferred radially across the reactor before it reaches the RPV where it is radiated to the RCCS and removed by the water in the RCCS.

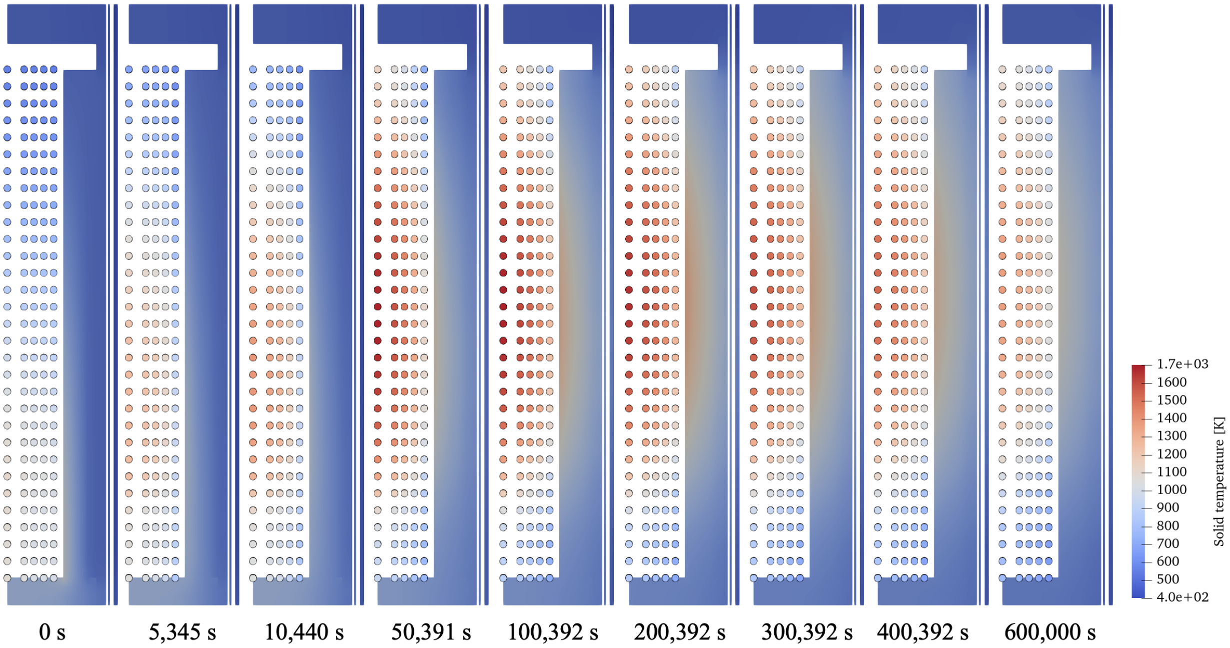

Figure 67. Distributions of solid temperature predicted by the SAM core channel model during the DLOFC transient.

Figure 69 compares the mean and maximum solid temperatures of the pebble bed predicted by the SAM core channel and the porous media models. The mean temperatures predicted by both models have an excellent agreement whereas the porous media model predicts a higher maximum temperature than the core channel model by about 60 K. Nevertheless, the maximum temperatures predicted by both models are still lower than the theoretical safety limit of tristructural isotropic fuel of about 1900 K. As expected, the innermost channel shows the highest temperature in the core channel model. The predictions from both models show a similar trend where the temperature rises sharply at the beginning of the transient and reaches the maximum value at roughly $t = 15$ hours. After that the pebble-bed temperature shows a gradual decrease for the remainder of the simulation.

Figure 70 compares the average reflector, core barrel, and RPV temperatures predicted by the core channel and porous media models. The solid lines are the results from the core channel model while the dashed lines are the results from the porous media model. The overall trends of the predictions between the models are

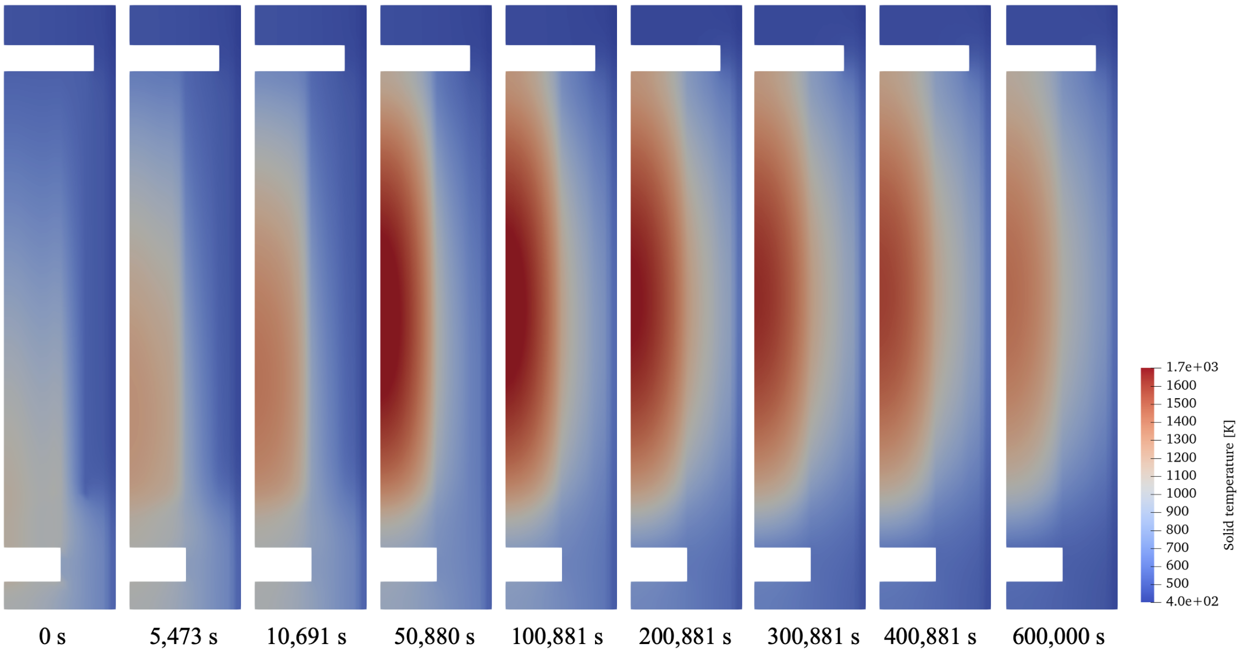

Figure 68. Distributions of solid temperature predicted by the SAM porous media model during the DLOFC transient.

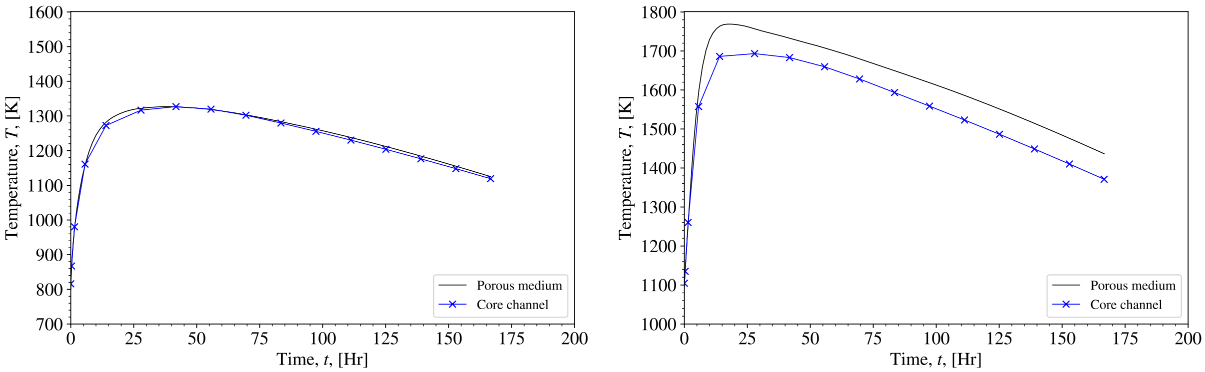

(a)

(b)

Figure 69. Comparison of the (a) mean and (b) maximum solid pebble-bed temperature predicted by the SAM core channel and porous media models during DLOFC.

similar where the temperatures are observed to increase initially and peak at roughly t = 50 hours before coming down gradually. However, the core channel model consistently predicts a higher average temperature across the three regions.

The RCCS mass flow rate as well as the RCCS inlet and outlet temperatures predicted by the models are shown in Figure 71. The overall trends of the predictions are similar between the models. The porous media model shows a higher steady-state flow rate of about 82 kg/s compared to the 64 kg/s predicted by the core channel model. However, during a transient, both models predict a rapid increase of mass flow rate until a peak value of roughly 105 kg/s is reached at about t = 50 hours. After that, an excellent agreement is observed between the two predictions as they gradually decrease. On the other hand, the inlet and outlet temperatures of the RCCS also show similar behaviors. Initially, the porous media model shows a slightly higher initial

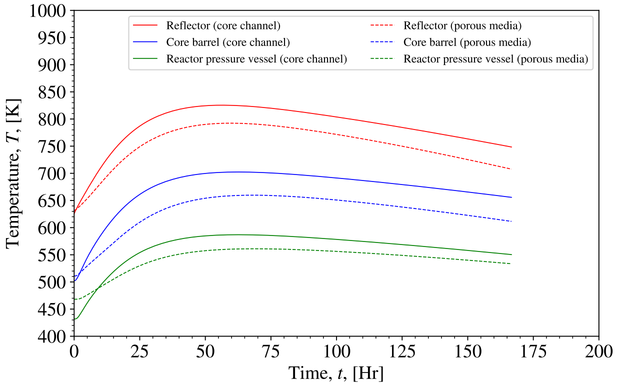

Figure 70. Comparison of the average reflector, core barrel, and RPV temperatures predicted by the core channel and porous media models during DLOFC.

inlet and outlet temperature, which leads to a higher mass flow rate. However, as the transient progresses, the agreement between the two models also improves. At its peak, the water in the RCCS experiences an increase of roughly 2 K across the heated region.

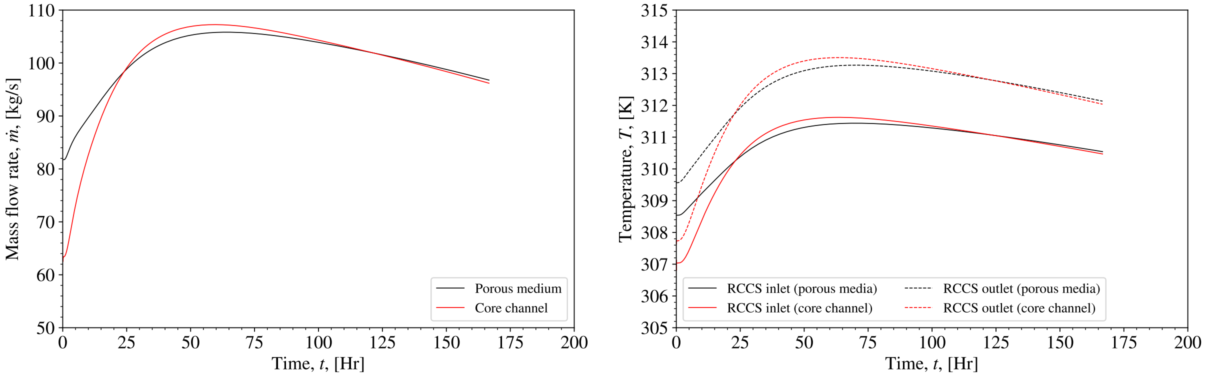

(a)

(b)

Figure 71. Comparison of the (a) RCCS mass flow rate and (b) RCCS inlet and outlet temperatures predicted by the SAM core channel and porous media models during DLOFC.

The RCCS heat removal rate predicted by the models are shown in Figure 72 along with the decay heat produced by the reactor. The heat removal rates by both models are similar with a peak value of roughly 800 kW. At about $t = 50$ hours, the heat removal rate exceeds the decay heat. As more heat is removed by the RCCS than generated by the reactor, the overall temperature of the core also falls accordingly. It should be emphasized that the heat removal rate of the RCCS is dependent on the design. Thus, the quantitative results predicted by the models may not accurately reflect those from an actual reactor. However, the qualitative results and the overall trends predicted by the models should still be relevant.

4.3.3. Protected PLOFC Accident

In this section, the PLOFC accident is simulated with the two models and the results are compared. The PLOFC accident is similar to the DLOFC accident, with the difference being that the pressure boundary is intact in the former. As a result, in-core natural circulation is established during PLOFC, which plays an

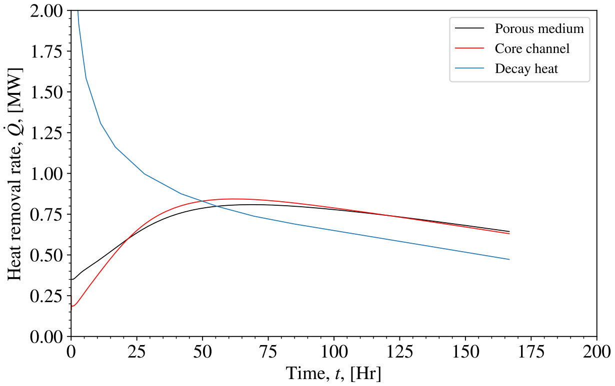

Figure 72. Comparison of the RCCS heat removal rate predicted by the SAM core channel and porous media models during DLOFC.

important role in the removal of decay heat. It should be noted that the current model does not include the effects of natural circulation in the primary loop as the inlet flow rate is explicitly set to zero.

The steady-state normal operating condition is established in both models prior to the transient. At the beginning of the transient, the helium flow rate is decreased linearly from 0 to 13 seconds. Simultaneously, the reactor is scram and the power level is determined using a decay heat curve [41]. The pressure boundary condition throughout the simulation is kept at 7 MPa.

Figures 73 and 74 show the solid temperature distributions predicted by the core channel and porous media models during PLOFC, respectively. Note the difference in the temperatures scales of the two figures. The core channel model has a higher maximum temperature of 1500 K while the porous media model only has a maximum value of 1300 K. Nevertheless, the overall trends predicted by both models are similar. The shift of the hot zone from the bottom of the core to the upper half of the core is predicted by both models. Furthermore, both models also show the transfer of decay heat from the pebble bed to the side reflectors and eventually to the RCCS.

Figure 75 compares the mean and maximum solid temperatures predicted by the SAM core channel and porous media models during PLOFC. The core channel model consistently shows a higher prediction of mean and maximum solid temperatures throughout the transient by roughly 100 K and 200 K, respectively. However, the overall trends predicted by both models agree well. For example, both models show a peak in the maximum temperature in the first 10 hours of the transient. The maximum temperatures then show a small decrease before increasing again and finally peaking at about $t = 45$ hours. The first peak is due to the reduction of convective heat transfer as the pump is tripped while the second is due to the decay heat in the core. A similar twin-peak temperature profile has been reported by Zheng et al. who model the HTR-PM reactor with TINTE and SPECTRA [42].

Figure 76 compares the RCCS heat removal rate predicted by the core channel and porous media models. Overall, the heat removal rates are similar with the core channel model showing a slightly higher value, which is consistent with the observation in the DLOFC case shown in Figure 72.

Compared to DLOFC, the PLOFC simulation shows larger discrepancies between the core channel and porous media models. In DLOFC, decay heat is conducted radially across the pebble bed to the surrounding solid structures and finally to the RCCS panel via thermal radiation. On the other hand, in PLOFC, in-core natural circulation plays a role in the redistribution of heat in the pebble bed and accelerates the transfer of heat to the surrounding side reflectors. As a result, PLOFC has a lower peak temperature that is reached sooner than DLOFC. This means that the prediction of natural circulation rate plays an important role in PLOFC.

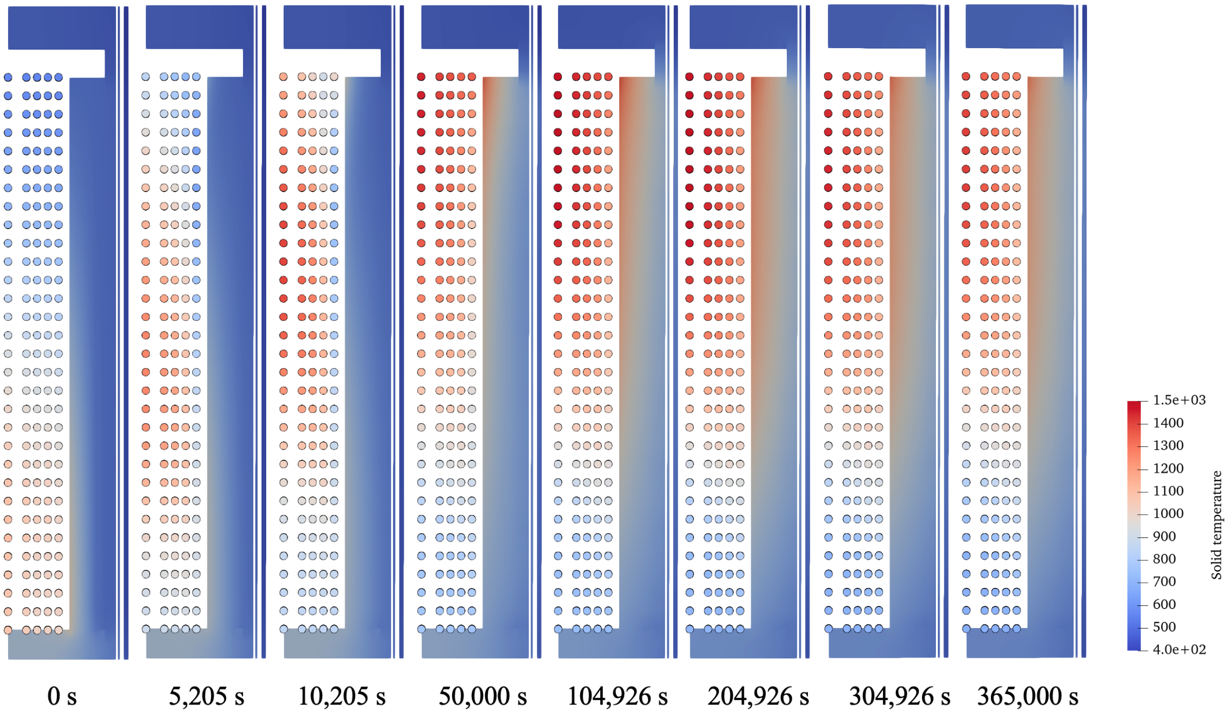

Figure 73. Distributions of solid temperature predicted by the SAM core channel model during the PLOFC transient.

In the core channel model, the helium flow path in the pebble bed is restricted by the number and locations of the core channels. This approach is applicable in the steady-state normal operating condition because helium primarily flows from the top to the bottom of the core. However, during PLOFC where forced flow is lost, the establishment of in-core natural circulation means that the flow structure in the pebble bed is much more complex where flow reversal and cross flow exist.

The complexity of the flow structure during PLOFC is shown by the velocity profiles and streamlines predicted by the porous media model shown in Figure 77. At t = 0 seconds, helium is observed to flow vertically from the top to the bottom of the core with no cross flow. However, roughly 1,000 seconds from the beginning of the transient, natural circulation is observed where helium flows upward in at the hotter inner core and downward at the colder outer core. As the transient progresses, large vortices are observed at the top and bottom of the core. Evidently, significant cross flow is predicted by the model.

Figure 78 compares the velocity profiles predicted by the SAM core channel and porous media models during PLOFC. The velocities are obtained at the top and bottom of the pebble bed at five radial locations denoted as CH-1–CH-5. In the porous media model, the velocities are the mean values obtained from r_{in} = [0, 0.36, 0.57, 0.78, 0.99] to r_{out} = [0.36, 0.57, 0.78, 0.99, 1.2]. Note that positive values represent downward flows and negative values represent upward flow. In the core channel model, CH-1–CH-4 show upward flows while downward flow only happens in CH-5. Even though the core channel model is able to show natural circulation in the core, due to its inability to model cross flow, the direction change can only happen in the top and bottom plena. This means that flow in each channel has to travel the entire length of the core channel before the flow direction changes. This is evident in Figure 78 (a) where the flow directions at the top and bottom of the core are always the same. On the other hand, the porous media model shows that the flow directions at the bottom and top of a channel are not always the same due to cross flows. For example, in the first 20 hours of the transient, the top and bottom velocities in CH-1–CH-3 have the same upward flow

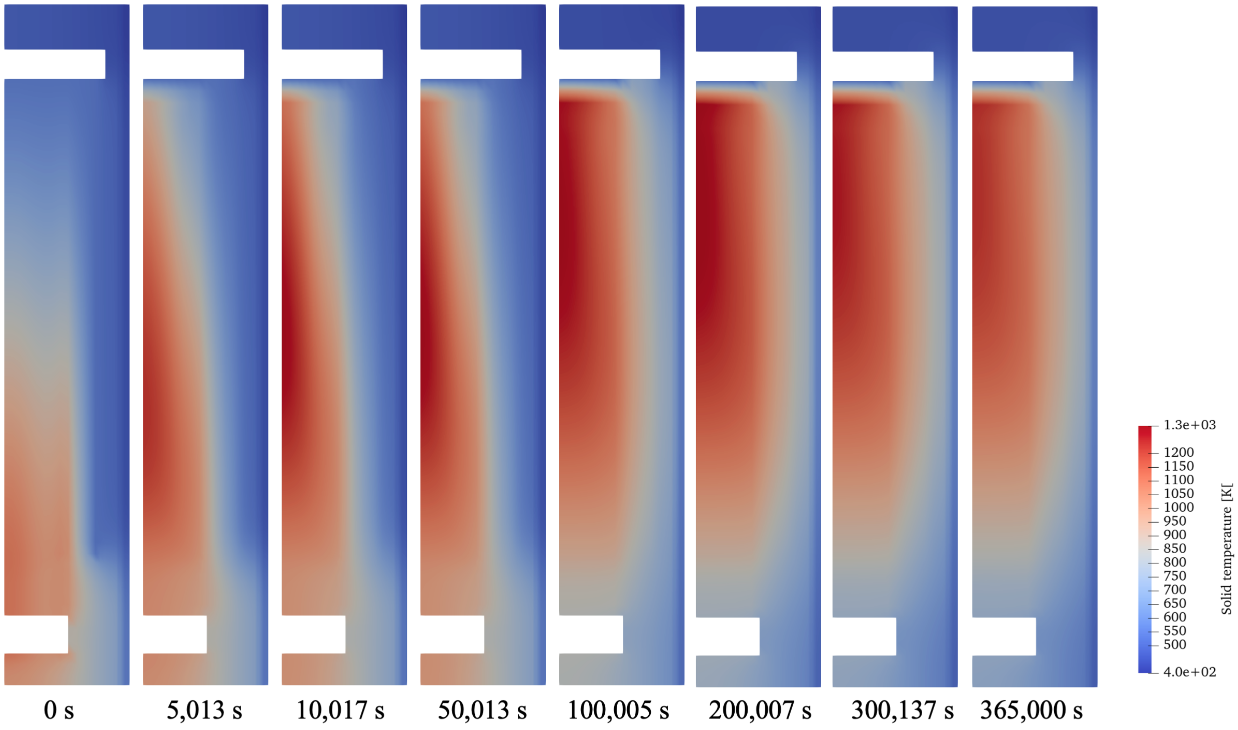

Figure 74. Distributions of solid temperature predicted by the SAM porous media model during the PLOFC transient.

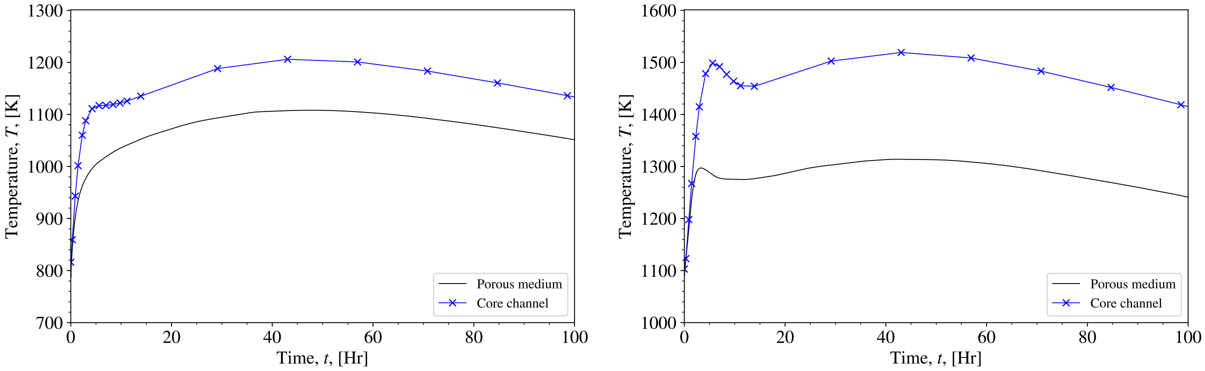

(a)

(b)

Figure 75. Comparison of the (a) mean and (b) maximum solid pebble-bed temperature predicted by the SAM core channel and porous media models during PLOFC.

directions. However, this changes from t = 20 hours onward as the bottom velocities become downward while the top velocities remain upward due complex flow features, such as the formation of vortices. The existence of cross flows in the porous media model also enhances mixing in the core that improves heat transfer from the hotter inner core to the colder outer core. Using the profile at t = 100,005 seconds in Figure 77 as an example, cold helium from the outer region of the core is continuously drawn inward to the hotter inner region as it flows upward. Conversely, such flow behaviors is not possible in the core channel model because the helium flow in the outer channels is independent of the flow in the inner channels. This means that helium in the hot inner channels is heated up more due to longer residence time in the channel, which in

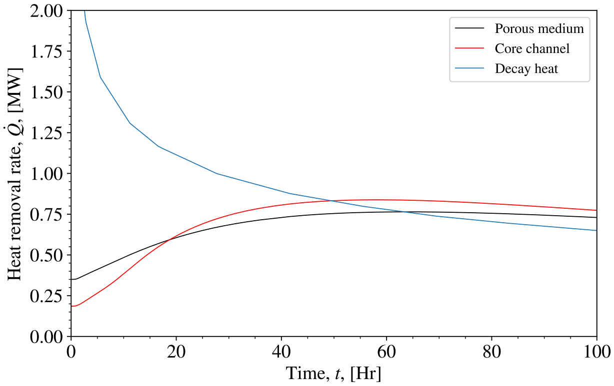

Figure 76. Comparison of the RCCS heat removal rate predicted by the SAM core channel and porous media models during PLOFC.

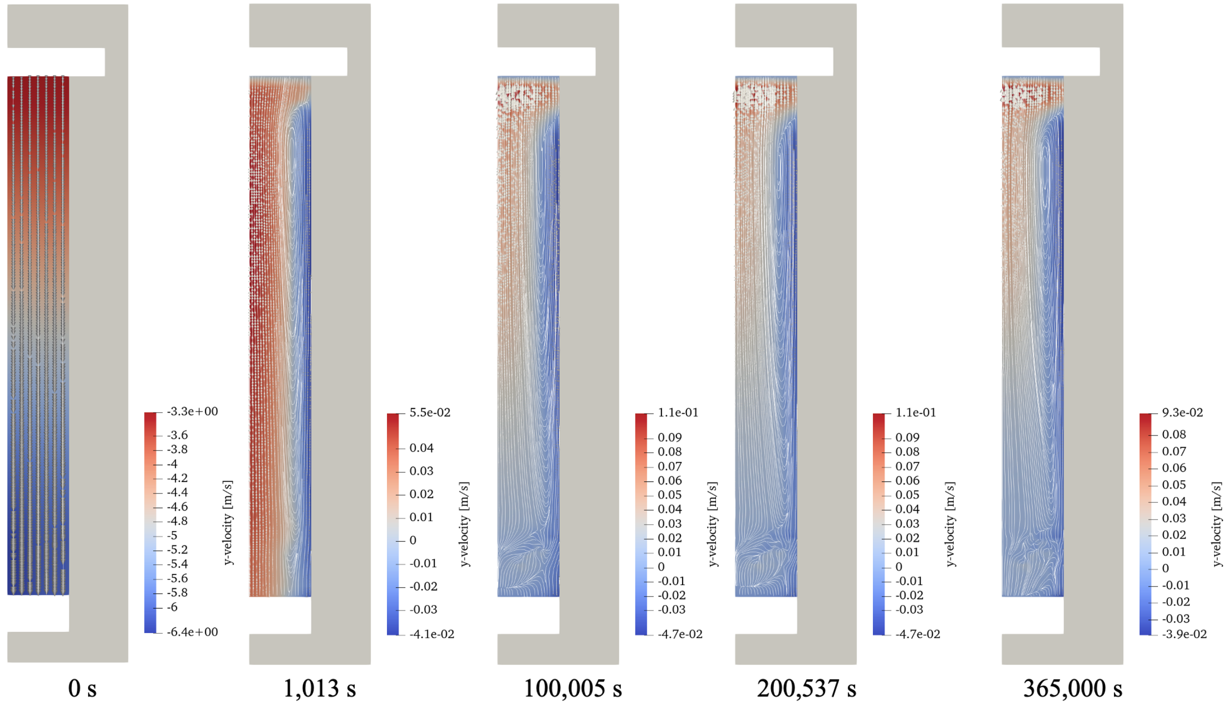

Figure 77. Streamlines and velocity profiles predicted by the SAM porous media model during PLOFC.

turn results in poorer heat removal.

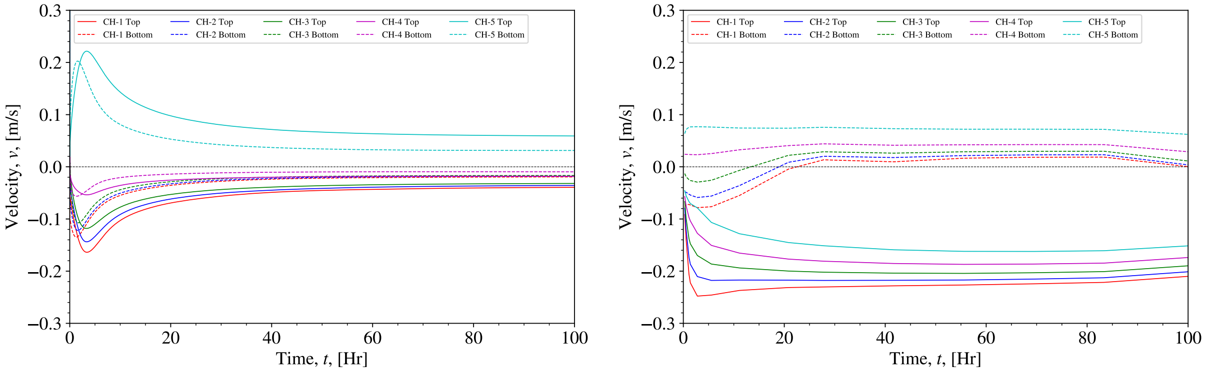

(a)

(b)

Figure 78. Comparison of the velocity profiles between the (a) core channel and (b) porous media models during PLOFC. Positive values represent downward flows and negative values represent upward flow.

4.4. Summary And Future Steps

SAM core channel and porous media models are developed for the GPBR200 reactor. The porous media model uses the so-called domain overlapping approach to ensure numerical stability and conservation of mass. Additionally, an RCCS loop is added to both models for decay heat removal. Both models compare well during steady-state normal operating conditions, where good agreements are obtained for the velocity and temperature profiles and other key parameters are within 1% of each other.

The protected DLOFC accident is then simulated. In this accident, due to the depressurization of the core, the effects of convection in heat removal is negligible and decay heat is primarily removed via radial conduction from the pebble bed to the RPV and via thermal radiation to the RCCS. Thus, a conservative approach is adopted where convective heat transfer is disabled for both models. Again, the predictions from the core channel and porous media models agree well with each other. The mean solid temperatures in the core predicted by both models show an excellent agreement while the core channel model shows a slightly higher maximum temperature than the porous media model. Nevertheless, the maximum temperatures from both models are well below the safety limit of tristructural isotropic fuel of about 1900 K despite the conservative approach [42].

Additionally, the protected PLOFC accident is simulated. PLOFC is similar to DLOFC with the only difference being that the pressure boundary is intact so convective heat transfer plays a significant role in the removal of decay heat. The core channel model predicts a higher overall temperature than the porous media model, suggesting that the effects of convective heat transfer are underpredicted by the core channel model. The core channel model fails to predict vortices and cross flow in the core, which likely contributes to the underprediction of convective heat transfer. Nevertheless, the core channel model is able to predict agreeable trends for major parameters with respect to the porous media model.

For future steps, the effects of cross flow during PLOFC will be investigated and new capabilities will be added to the SAM core channel components to model cross flow if necessary. Furthermore, both models will also be further tested with other transient scenarios, especially those that incorporate neutronics and feedback calculations.

5. ACKNOWLEDGEMENT

Argonne National Laboratory's work was supported by U.S. DOE Office of Nuclear Energy's Nuclear Energy Advanced Modeling and Simulation (NEAMS) program, through U.S. Department of Energy contract

DE-AC02-06CH11357. The authors would like to thank Dr. Sung Nam Lee from Korea Atomic Energy Research Institute for providing HTTF benchmark results using GAMMA+.

6. REFERENCES

[1] Wang, Y., Prince, Z. M., Calvin, O. W., Park, H., Choi, N., Jung, Y. S., Schunert, S., Kumar, S., Hanophy, J., Laboure, V., Lee, C., Ortensi, J., Harbour, L., and Harter, J. (2024) Griffin: A Moose-Based Reactor Physics Application for Multiphysics Simulation of Advanced Nuclear Reactors. *Available at SSRN,*.

[2] Giudicelli, G., Lindsay, A., Harbour, L., Icenhour, C., Li, M., Hansel, J. E., German, P., Behne, P., Marin, O., Stogner, R. H., Miller, J. M., Schwen, D., Wang, Y., Munday, L., Schunert, S., Spencer, B. W., Yushu, D., Recuero, A., Prince, Z. M., Nezdyur, M., Hu, T., Miao, Y., Jung, Y. S., Matthews, C., Novak, A., Langley, B., Truster, T., Nobre, N., Alger, B., Andrs, D., Kong, F., Carlsen, R., Slaughter, A. E., Peterson, J. W., Gaston, D., and Permann, C. (2024) 3.0 - MOOSE: Enabling massively parallel multiphysics simulations. *SoftwareX,* **26**, 101690.

[3] kugelpy. `https://github.com/idaholab/kugelpy` (2024).

[4] Leppänen, J., Pusa, M., Viitanen, T., Valtavirta, V., and Kaltiaisenaho, T. (2015) The Serpent Monte Carlo code: Status, development and applications in 2013. *Annals of Nuclear Energy,* **82**, 142–150.

[5] Hanophy, J., Ortensi, J., Balestra, P., and Wang, Y. (4, 2024) Initial Demonstration of New Griffin Capability for Simulating the Running-In Phase of Pebble-Bed Reactors with Multiphysics. In *Proceedings of the international conference on physics of reactors-PHYSOR 2024* San Francisco, CA: pp. 2278–2287.

[6] Hanophy, J., Balestra, P., Wang, Y., Schunert, S., and Ortensi, J. (2024) Multiphysics Simulations of the Running-In Phase of Pebble-Bed Reactors with Griffin. *submitted to Nuclear Science and Engineering,*.

[7] Stewart, R., Cavaluzzi, J., Balestra, P., and Strydom, G. (2024) Capturing the run-in of a pebble-bed reactor by using thermal feedback and high-fidelity neutronics simulations. *Annals of Nuclear Energy,* **207**, 110697.

[8] Schunert, S., Ortensi, J., Wang, Y., Balestra, P., Jaradat, M., Calvin, O., Hanophy, J., and Harbour, L. (2023) An equilibrium core depletion algorithm for pebble-bed reactors in the Griffin code. *Annals of Nuclear Energy,* **192**, 109980.

[9] Stewart, R., Balestra, P., Reger, D., Merzari, E., and Strydom, G. (2024) High-fidelity simulations of the run-in process for a pebble-bed reactor. *Annals of Nuclear Energy,* **195**, 110193.

[10] Giudicelli, G. L., Abou-Jaoude, A., Novak, A. J., Abdelhameed, A., Balestra, P., Charlot, L., Fang, J., Feng, B., Folk, T., Freile, R., Freyman, T., Gaston, D., Harbour, L., Hua, T., Jiang, W., Martin, N., Miao, Y., Miller, J., Naupa, I., O'Grady, D., Reger, D., Shemon, E., Stauff, N., Tano, M., Terlizzi, S., Walker, S., and Permann, C. (2023) The Virtual Test Bed (VTB) Repository: A Library of Reference Reactor Models Using NEAMS Tools. *Nuclear Science and Engineering,* **197**(8), 2217–2233.

[11] Hanophy, J., Park, H., Labouré, V., Jung, Y., Schunert, S., Wang, Y., and Ortensi, J., Initial Demonstration of New Griffin Technologies for Simulating the Running-In Phase of Pebble-Bed Reactors. Technical Report INL/RPT-23-74913, Idaho National Laboratory (September, 2023).

[12] de Oliveira, R., Hanophy, J., Stewart, R., and Balestra, P., Verification of equilibrium core solution and decay heat modeling for the GPBR200. Technical Report INL/RPT-23-03822, Idaho National Laboratory (September, 2023).

[13] Ortensi, J., Mueller, C. M., Terlizzi, S., Giudicelli, G., , and Schunert, S., Fluoride-Cooled High-Temperature Pebble-Bed Reactor Reference Plant Model. Technical Report INL/RPT-23-72727, Idaho National Laboratory (May, 2023).

[14] Park, H., Jung, Y. S., Lee, C., Wang, Y., and Ortensi, J. (4, 2024) Initial assessment of online cross section generation capability of Griffin for gas-cooled pebble-bed reactor. In *Proceedings of the international conference on physics of reactors-PHYSOR 2024* San Francisco, CA: pp. 642–653.

[15] Gutowska, I. and Woods, B., OSU High Temperature Test Facility Design Technical Report. Technical Report OSU-HTTF-TECH-003-R2, Oregon State University Corvallis, OR (2019).

[16] Epiney, A. S., Strydom, G., Kile, R., Retamales, M. T., Yoon, S., Mueller, C., Gutowska, I., Zou, L., Hua, T., Fang, J., Yuan, H., Podila, K., Huang, X., Chen, Q., Jafri, T., Waddington, G., Pfeiffer, P., and Li, C. (2022) Overview of HTTF Modeling and Benchmark Efforts for Code Validation for Gas-Cooled Reactor Applications. In *Proceedings of 4th International Conference on Generation IV & Small Reactors (G4SR-4)* Toronto, Ontario, Canada: Canadian Nuclear Society pp. 3–6.

[17] Bayless, P. D., RELAP5-3D Input Model for the High Temperature Test Facility. Technical report, Idaho National Lab.(INL), Idaho Falls, ID (United States) (2018).

[18] American Nuclear Society (August, 1994) Decay Heat Power in Light Water Reactors, American Nuclear Society, ansi/ans-5.1-1994 edition.

[19] Ball, S. J., Corradini, M., Fisher, S. E., Gauntt, R., Geffraye, G., Gehin, J. C., Hassan, Y., Moses, D. L., Renier, J.-P., Schultz, R., and Wei, T., Next Generation Nuclear Plant Phenomena Identification and Ranking Tables (PIRTs) Volume 2: Accident and Thermal Fluids Analysis PIRTs. Technical Report NUREG/CR-6944, Oak Ridge National Laboratory (2008).

[20] Podila, K., Chen, Q., Huang, X., Li, C., Rao, Y., Waddington, G., and Jafri, T. (2022) Coupled simulations for prismatic gas-cooled reactor. *Nuclear Engineering and Design,* **395**, 111858.

[21] Fischer, P., Kerkemeier, S., Min, M., Lan, Y.-H., Phillips, M., Rathnayake, T., Merzari, E., Tomboulides, A., Karakus, A., Chalmers, N., and Warburton, T. (2022) NekRS, a GPU-accelerated spectral element Navier–Stokes solver. *Parallel Computing,* **114**, 102982.

[22] Fang, J., Shaver, D. R., Min, M., Fischer, P., Lan, Y.-H., Rahaman, R., Romano, P., Benhamadouche, S., Hassan, Y. A., Kraus, A., and Merzari, E. (2021) Feasibility of Full-Core Pin Resolved CFD Simulations of Small Modular Reactor with Momentum Sources. *Nuclear Engineering and Design,* **378**, 111143.

[23] Ho, L. W. A Legendre spectral element method for simulation of incompressible unsteady viscous free-surface flows PhD thesis Massachusetts Institute of Technology (1989).

[24] Shaver, D., Obabko, A., Tomboulides, A., Fang, J., Yu, Y., Tutwiler, S., Dai, D., Saini, N., and Boyd, C., Nek5000: improvements in the available RANS models, meshing, tutorials, and training. Technical Report ANL/NSE-21/79, Argonne National Laboratory Lemont, IL (2021).

[25] Tomboulides, A., Aithal, S., Fischer, P., Merzari, E., Obabko, A., and Shaver, D. (aug, 2018) A novel numerical treatment of the near-wall regions in the k-ω class of RANS models. *International Journal of Heat and Fluid Flow,* **72**, 186–199.

[26] Wilcox, D. (2008) Formulation of the k-ω Turbulence Model Revisited. *AAIA Journal,* **46**(11), 2823–2838.

[27] Shaver, D. R., Tomboulides, A., Obabko, A., Fang, J., and Saini, N. (2023) Demonstration of RANS models with wall functions in the spectral element code Nek5000. *Nuclear Engineering and Design,* **408**, 112302.

[28] Yuan, H., Yu, Y., and Shaver, D. (2022) Development of A Quadratic Tet-To-Hex Conversion for Pure Hexahedral Mesh: Application to Nuclear Engineering. In *Proceedings of 19th International Topical Meeting on Nuclear Reactor Thermal Hydraulics (NURETH-19)* Brussels, Belgium (Virtual): American Nuclear Society.

[29] van Antwerpen, W., Rousseau, R. G., and du Toit, C. G. (2012) Multi-sphere Unit Cell model to calculate the effective thermal conductivity in packed pebble beds of mono-sized spheres. *Nuclear Engineering and Design,* **247**, 183–201.

[30] Merzari, E., Yuan, H., Min, M., Shaver, D., Rahaman, R., Shriwise, P., Romano, P., Talamo, A., Lan, Y., Gaston, D., et al. (2021) Cardinal: A lower-length-scale multiphysics simulator for pebble-bed reactors. *Nuclear Technology,* **207**(7), 1118–1141.

[31] Novak, A., Carlsen, R., Schunert, S., Balestra, P., Slaybaugh, R., and Martineau, R. (2021) Pronghorn: A Multidimensional Coarse Mesh Application for Advanced Reactor Thermal-Hydraulics. *Nucl. Tech.,* **207**, 1015–1046.

[32] Schunert, S., Balestra, P., Carlsen, R., DeHart, M., Martineau, R., and Novak, A., Coupling of Pronghorn and RELAP-7 for a Pebble Bed Reactor. Technical Report INL/CON-19-54415-Rev000, Idaho National Laboratory (August, 2020).

[33] Stewart, R., Reger, D., and Balestra, P., Demonstrate Capability of NEAMS Tools to Generate Reactor Kinetics Parameters for Pebble-Bed HTGRs Transient Modeling. Technical Report INL/EXT-21-64176, Idaho National Laboratory (August, 2021).

[34] Ooi, Z., Zou, L., Hua, T., Fang, J., and Hu, R., Modeling of a Generic Pebble Bed High-temperature Gas-cooled Reactor (PB-HTGR) with SAM. Technical Report ANL/NSE-22/59, Argonne National Laboratory (2022).

[35] Ooi, Z., Zou, L., Hua, T., Fang, J., and Hu, R., Multi-Physics System-level Simulations of a Generic Pebble Bed High-Temperature Gas Cooled Reactor with Coupled SAM/Griffin Model. Technical Report ANL/NSE-23/45, Argonne National Laboratory (2023).

[36] Zou, L. and Hu, R., Recent SAM Code Improvement to Heat Transfer Modeling Capabilities. Technical Report ANL/NSE-19/46, Argonne National Laboratory (2019).

[37] van Antwerpen, W., Du Toit, C. G., and Rousseau, P. G. (2010) A review of correlations to model the packing structure and effective thermal conductivity in packed beds of mono-sized spherical particles. *Nuclear Engineering and Design,* **240**(7), 1803–1818.

[38] Roberto, T. D., Lapa, C. M., and Alvim, A. C. (2020) Scaling analysis of reactor cavity cooling system in HTR. *Nuclear Technology,* **206**(4), 527–543.

[39] Gaston, D. R., Permann, C. J., Peterson, J. W., Slaughter, A. E., Andrš, D., Wang, Y., Short, M. P., Perez, D. M., Tonks, M. R., Ortensi, J., Zou, L., and Martineau, R. C. (2015) Physics-based multiscale coupling for full core nuclear reactor simulation. *Annals of Nuclear Energy,* **84**, 45–54.

[40] Huxford, A., Leite, V. C., Merzari, E., Zou, L., Petrov, V., and Manera, A. (2023) A hybrid domain overlapping method for coupling System Thermal Hydraulics and CFD codes. *Annals of Nuclear Energy,* **189**, 109842.

[41] NEA, PBMR Coupled Neutronics/ Thermal-hydraulics Transient Benchmark: The PBMR-400 Core Design - Volume 1: The Benchmark Definition. Technical Report NEA/NSC/DOC(2013)10, Organisation for Economic Co-operation and Development-Nuclear Energy Agency (2013).

[42] Zheng, Y., Stempniewicz, M. M., Chen, Z., and Shi, L. (2018) Study on the DLOFC and PLOFC accidents of the 200 MWe pebble-bed modular high temperature gas-cooled reactor with TINTE and SPECTRA codes. *Annals of Nuclear Energy,* **120**, 763–777.